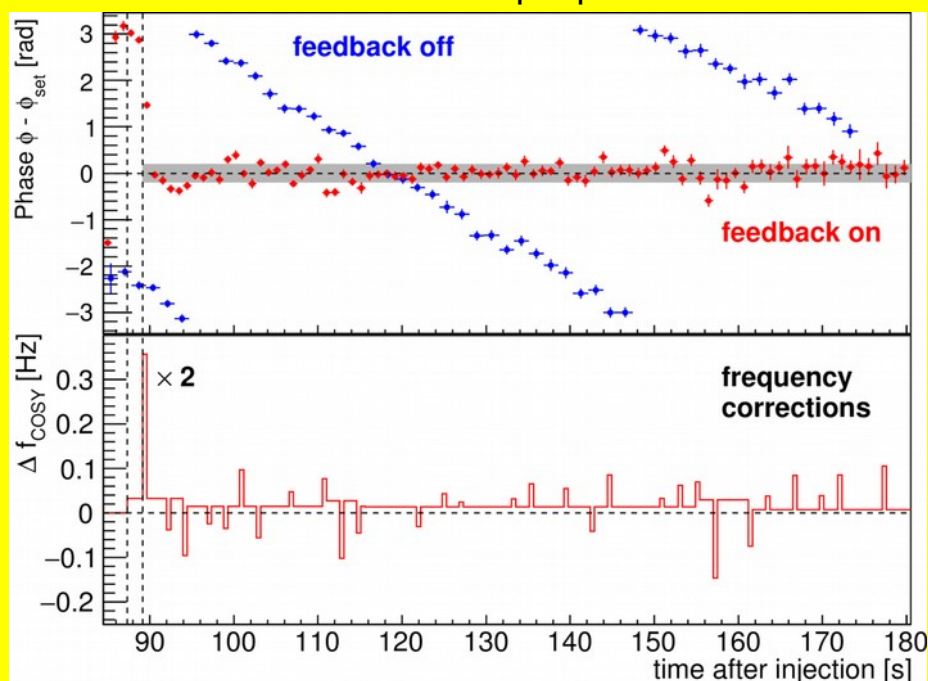
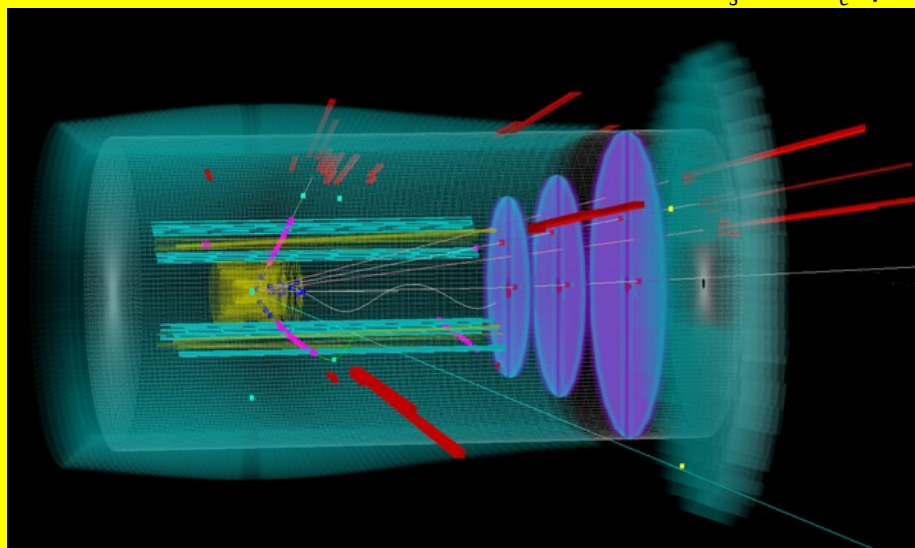


Institut für Kernphysik (IKP)
COSY

JEDI: active control of the spin precession in COSY



PANDA: event display for the decay $D_s^+ \rightarrow e^+ \nu_e \eta$



Annual Report 2016

Annual Report 2016

Institut für Kernphysik / COSY

DIRECTORS AT THE IKP:

Experimental Hadron Structure (IKP-1):
Experimental Hadron Dynamics (IKP-2):
Theory of the Strong Interactions (IKP-3/IAS-4):
Large-Scale Nuclear Physics Equipment (IKP-4):

Prof. James Ritman (managing director)
Prof. Hans Ströher
Prof. Ulf-G. Meißner
Prof. Mei Bai

EDITORIAL BOARD:

Prof. Frank Goldenbaum
Dr. Dieter Grzonka
Prof. Christoph Hanhart
Dr. Volker Hejny
Dr. Andro Kacharava
Prof. Andreas Lehrach
Prof. Livia Ludhova
Prof. Ulf-G. Meißner
Prof. James Ritman
Dr. Thomas Sefzick
Prof. Hans Ströher
Dr. Raimund Tölle

Cover picture:

The upper panel of the cover picture shows the first implementation of an active feedback system to control the spin precession in a storage ring. Precision experiments based on a resonant operation of a spin manipulating device in the ring — like the measurement of the deuteron EDM by means of an rf Wien filter — have to maintain both the resonance condition and the relative phase between the spin precession and the rf signal to a level that cannot be achieved without an active control. This feedback system continuously monitors the phase of the spin precession and locks it to the phase of the rf signal. For this, it changes the spin precession frequency by slightly modifying the synchrotron frequency in a range well below 1 Hz. The upper plot shows the relative phase for a cycle without a running feedback system and for a cycle with the feedback system switch on. The lower plot shows the corrections to the synchrotron frequency. As a result the relative phase could be maintained at a level of ± 0.2 rad, which is one of the milestones achieved at COSY towards the precursor experiment. Further details are discussed in Section 2.2.1.

The lower panel displays a simulated anti-proton proton reaction which generates a D_s pair inside the future $\overline{\text{PANDA}}$ experiment. One of the D_s decays semileptonically into $e^+ \nu_e \eta$. This is a very rare decay which requires that all generated charged and neutral particles except the neutrino are reconstructed, thus making it an ideal benchmark channel for $\overline{\text{PANDA}}$. One can see the tracks of the generated particles, the measured points in the tracking detectors as well as the energy in the calorimeters. More details on this analysis and the tracking detectors in $\overline{\text{PANDA}}$ can be found in Chapter 4.

Contents

Preface	v
1 Accelerator Developments at COSY	1
1.1 COSY orbit upgrade	1
1.2 Beam cooling	2
1.3 Expanding COSY for applied research	3
1.4 Siberian snake	4
1.5 Operation statistics of COSY	7
2 Storage Ring Based EDM Search	9
2.1 Experimental methods to measure EDMs of charged particles	9
2.2 Experimental achievements at COSY	9
2.3 Technical developments	14
2.4 Beam and spin dynamics	17
2.5 Summary and goals	19
3 The HESR at FAIR	21
3.1 Project status and interface to FAIR	21
3.2 Magnets, power converters and radio frequency system	21
3.3 Injection, beam diagnostics and vacuum	22
3.4 Stochastic cooling and experiment installations	24
4 The PANDA Experiment at FAIR	27
4.1 Feasibility study to measure the $D_s^+ \rightarrow e^+ \nu_e \eta$ decay form factor	27
4.2 Silicon strip readout chip ASIC	28
4.3 Online tracking on GPUs	28
4.4 The straw tube tracker	29
4.5 The phase-0 straw trackers together with HADES	30
4.6 KOALA at HESR	31
5 Neutrino Physics	33
5.1 Borexino latest results and perspectives	33
5.2 Short distance neutrino oscillations with Borexino	34
5.3 Towards neutrino mass hierarchy: JUNO	35
6 COSY - Highlights from Hadron Physics	37
6.1 Precision studies on angular asymmetries of the $d + p \rightarrow {}^3\text{He} + \eta$ reaction	37
6.2 Model-independent measurement of the spin triplet $p\Lambda$ scattering length	38
6.3 Search for an isospin $I = 3$ dibaryon	39
6.4 Coherent meson production in the reaction $pd \rightarrow pdX$	39
6.5 Isoscalar single-pion production in the region of Roper and $d^*(2380)$ resonances	40
6.6 Measurement of the $\omega \rightarrow \pi^+ \pi^- \pi^0$ Dalitz plot distribution	41
6.7 Charge symmetry breaking in $dd \rightarrow {}^4\text{He} \pi^0$	42
7 Further Experimental Activities	44
7.1 Photo production of the π^0 meson up to 5.5 GeV with CLAS	44
7.2 Transition form factor of the η' meson with CLAS12	46
7.3 A spin-off from COSY: Production and interaction of polarized molecules	47
7.4 PAX/TRIC detector development	49

8	Theoretical Investigations	51
8.1	Introduction	51
8.2	Nuclear physics near a quantum phase transition	51
8.3	Nuclear structure using relative coordinates	51
8.4	$\Lambda\Lambda$ and ΞN interactions in chiral effective field theory	52
8.5	The nucleon EDM from the <i>flowed</i> Weinberg operator	53
8.6	The decay $\omega \rightarrow \pi\pi$ revisited	53
8.7	The width of the Δ and Roper resonances at two-loop order	54
8.8	What is the X(5568)?	55
8.9	Lineshapes of the $Z_b(10610)$ and the $Z_b(10650)$	56
A	Councils	58
A.1	CBAC – COSY Beam Time Advisory Committee	58
B	Publications–Journal Articles	59
C	Talks and Colloquia	64
C.1	Conference and workshop contributions	64
C.2	Colloquia	75
D	Diploma and Ph.D. Theses	78
E	Awards & Offers for Professorships	81
F	Third Party Funded Projects	82
G	JCHP-FFE Projects	83
H	Conferences (co-)organized by the IKP	84
H.1	Physics with neutral kaon beam at JLab workshop	84
H.2	European JUNO analysis kick-off meeting at IKP	84
H.3	International workshop expanding COSY capability for multi-disciplinary science	84
H.4	14th International workshop on meson production, properties and interaction—MESON 2016	85
H.5	Hadron Physics Summer School 2016	85
H.6	Georgian–German Science Bridge: SMARTI EDM_Lab opening and 7 th GGSWBS in Tbilisi	86
H.7	Symposium on “Advances in Effective Field Theories” and the Lise Meitner Prize	87
H.8	Excited hyperons in QCD thermodynamics at freeze-out	87
I	Teaching Positions	89
J	Personnel	90
K	Further Contributions	93

Preface

The achievements of the Institut für Kernphysik (IKP) in 2016, the second year of the ongoing period of the "Programme oriented Funding" (PoF), have again been remarkable and clearly demonstrated the scientific virtue of our research. IKP is an indispensable key player in various projects and a reliable partner in scientific collaborations.

The EDM project accomplished a number of important steps towards a high precision storage ring based EDM measurement. For this activity Prof. Ströher has been awarded an Advanced Grant by the European Research Council (ERC) given to outstanding research activities which confirms the high scientific value. Marcel Rosenthal was awarded the JARA Excellent Junior Award for his project "Spin Tracking Studies towards Electric Dipole Moment Measurements in Storage Rings" (JARA-FAME).

The activities for the FAIR projects are in excellent condition on the accelerator side as well as on the detector side. The HESR components preparations are on schedule and the development of PANDA detector components is making very sustainable progress. Many fully tested and assembled dipole and quadrupole magnets have already been delivered to Darmstadt. These activities are crucial to the realization of both HESR and PANDA.

The neutrino physics activities are ramping up by joining the Borexino/SOX and JUNO experiments. During this year three new PhD students started to work for Borexino/SOX and two for JUNO.

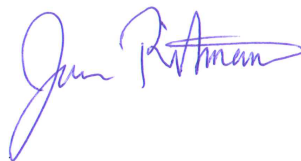
The excellent scientific achievements of the COSY hadron physics program have been summarized this year in a review article. Some data are still being analyzed, and further important results will be completed shortly. COSY is now being mostly used as a test facility for FAIR and to perform preliminary studies for a storage ring EDM experiment (srEDM). Since the amount of beam time is oversubscribed, recommendations to select the best measurements are made by the COSY Beamtime Advisory Committee (CBAC).

The theory group is working on various topics in nuclear and hadronic physics via effective field theory applications and high performance computing. Prof. Meißner was awarded with the Lise Meitner Prize 2016 by the European Physical Society (EPS) to recognize the outstanding work in these fields.

During the past year one major issue was the discussion of the IKP future within the strategy of the Forschungszentrum Jülich. Despite widespread support for the IKP activities, the Board of Management plans to end the particle/hadron/nuclear activities of our institute in the medium term. Our main emphasis is and will be to avoid any drawbacks for the science we are pursuing.

Last but not least I would like to thank all IKP members, the colleagues of the infrastructure departments as well as many members of the national and international nuclear and hadronic physics community, explicitly including the local universities, for their strong support of our activities.

Jülich, March 2017



James Ritman, managing director

1 Accelerator Developments at COSY

Even though the hadron physics program at COSY has been completed by the end of PoF-2 (2015), the facility still remains the workhorse of the experimental scientific program at IKP: besides its exploitation for accelerator and detector development tests for FAIR (HESR, CBM and PANDA), COSY is now used for R&D in connection with the pursued search for charged-particle EDMs in storage rings. COSY is the only operational EDM test facility worldwide, and in order to prepare for a first direct measurement for deuterons, it is currently upgraded. In addition IKP is looking into a possible use of COSY beams for applications.

1.1 COSY orbit upgrade

In order to fulfill the requirements of the JEDI experiment some components of the COSY synchrotron need to be upgraded or to be added. One of these systems is an automated orbit correction system which is needed to limit the maximum orbit deviation. Basically, each individual orbit corrector is powered and the corresponding change of the orbit is measured. From these data numbers are deduced describing the orbit response in the synchrotron to the excitation of each orbit corrector (Orbit Response Matrix, ORM). The next natural step is to inspect the beam position monitor (BPM) in more detail.

The accuracy of the BPM system needs improvements to reach a root mean square (RMS) orbit deviation value to fulfill the requirements of the JEDI experiment. The analog processing of the orbit information contains offsets which differ with the gain selected for the difference signal. The measurement of this behavior is shown in Fig. 1. The gain for the difference signal has to be adjusted to higher values when the particles are on axis.

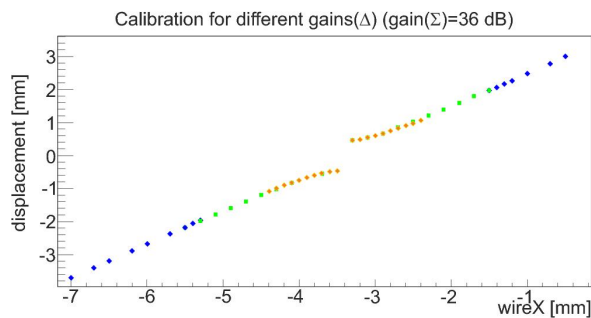


Fig. 1: Test bench measurements around the 0 position of the BPM. Blue points denote 66 dB amplification, green points 72 dB, and orange points 78 dB. There is a clear jump close to 0 mm displacement combined with a clearly visible nonlinearity. The reason is an offset in the analog signal processing, accompanied by an independent determination of the sign of the beam position.

Several possibilities to enhance the BPM system accuracy were explored and presented to a team of beam instrumentation experts from CERN, DESY, and GSI. Recommendation was to upgrade the read out electronics using the commercially available system LIBERA Hadron. The LIBERA system is based on 250 MHz 16 bit ADCs with a postprocessing of the signals mainly done digitally utilizing an FPGA. It natively supports 2 widely spread control system frameworks: EPICS and TANGO. As the EPICS system is more widely spread, and also TANGO is up to now only used in light sources, another decision was made to use the EPICS framework for further COSY developments and upgrades. To speed up the development process, another company named Cosylab, specialized on control system integration for accelerators, was contracted.

As a first EPICS based application the archiver feature was activated for the BCT signal to demonstrate the correct implementation and integration of the EPICS system components. The signal can be displayed, several signals can be overlayed and the saved data can be downloaded. The upgrade of the orbit control system was divided into several stages. Stage 0 includes the following items:

- GUI using Control System Studio (CSS)
- Implementing correction algorithm developed at COSY
- Using COSY BPM system, adapting EPICS to COSY data communication
- Controlling correction dipoles, adapting EPICS to COSY data communication
- Setup of other CSS parts like archiver and machine settings saving
- Training

The next stage will include the integration of the LIBERA hardware into the system. In addition a transition to a new timing system is under discussion.

During 2016 most effort was spent to implement the system communication, based on a self developed standard called Single Command Single Response (SCSR), into the new CSS based GUI. This has been successfully tested for both target systems, the BPM readout and the correction magnet control. A preliminary GUI has been developed and the successful operation of the orbit correction is shown in Fig. 2. The measured COSY orbit was saved as reference. Then a bump was introduced and the activated orbit correction could re-install the reference orbit. Further features like BPM settings control still have to be implemented.

Any orbit correction is limited by the misalignment of the magnets. This effect is examined and explained in detail in "Theoretical Limits of Closed Orbit Corrections" by F. Hinder in Appendix K. The misalignment itself has been measured and the re-alignment procedure has been started.

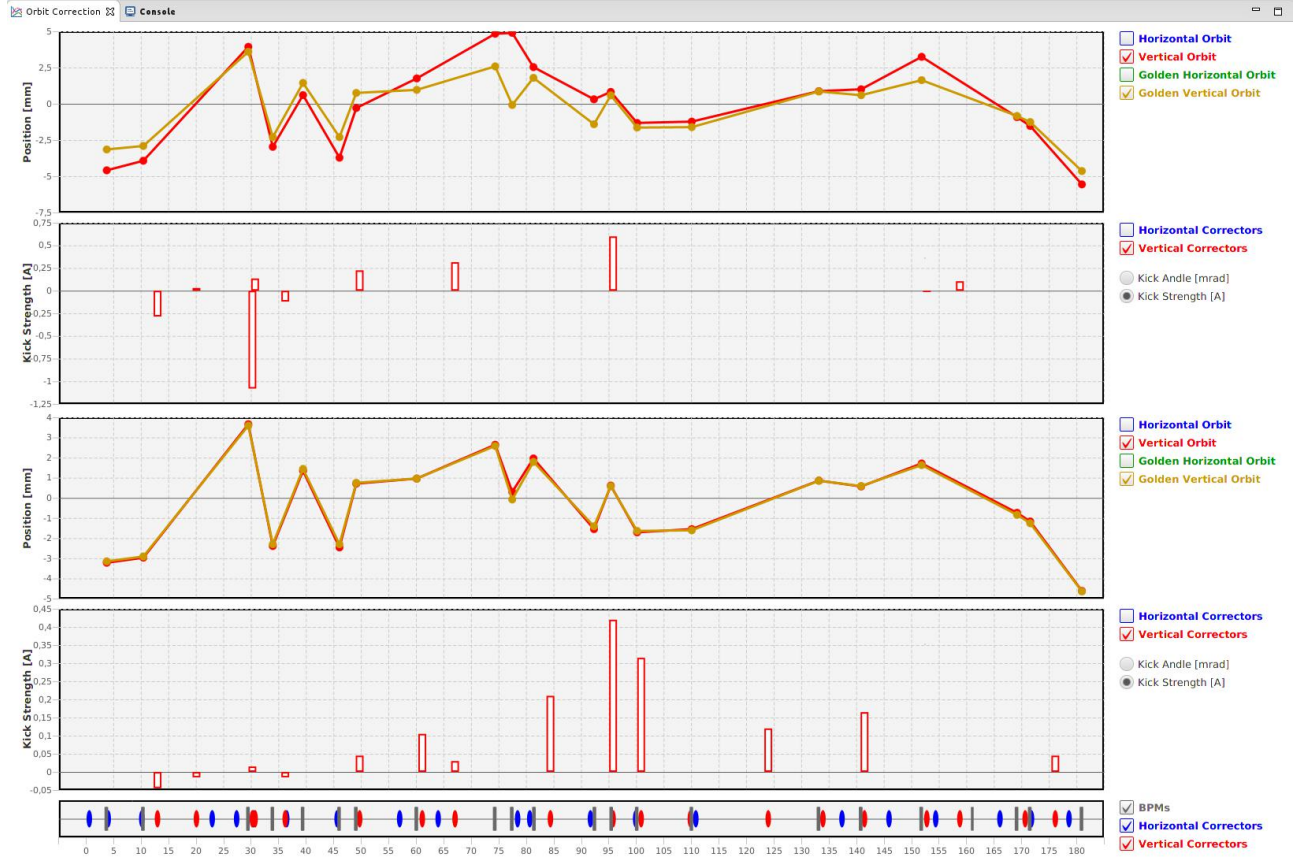


Fig. 2: Test of the orbit correction. The COSY orbit was saved as reference orbit and then a bump inserted. Afterwards the orbit correction algorithm was used to correct the orbit back to the initial one. This is a preliminary setup to test the functionality of the communication to the COSY BPM system and correction magnet controllers, which succeeded. The upper graph shows the distorted orbit in red and the desired (undistorted) orbit in gold. The column height in the histogram below corresponds to the corrector strength. The next graph below shows that the desired orbit and the orbit achieved after correction coincide. The corresponding corrector strengths as displayed in the histogram below differ clearly from the previous setting. The small graph at the bottom displays the position of the horizontal (blue) and vertical (red) orbit correctors along the beam line.

Table 1: Overview of the beam parameters applied for cooling at COSY using the 2 MeV e-cooler.

Proton energy [MeV]	Proton momentum [MeV/c]	Electron energy [MeV]	Max. electron current [A]
200	644	0.109	0.5
353	887	0.192	0.5
580	1194	0.316	0.3
1670	2434	0.908	0.9
2300	3100	1.25	0.5

1.2 Beam cooling

Two weeks of beam time were dedicated to high-energy electron cooling in 2016 at COSY. Electron cooling studies were carried out with proton momenta up to 3.1 GeV/c corresponding to electron beam energies up to 1.257 MeV. Table 1 summarizes the proton and electron beam parameters using the 2 MeV electron cooler so far.

Stable cooler operation was possible with an electron current up to 0.8 A at 1.25 MeV (not yet used for cooling).

Fig. 3 shows the longitudinal Schottky spectra of the 3.1 GeV/c proton beam during cooling with the 0.5 A, 1.257 MeV electron beam. The spectra were acquired using the stochastic cooling pickup built for the HESR and installed into the COSY ring for testing, see section 3.4.

The effects of the cluster jet target on the beam and their mitigation using electron cooling were studied. These studies are of interest for the future PANDA experiment that is going to use the cluster jet target currently under development at Münster University. The preliminary results indicate, that electron cooling even with a moderate electron current of 0.5 A could significantly mitigate the energy loss and decrease the momentum spread of the 3.1 GeV/c proton beam (see Fig. 4).

The positive effects of the e-cooling such as reduction of the momentum spread and reduction of emittance growth during target operation could be further improved when

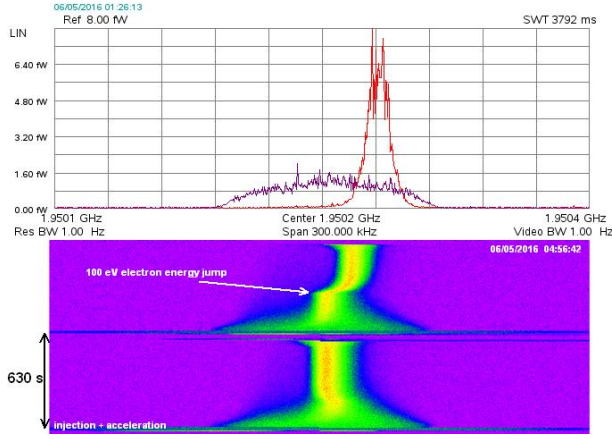


Fig. 3: Longitudinal Schottky spectra of the 3.1 GeV/c proton beam as measured by the pickup of the stochastic cooling system during cooling with the 0.5 A, 1.257 MeV electron beam. The color spectrogram shows the evolution of the Schottky spectra during the cooling process and tuning of the electron beam. The upper plot demonstrates the initial beam spectrum before e-cooling (purple trace) and a spectrum of a well-cooled beam (red trace).

the cooling process was assisted by the barrier bucket RF system.

The development of the cooler model continued. During COSY maintenance periods, measurements have been performed to benchmark and further optimize the model. Besides the software used for the automated compensation of the Larmor rotation and the galloping effects, additional tools are becoming available. The e-beam orbit designer tool utilizing the orbit response matrix method allows for shorter cooler setup times and better e-beam quality in the cooling section and thus stronger beam cooling. It also improves the reliability of the overall system by performing plausibility checks of the operator inputs. The orbit feedback feature keeps the orbit constant at a desired location while the upstream magnetic elements are being adjusted. This way an optimum electron collector efficiency can be guaranteed paving the way to higher e-current at high energies. Further improvements of the model such as implementation of the hysteresis and iron saturation effects are on the way. More details can be found in Appendix K "Progress with the model development for the 2 MeV electron cooler" by A. Halama.

1.3 Expanding COSY for applied research

With the successful integration of the ion source at the compact antiproton storage ring ELENA at CERN IKP contributed a substantial subsystem. After a short set-up period, negative ions from this ion source were stored for many revolutions for the first time. Important milestones could be reached.

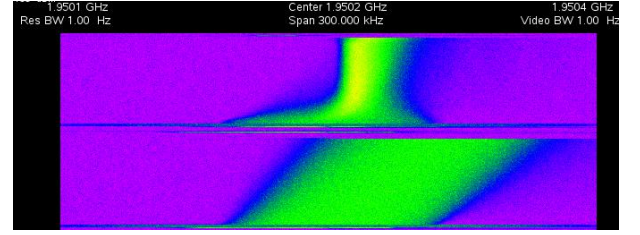


Fig. 4: Evolution of the Schottky spectrum of the 3.1 GeV/c proton beam while interacting with a cluster jet target of density $n_a = 2 \cdot 10^{14} \text{ cm}^{-2}$. The lower part of the color spectrogram shows the increase of the revolution frequency due to the target only. This corresponds to a decrease in energy of the circulating particles. The upper part shows that electron cooling can compensate the change in energy caused by the beam - target interaction. The frequency span of 300 kHz corresponds to a momentum spread $dp/p = 2.5 \cdot 10^{-3}$.

COSY can contribute significantly to applied research with accelerators in the fields of light ion production for nuclear medicine, light ion beams for studying radiation effects during space explorations, and light ion beams for radiological research. Currently, most high energy proton accelerators provide only beams at one fixed energy, e.g. 1400 MeV at the CERN-PSB, 590 MeV at the PSI cyclotron, etc. COSY is the only proton accelerator in Europe that covers the entire energy range of interest (from 300 to 2500 MeV) and that is flexible enough for providing external proton beams at a series of different but well determined energies with an accuracy better than 0.1%. As the intensity at COSY is in the low nA range, basic properties of reactions employed in isotope production can be measured and corresponding procedures can be established.

A request submitted to the CBAC03 meeting asking for irradiations with protons of energies between 50 and 200 MeV at the extracted beam of the COSY facility was accepted. To prove the feasibility of this kind of experiments an irradiation with protons at 100 MeV with at least 1 nA integrated intensity had been scheduled for autumn 2016. Several new challenges to the accelerator setup had to be met for this achievement.

The acceleration to 100 MeV, starting from 45 MeV injection energy is one of the challenges. Extracting 100 MeV protons requires a modification of the standard COSY ramp definitions, as the whole system is adjusted for maximum ramp speed for highest energies. The standard ramps consist of smooth increase/decrease of dI/dt from/to 0 to/from maximum at start/end of the ramp. These transitions require 200 ms time. Between these two transitions a linear ramp with maximum dI/dt is inserted, until the desired energy is reached. When ramping from the fixed 45 MeV injection energy to only 100 MeV final energy, the linear part had been minimized (to 2 ms), and the transition time had been reduced signifi-

cantly to 130 ms. To avoid beam losses because of betatron resonances careful tuning of the quadrupole settings was needed. Methods to reduce this transition time were developed. The setup found may be used as a starting point to reduce the required setup time.

The extraction method readily available at COSY is the ultra slow extraction (USE), a procedure where the stored beam is slowly extracted via white noise excitation and the $11/3$ horizontal betatron tune resonance. The systems are designed for typical extraction times in the order of minutes. To use this method for extraction the horizontal betatron tune needs to be adjusted to a value close to the extraction resonance. This tune adjustment is mandatory for the extraction and requires an adjustment of the optics by change of quadrupole settings after acceleration. For higher energy operation this is a standard procedure without any impact on the beam intensity. At an energy of 100 MeV a significant beam loss was observed and still needs to be cured.

The integrated intensity on target was optimized by reducing the cycle time between injections. Thus the duty cycle could be increased. Several measures were combined to accomplish this task. The power available for the white noise excitation, designed for ultra slow extraction over minutes, was increased to have extraction over as little as 1 sec. The software for the accelerator timing was modified to allow injections more frequent than 0.5 Hz. The setup of all involved systems was adjusted with beam for best efficiency, starting from injection, bunching, acceleration, extraction, and transmission through the extraction beam line.

The requirement for beam adjustment on target with 10 mm diameter at entrance and exit of the foil stack which had to be irradiated is quite different from previous nuclear physics experiments carried out at the external COSY beam, where the request was mostly to have the smallest beam spot at target with very little beam halo outside. To improve the setup of the beamline a detailed study of profiles measured along the whole line and verification of the beamline model was carried out. New procedures to adjust the beam line magnets were developed. Some beam spot shapes during beam size adjustment are not yet understood and require further study of beam properties of the extracted beam.

The irradiation of a stack of target foils for the INM group (INM-5, FZ Jülich) was carried out with protons at 100 MeV kinetic energy with an average beam current of 1.2 nA in a 1.4 seconds cycle. Fig. 5 shows the beam spot adjusted to the 10 mm foil size, measured by irradiation of a radiographic film, at the entrance and the exit of the irradiation foil stack.

Irradiations at energies below 100 MeV were required by several users. This was accomplished by degrading the 100 MeV extracted beam right in front of the experiment setup. Issues which need further optimization include scattering in the degrader in close vicinity of the target, additional scrapers to stop the background produced in the degrader while keeping the intensity on target.

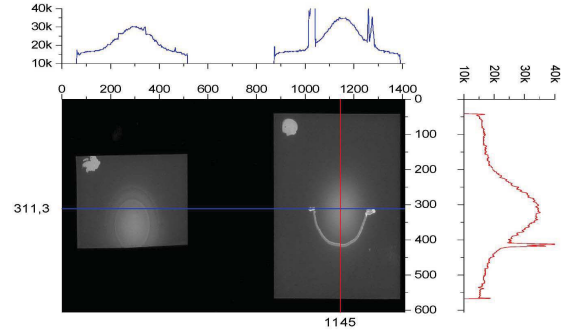


Fig. 5: Beam spot at the target as recorded by a radiographic film after 20 extractions. Left spot is recorded at the exit of the target chamber, the spot on the right side is from the entrance of the target chamber. The thin semi-circle line on the right is indicating the target holder. Beam size at the entrance is 10 mm (h) x 12 mm (v).

Future improvements of the systems may lead to some increase in beam current on target beyond 1 nA. A further reduction of the cycle time is not possible, as the time needed for acceleration and beam preparation for extraction are now the limiting factors. Some of the observed beam losses can be cured once a more detailed understanding of the processes involved during the different phases of beam manipulations is reached. Without a major upgrade of COSY, the upper limit for the extracted average beam current is given by the number of injected particles (app. 10^{11} protons). Assuming a repetition time of 1.4 s this corresponds to 11 nA if all losses are neglected.

The capability of COSY to deliver a 1 nA proton beam at 100 MeV at the external experiment station BIG KARL was proven. In the future the required setup time can possibly be reduced by establishing standardized setup procedures for these kinds of experiments.

1.4 Siberian snake

A 4.7 Tm superconducting (SC) solenoid has been delivered by CRYOGENIC LTD (London, UK) to Forschungszentrum Jülich, successfully commissioned in the COSY hall and will be implemented in the COSY accelerator. The solenoid will be operated as full Siberian snake to provide a longitudinal polarized proton beam at the PAX interaction point.

1.4.1 Strategy for the PAX experiment

Siberian snakes are used to avoid crossing depolarizing resonances in circular accelerators. The spin rotation in a full Siberian snake is 180° per turn around a horizontal axis, forcing the spin tune to be a half integer, independent of the beam energy. If only one Siberian snake is used, the invariant spin axis is in the horizon-

tal plane. This is an interesting feature to deliver longitudinally polarized beam to internal experiments. The COoler SYnchrotron COSY accelerates polarized protons and deuterons up to a momentum of 3.7 GeV/c. For this experiment the proton beam will be injected vertically polarized into COSY, electron-cooled and accelerated to beam momenta between 520 and 920 MeV/c. The momentum range for commissioning is chosen in a way, that the 4.7 Tm SC solenoid can be operated as full Siberian snake. By ramping the SC solenoid from zero to 1.95 resp. 3.4 Tm, the vertical beam polarization will be transferred into the horizontal plane. The beam will in particular be longitudinally polarized in the straight section where EDDA and PAX are located, if the SC solenoid is installed at the location of the ANKE detector. The existing EDDA polarimeter will be used to measure the change of vertical beam polarization during the SC solenoid ramp. We will first start with a beam momentum of 911.86 MeV/c (kinetic energy of 370 MeV), where the spin tune $\nu_{sp} = \gamma G$ without snake equals 2.5. Since turning on a Siberian snake moves the spin tune towards the nearby half-integer spin tune, the spin tune stays at 2.5 and depolarizing resonances are not crossed during the snake ramp. Under these conditions no polarization losses are expected. In a stepwise approach we will move γG close to integer and study spin resonance crossing during the snake ramp. Finally, we plan to investigate the beam momentum of 521 MeV/c (135 MeV), where γG equals roughly 2.05. This beam momentum is proposed for the TRIC and PAX experiment.

1.4.2 Spin and beam dynamics relevant for the experiment

Only one imperfection resonance $\gamma G = 2$ has to be crossed at a momentum of 463.8 MeV/c (108.4 MeV) in the momentum range from injection up to 920 MeV/c. The existing orbit correction system of COSY is routinely been used to overcome this resonance by exciting an adiabatic spin flip. The only intrinsic resonance in this momentum range is $\gamma G = 6 - Q_y$ located at 826.9 MeV/c (312.4 MeV) for a vertical betatron tune of $Q_y = 3.61$. The tune-jump system will be used to preserve polarization at this resonance by increasing the crossing speed significantly. The betatron tunes have to be chosen carefully at the final momentum to avoid polarization losses by higher-order depolarizing resonances. The relevant higher-order depolarizing resonances at 135 and 370 MeV are plotted in Fig. 6.

For a full Siberian snake this leads to an transverse phase space rotation of 32.2° . Calculations have been performed to investigate the influence of the solenoidal field on beam optics. As can be seen in Fig. 7, the betatron amplitude grows from below 30 m without snake to more than 40 m with the snake turned on. This is not of major concern as long as the transverse acceptance limit of COSY is not reached, which is unlikely to happen due to adiabatic shrinking of the beam size during acceleration. Eventually the betatron amplitude growth could be sup-

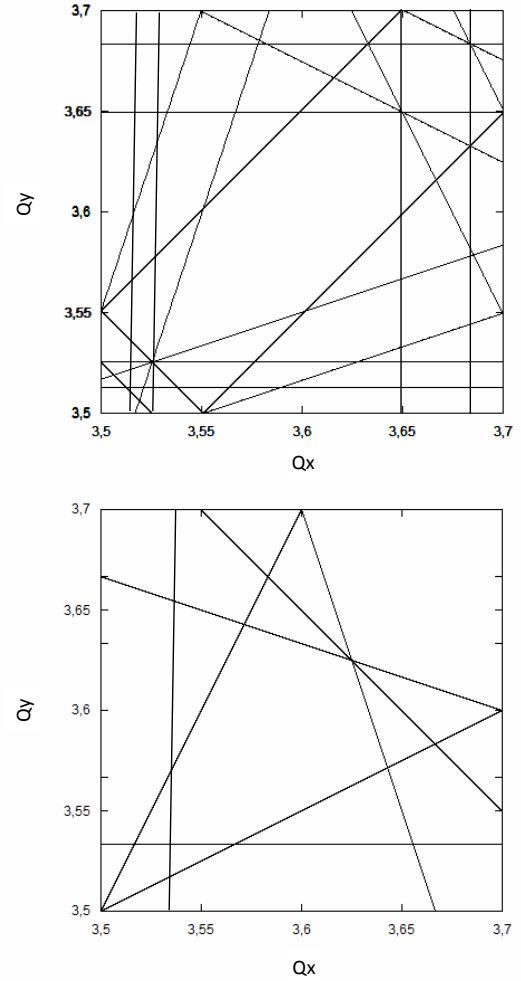


Fig. 6: Higher-order depolarizing resonances at 135 MeV (upper panel) and 370 MeV (lower panel) up to fourth order plotted in a betatron tune diagram.

pressed by nearby quadrupole triplets. The betatron tunes are shifted from $Q_{x,y} = 3.62; 3.59$ without snake to 3.76 resp. 3.57 with the snake turned on. The strength of the quadrupole families in the arcs can be adjusted accordingly if this betatron tune setting leads to a reduced beam life time or is causing polarization losses because the distance to a higher-order depolarizing resonance is too small.

1.4.3 SC Solenoid parameters and performance

Superconducting magnet technology has to be used to achieve an acceptable length of the snake. The main technical data of the SC solenoid are: length of the cryostat: 975 mm, bore diameter (i.e. inner diameter of vacuum tube): 90 mm, maximum field integral along axis: 4.7 Tm, maximum field: 6 T at 258.83 A. Cryogen-free operation (no external liquefier, no manual refill of cryogenic liquids), turnkey, stand-alone system required in-

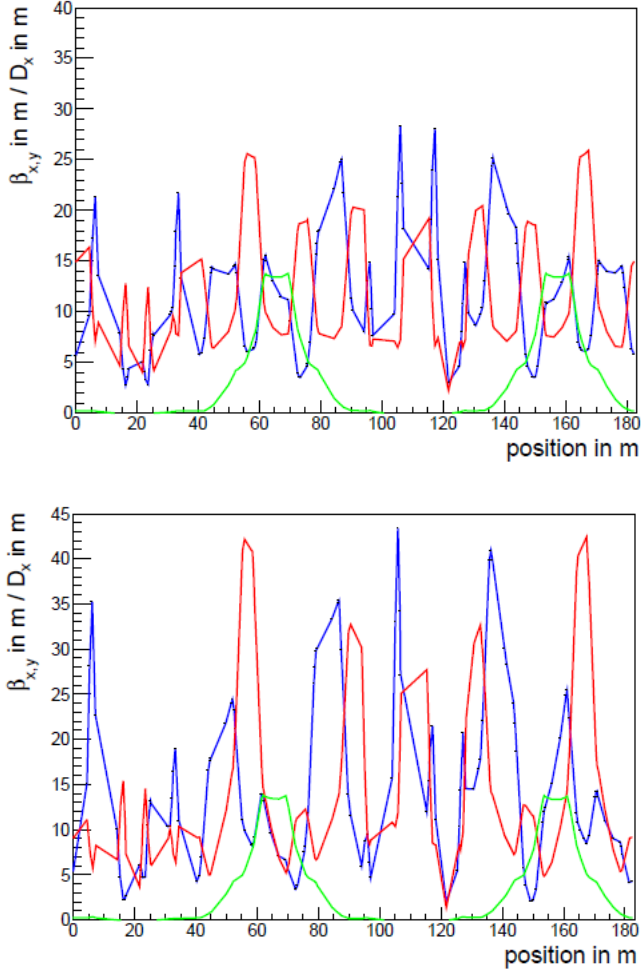


Fig. 7: Beam Optics without (upper panel) and with (lower panel) Siberian snake turned on. The transverse betatron amplitudes $\beta_{x,y}$ (blue, red line) and horizontal dispersion D_x (green line) are plotted versus the position in the COSY ring.

cluding all the auxiliary systems (compressors, power units, re-condensing system, Hall sensors, temperature sensors) are additional features of the system.

To realize a full Siberian snake a magnetic field of roughly 2.7 T at a beam momentum of 521 MeV/c and 4.8 T at 911.86 MeV/c has to be provided by the SC solenoid. The setup of the snake on a test bench in the COSY hall can be seen in Fig. 8 (upper panel). The sequence shown in Fig. 8 (lower panel) has been performed with a ramp of 0.7 A/s to a maximum field of 5 T and 300 s hold time in between. Temperatures in several subsystems are also shown in Fig. 8 (lower panel). They stay below 5.5 K during the ramp procedure. The established ramp rates to different maximum fields are compiled in the Tab. 2.

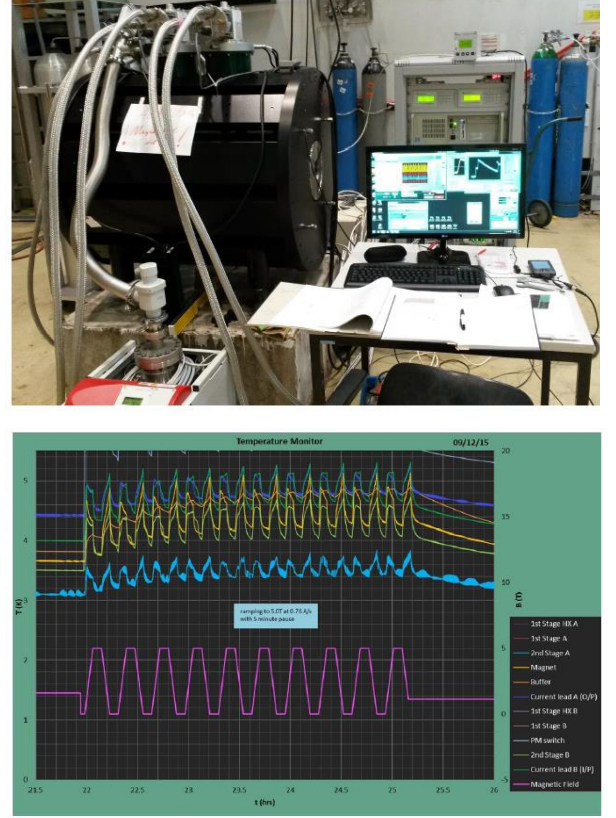


Fig. 8: Setup of the snake on a test bench in the COSY hall (upper panel). A sequence of ramps to 5 T at a ramp rate of 0.76 T/s measured with a hall probe (lower graph of lower panel). Temperatures in different subsystems of the snake are shown in the upper curves of the lower picture.

1.4.4 Summary and goals

The superconducting solenoid has been commissioned in the COSY hall (LKW Schleuse). Several sequences of the required ramps for the magnetic field have been performed and established up to a maximum field of 5 Tesla. After roughly four hours the equilibrium temperature of the superconducting solenoid is reached, ensuring stable conditions over long time periods. The system is ready for installation in the COSY ring.

Table 2: Parameters for ramps that have been experimentally verified by CRYOGENIC LTD.

Max. field [T]	Ramp rate [A/s]	Sequence	Dwell time [s]
3	1.65	yes	300
4	1.0	yes	300
5	0.76	yes	300
6	0.24	no	—

1.5 Operation statistics of COSY

For 2016 in total 3920 hours of operation were scheduled for FAIR, JEDI and irradiation studies.

As shown in Fig. 9, 2072 hours (23%) were scheduled for dedicated beam dynamic studies, equipment tests for HESR and FAIR related activities, 1176 hours (13%) for precursor experiments on EDM studies and 672 hours (8%) for irradiation related activities. 1120 hours (13%) were used for COSY machine development and experimental set-up and a couple of hours were devoted also to students education. With a shutdown duration of 3744 hours (43%) the reliability of COSY amounts to more than 90% .

Within the FAIR related activities, one week of beam time was used in 2016 by the the external group CBM (Compressed Baryonic Matter) for detector-system tests and tests of FPGA-based read out boards. To this the radiation tolerance, i.e. single- and multiple-bit upset detection and correction methods were studied. The INT (Institut für nukleare Trendanalysen) of the Fraunhofer Institute Euskirchen spent two weeks of COSY beam time on the measurement of cross sections for single event effects on various different incident proton energies and one week jointly with the INM (Institut für Neurowissenschaften und Medizin, FZ-Jülich) for irradiation studies. The distribution of user weeks and maintenance/shutdown periods is listed in Table 3.

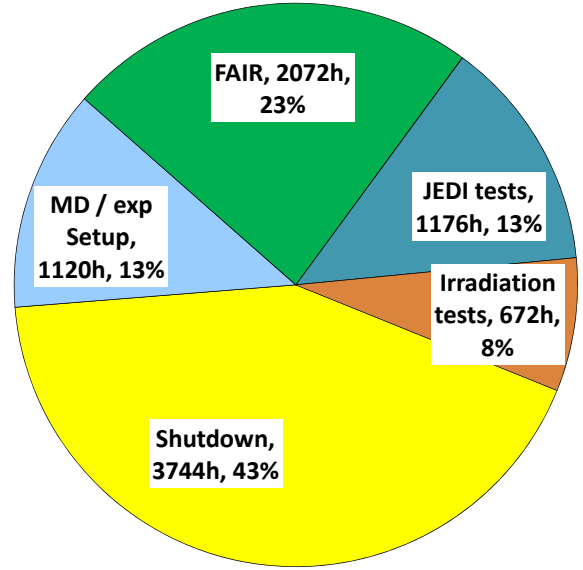


Fig. 9: COSY beam-time statistics in 2016.

Table 3: Overview COSY user beam time and EDM/FAIR weeks in 2016.

Date	Experiment	Duration	Reaction, experiment #
1.01.16.–14.02.16	Maintenance	6 week	shutdown of COSY
22.02.–28.02.	COSY	1 week	beam optics studies, Exp. A005
07.03.–20.03.	EDM (JEDI)	2 week	EDM, COSY Exp. E002
21.03.–17.04.	Maintenance	4 weeks	shutdown of COSY
25.04.–01.05.	FAIR (STT)	1 week	FAIR straw tube tracker, Exp. D002
09.05.–15.05.	INT	1 week	Irradiation measurements (INT), D006
23.05.–05.06.	FAIR	2 weeks	FAIR electron cooling, Exp. A002
13.06.–26.06.	PAX/TRIC	2 weeks	TRIC, Exp. E006
04.07.–10.07.	FAIR (MVD)	1 week	FAIR micro Vertex detector, Exp. D001
11.07.–21.08.	Maintenance	6 weeks	shutdown of COSY
29.08.–04.09.	FAIR (CBM)	1 week	CBM measurements COSY Exp. D004
05.09.–11.09.	INT	1 week	Irradiation measurements (INT), D006
12.09.–18.09.	FAIR	1 week	FAIR stochastic cooling, Exp. A001
19.09.–25.09.	HBS	1 week	High Brilliance Source HBS, Exp. A010
26.09.–16.10.	Maintenance	3 weeks	shutdown of COSY
24.10.–30.10.	FAIR (MVD)	1 week	FAIR micro Vertex detector, Exp. D001
31.10.–06.11.	INT & INM	1 week	Irradiation measurements (INT) D006 and (INM) A006
14.11.–27.11.	EDM (JEDI)	2 week	EDM, COSY Exp. E004
28.11.–04.12.	FAIR (STT)	1 week	FAIR straw tube tracker, Exp. D002
12.12.–18.12.	EDM (JEDI)	1 week	EDM, COSY Exp. E002
19.12.–31.12.	Maintenance	2 weeks	shutdown of COSY
user weeks 2016		19 weeks	
maintenance		21 weeks	
EDM & PAX/TIC		7 weeks	
FAIR		9 weeks	

2 Storage Ring Based EDM Search

The fact that we and the world around us are made of matter and only a minimal amount of antimatter is observed constitutes one of the fundamental puzzles in modern physics, motivating a variety of theoretical speculations and experimental investigations. The combined standard models of cosmology and particle physics suggest that at the end of the inflation epoch immediately following the Big Bang the number of particles and antiparticles were almost in precise balance. Yet the laws of physics act differently on matter and antimatter to generate the apparently large imbalance that we observe today. One of the necessary mechanisms required for this to happen – namely CP violation – is very small in the Standard Model of particle physics and therefore only able to account for a tiny fraction of the actual imbalance. New sources of CP violation are needed, and one such potential signature would be the appearance of electric dipole moments (EDMs) in fundamental particles.

Permanent EDMs of subatomic particles violate parity P and time reversal T symmetry. Assuming the CPT theorem, this leads to CP violation. The Standard Model allows non-vanishing EDMs, their magnitudes, however, are expected to be unobservably small with current experimental techniques. The discovery of a non-zero EDM would be a signal for new physics and could explain the matter-antimatter asymmetry observed in our Universe.

The measurement of an EDM is based on the observation of a spin precession in the presence of a strong electric field. So far, only EDMs of electrically neutral systems have been examined except the EDM of the μ lepton. It has been proposed to perform charged-particle EDM searches in storage rings, since the electric field is also the field that bends and closes the particle orbit. These experiments require a new class of high-precision storage rings built to provide improvements by orders of magnitude in the technology for polarized beam storage and measurement, as well as the knowledge of and control over the beam itself.

At the Cooler Synchrotron COSY at the Forschungszentrum Jülich (FZJ), the JEDI Collaboration is working on a series of feasibility studies for such a measurement using an existing conventional hadron storage ring. COSY, which is able to store both polarized proton and deuteron beams with a momentum up to 3.7 GeV/c, is an ideal machine for the development and commissioning of the necessary technology. As a first step, R&D work at the Cooler Synchrotron COSY has been pursued. Subsequently, a first EDM measurement (precursor experiment) of deuterons will be performed at COSY with limited sensitivity starting in 2017. In parallel a design study for a dedicated EDM storage ring is carried out.

2.1 Experimental methods to measure EDMs of charged particles

In a planar storage ring the spin precession in the horizontal plane is governed by the magnetic moment. If an EDM exists, the spin vector will experience an additional torque. The resulting vertical spin component, proportional to the size of the EDM, will be measured by scattering the particles of the stored beam at an internal target and analyzing the azimuthal distribution of the scattered particles. A coherent buildup of the vertical polarization only takes place within the time the spins of the particle ensemble stays aligned. The major challenge of such kind of experiment is a very small expected vertical component of the spin excited by the EDM and the relatively large contribution by false spin rotations via the magnetic moment. These spin rotations are caused by field and misalignments errors of accelerator elements.

The precursor experiment is based on an RF method, using a radio-frequency (RF) Wien-Filter. The idea is to look for an EDM-driven resonant rotation of the stored deuteron spins from the horizontal to the vertical direction and vice versa, generated by the RF Wien filter at the deuteron spin precession frequency. The RF Wien-Filter per se is transparent to the EDM of the particle; its net effect is a frequency modulation of the spin tune. This modulation couples to the EDM precession in the static motional E -field of the ring, and generates an EDM-driven rotation of the polarization around the radial axis.

Different approaches to measure EDMs of charged particles are proposed with an ultimate goal to reach a sensitivity of $10^{-29} e \cdot \text{cm}$ in a dedicated storage ring. For protons pure electrostatic bending fields are sufficient to freeze the spin at a magic momentum of roughly 701 MeV/c. Deuteron or ^3He EDM experiments require combined electromagnetic ring elements to freeze the spin. If the particle has an EDM along its spin direction, the electrostatic fields in the rest frame of the particles will rotate the spin into the vertical direction. This change of the vertical component of the beam polarization from early to late storage times is the signature of the EDM signal.

The main focus of the JEDI collaboration in the next years is to perform the anticipated precursor experiment at COSY with the optimum performance and to finalize the design of a dedicated deuteron EDM storage ring including the necessary prototype developments of critical hardware.

2.2 Experimental achievements at COSY

For the measurements and the results discussed below a common experimental setup at COSY has been used. A polarized deuteron beam with an intensity of approximately 10^9 particles was accumulated, accelerated to the final momentum of 970 MeV/c, and electron-cooled to reduce the equilibrium beam emittance. The beam polarization, perpendicular to the ring plane, was alternated from cycle to cycle using two vector-polarized states. An

RF cavity was used to bunch the beam during the full cycle, while after the beam was prepared, the electron cooler was turned off for the remaining measurement period. An RF solenoid induced spin resonance was employed to rotate the spin by 90° from the initially vertical direction into the horizontal plane. Subsequently, the beam was slowly extracted onto a carbon target using a white noise electric field applied to a stripline unit. Elastically scattered deuterons were detected in the scintillation detectors of the EDDA polarimeter consisting of rings and bars around the beam pipe and forming four quadrants up, down, right, and left. The corresponding rate asymmetries are used to analyze the polarization states of the beam throughout the cycle.

2.2.1 Feedback system for an active control of the spin tune

The precursor experiment requires control of the phase between the spin precession in the horizontal plane and the oscillating electric and magnetic fields in the RF Wien filter. This can only be achieved using an active feedback system. Such a system has been successfully tested in fall 2015. As the RF Wien filter was not yet available at that time, the RF solenoid has been used as reference instead. The feedback system measures the RF solenoid frequency, the COSY frequency, and the events from the polarimeter using the same time reference and determines the spin precession frequency (spin tune) and its phase to high precision (see also [PRL 115 (2015) 094801]). The phase is then matched to that of the solenoid RF frequency by adjusting the COSY frequency.

The result is shown in Fig 10. The upper plot illustrates two cases for the relative phase between the two systems: without (blue) and with (red) active feedback. After the feedback has been switched on at around $t = 90$ s, the phase has been set and kept at $\phi = \phi_{\text{set}}$ by applying corrections to the COSY RF frequency indicated in the lower plot. The feedback system uses two types of corrections: short changes to the frequency to move the phase to a certain value and long term changes to compensate drifts. The grey band in the upper plot indicates the $\pm 1\sigma$ band for the resulting phase distribution.

While the system was initially commissioned by observing a phase dependent vertical polarization build-up at low solenoid amplitudes (see IKP Annual Report 2015, section 3.2.3), it was also used to study driven oscillation of the polarization vector induced by an RF solenoid as a function of the initial phase. For this, the feedback system was first used to set the initial phase difference $\Delta\phi$ between the solenoid and the spin precession, but was then switched off, i.e. $\Delta\phi$ was not controlled while the solenoid was operated.

The spin motion is parametrized using the angle between the spin and the horizontal plane α and the phase difference $\Delta\phi$ (see Fig. 11). The behavior of the spin under the influence of the solenoid can be described using a simple geometrical model that assumes that the spin is rotated by the angle k around the z axis each turn.

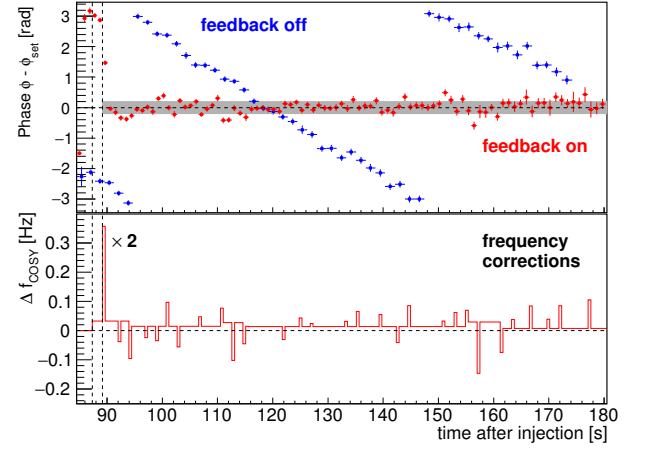


Fig. 10: Top: phase between the measured spin direction and the RF frequency of the solenoid without (blue) and with (red) an active feedback system. The y-axis has been normalized to the demand value. Bottom: the corresponding corrections to the synchrotron frequency.

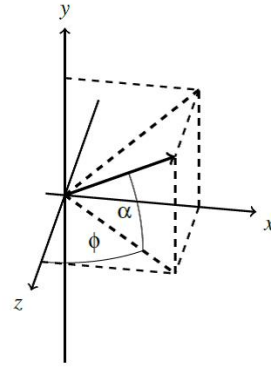


Fig. 11: Spin under the influence of an RF solenoid. The beam points in z -direction. The solenoid rotates the beam about this axis.

This leads to the following equation of motion

$$\begin{aligned} \frac{d(\Delta\phi)}{dn} &= \frac{k}{2} (\tan \alpha \sin \Delta\phi + q) \\ \frac{d\alpha}{dn} &= \frac{k}{2} \cos \Delta\phi, \end{aligned} \quad (1)$$

with $q = \frac{4\pi(v_s - v_s^{\text{sol}})}{k}$, where v_s is the actual spin tune and v_s^{sol} is the spin tune to which the solenoid is set.

The parameter q is a measure for how far the solenoid is away from the resonance frequency. Figure 12 shows some solutions for $k = 5 \cdot 10^{-7}$ and $q = 0.2\pi$. The oscillations in α and $\Delta\phi$ are typical features. It can be shown analytically that α oscillates around $-\arctan(q)$ and $\Delta\phi$ oscillates around $\pm\pi/2$. The length of one oscillation period is $\frac{4\pi}{k\sqrt{1+q^2}}$. If the amplitude exceeds a critical value depending on q , $\Delta\phi$ no longer oscillates but moves around the complete unit circle.

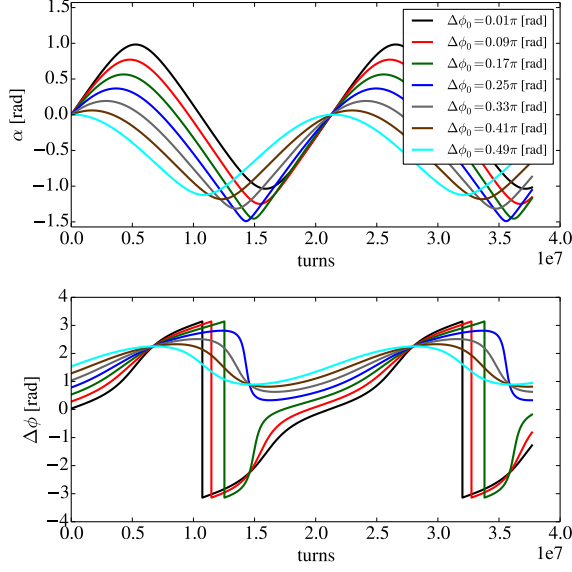


Fig. 12: Numerical solution for equation (1) for different initial conditions: $k = 5 \cdot 10^{-7}$, $q = 0.2\pi$.

This behavior was verified by fitting the numerical solution of Eq. (1) to the measured data: Figure 13 shows a run close to $q = 0$, while Fig. 14 is for a run further away from resonance.

This illustrates that the availability of an active spin tune feedback is not only an important step towards a first EDM measurement in a storage ring, but it is also a new precision tool to study the phase dependent spin dynamics in storage rings.

2.2.2 Progress in spin tune analysis

After establishing a method to precisely measure the spin tune, the analysis method was refined. It is now possible to determine the spin tune with a much simpler algorithm compared to the published method [PRL 115 (2015) 094801]. In the new algorithm a Fourier transform is performed for a macroscopic time interval of approximately 5.2 s corresponding to $4 \cdot 10^6$ turns. From the time dependence of the phase, the spin tune can be determined. Moreover, it was for the first time possible to understand the change of the spin tune versus time (or turn number). Starting point is the assumption that the spin tune ν_s follows the Rayleigh probability distribution:

$$P_{\nu_s}(\nu_s | \nu_s^{\text{ref}}, \sigma_R) = \frac{\nu_s - \nu_s^{\text{ref}}}{\sigma_R^2} e^{-\frac{(\nu_s - \nu_s^{\text{ref}})^2}{2\sigma_R^2}}, \quad \nu_s > \nu_s^{\text{ref}} \quad (2)$$

described by a shape parameter σ_R and the reference spin tune ν_s^{ref} .

Fig. 15 shows the in-plane polarization vs. turn number and phase vs. turn number for two runs with short and long spin coherence time. The black curves show simultaneous fits to the in-plane polarization and phase

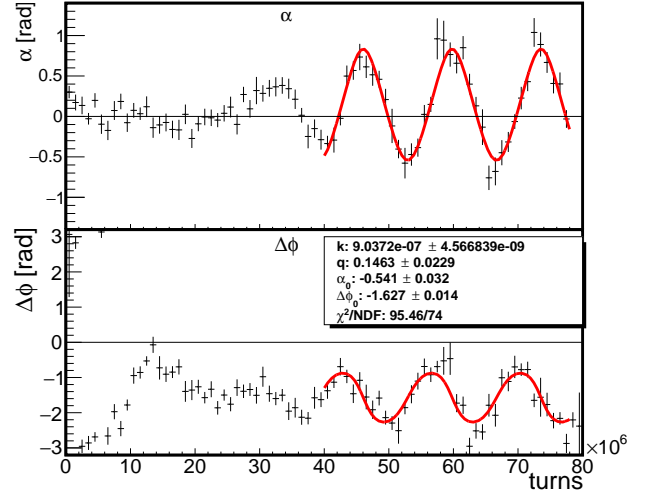


Fig. 13: Spin oscillations close to resonance. $\Delta\phi$ is oscillating throughout the cycle with a frequency proportional to the integral field of the RF solenoid.

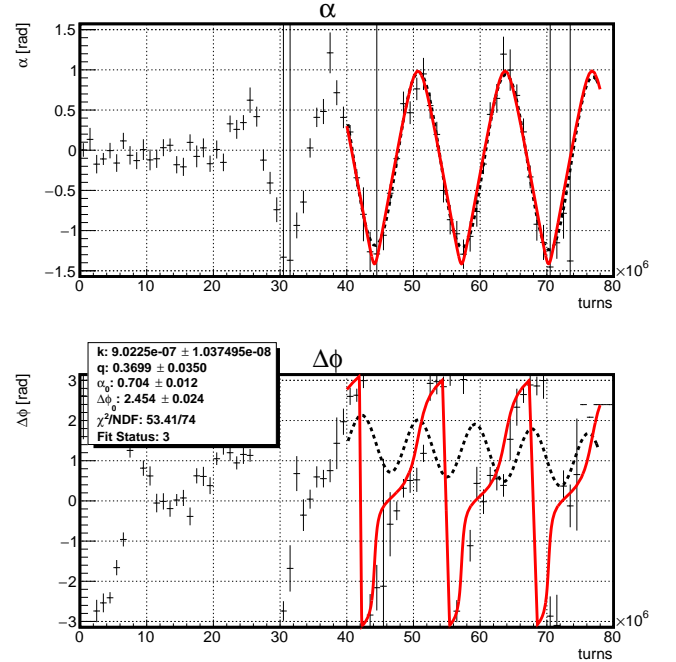


Fig. 14: Spin oscillation for a run further away from resonance $\Delta\phi$ moves over the complete angular range.

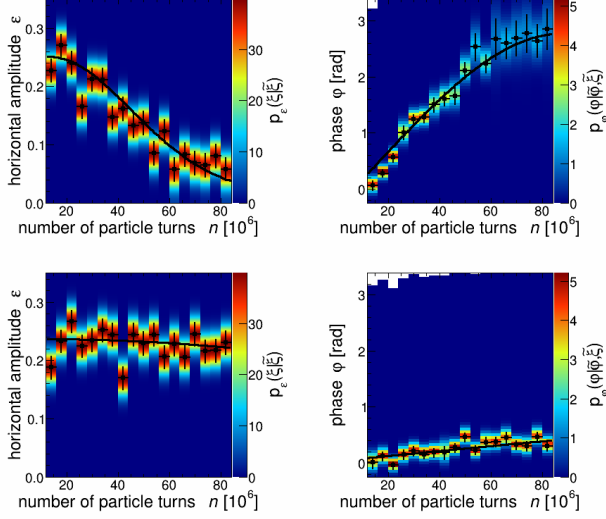


Fig. 15: In-plane polarization vs. turn number (left) and phase vs. turn number (right) for a run with short spin coherence time (top) and long coherence time (bottom). The black curves show simultaneous fits to the in-plane polarization and phase described by the single parameter σ_R .

described by the single parameter σ_R . For the two cycles shown the corresponding shape parameters are

$$\begin{aligned}\sigma_R^{\text{short}} &= (7.26 \pm 0.18) \times 10^{-9}, \\ \sigma_R^{\text{long}} &= (1.23 \pm 0.19) \times 10^{-9}.\end{aligned}$$

This can be translated to a spin coherence time:

$$\begin{aligned}\tau_{SCT}^{\text{short}} &= (49.1 \pm 1.2) \times 10^6 \text{ turns}, \\ \tau_{SCT}^{\text{long}} &= (287.1 \pm 44.4) \times 10^6 \text{ turns}.\end{aligned}$$

2.2.3 Spin tune mapping as a novel tool to probe spin dynamics at storage rings

We developed a new method to map out the spin tune response of a machine with respect to artificially introduced magnetic field imperfections. The theoretical background to this method and its experimental vindication are prerequisites to the planned precursor EDM experiments at COSY, and will also have an impact on the design of future dedicated EDM storage rings.

On the other hand, the EDM interaction with the radial motional electric field tilts the vertical stable spin axis inwards or outwards the ring. This tilt constitutes another static EDM observable, dual to the EDM-driven resonance spin rotation. Any offset and misalignment of magnetic elements in the ring produces radial and/or longitudinal imperfection of magnetic fields as well. A rotation of the MDM in these magnetic imperfections is indistinguishable from that of the EDM in a radial motional electric field. In practice, those imperfection of magnetic fields cannot readily be compensated for element by element and emerge as a principal background to the search for the EDM using an RF Wien filter.

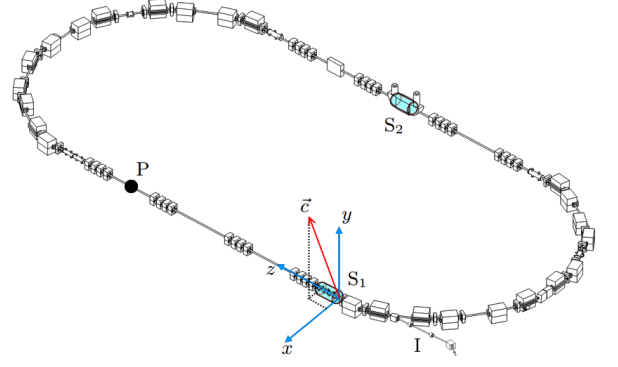


Fig. 16: Sketch of the experimental setup with two solenoids S_1 and S_2 located in the opposite straight sections of the COSY ring. The vector \vec{c} indicates the stable spin axis before the solenoid S_1 , when S_1 and S_2 are switched off. P shows the location of the polarimeter, and I indicates the injection.

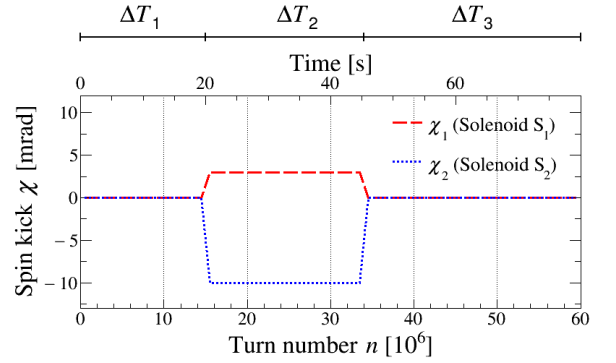


Fig. 17: Timing of spin kicks ($\chi_{1,2}$) of the two solenoids S_1 and S_2 during a measurement cycle, given for a particular pair of solenoid settings.

The ultrahigh precision of the spin tune determination can be applied to provide a diagnosis tool to quantify the magnetic ring properties. Specifically, the imperfections are known to affect the spin tune. The new technique is based on the introduction of artificial imperfections in the ring and to study the spin tune as a function of the spin kick in these artificial imperfections. Such a mapping of the spin tune response enables one to determine the orientation of the stable spin axis \vec{c} at the location of the artificial imperfections, and we report here about the first ever direct measurement of the stable spin axis in a storage ring. Preliminary results are given in [J. Mod. Phys. Conf. Ser. 40, 1660093 (2016)]. In the present experiment, the two electron cooler solenoids, placed in the opposite straight sections of COSY (see Fig. 16), have been utilized as makeshift artificial imperfections. During the beam cycle, the solenoids were switched on for 25 seconds (see Fig. 17), producing the spin rotations (χ_1, χ_2) around longitudinal axis. In the post-analysis of the spin tune for each beam cycle, we determine the spin tune jump at the time when the solenoids were switched

on. For better statistical accuracy in the determination of spin tune jump, the beam cycles with the same solenoid settings were repeated 6 times. The spin tune jump $\Delta\nu_s$, which corresponds to a particular pair of solenoid settings (χ_1, χ_2) is added to a 3-dimensional spin tune map $\Delta\nu_s(\chi_+, \chi_-)$. Then the map fits to a theory-predicted parabolic surface, which has concave (in $\chi_- = \chi_1 - \chi_2$ dimension) and convex (in $\chi_+ = \chi_1 + \chi_2$ dimension) curvature (see Fig. 18). The saddle point of the surface allows one to deduce longitudinal components of the stable spin axis \vec{c} at two positions in the ring: at the locations before the solenoid 1 and 2, assuming the solenoids are switched off and act as a drift region. Statistical accuracy in the determination of the c_z at both locations is $\approx 1\mu\text{rad}$. The data also shows the steering effect of the electron-cooler solenoids for both horizontal and vertical orbits which indicates a misalignment of the solenoids field with respect to the beam. At the present time, the analysis of possible systematic effects of spin tune jumps coming from the changes of beam closed orbit is ongoing. However, this effect does not compromise the power of the technique. The results of simulations made with COSY-Infinity will help to set the requirements for suppression of systematic effects in further EDM experiments involving a spin tune mapping.

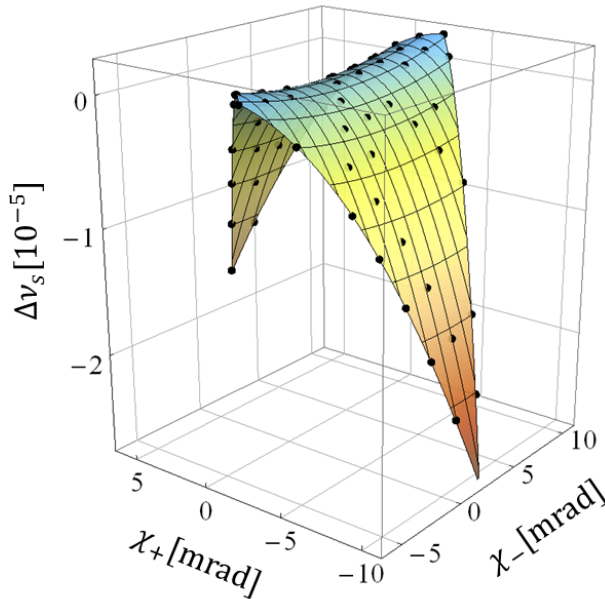


Fig. 18: Spin tune map shows the results of the measurement of spin tune jumps $\Delta\nu_s(\chi_+, \chi_-)$. Each point represents a single measurement. The error bars are smaller than the size of the symbols. A surface is fit to the data as described in the text.

2.2.4 Data base experiment in support of a deuteron EDM polarimeter

An effective deuteron polarimeter for a storage ring EDM experiment must maximize efficiency and sensitivity to

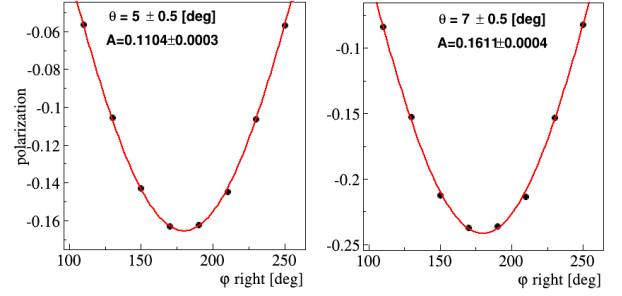


Fig. 19: Measurements of the product $p_Y A_Y$ for a series of 20° pie sections left-right pairs at two different polar scattering angles θ . The red curve is a fit to these data with the function $f = A \cos(\phi)$.

the deuteron vector polarization. Such a polarimeter is likely to be based on a thick carbon target where the spin-orbit effects in elastic scattering are large. It will be important to consider the inclusion of other reaction channels where the analyzing power is substantial and to investigate which backgrounds such as breakup have to be eliminated already at the trigger level. The data needed to optimize the polarimeter design is largely absent from the literature, so we arranged to use the scintillators and straw tubes from the WASA Forward Detector in a refurbished installation to collect the broad range of data needed at a variety of deuteron energies (170, 200, 235, 270, 300, 340, and 380 MeV). The detector stack provided full azimuthal coverage at scattering angles ranging from 4° to 17° . All single and multiple track events were recorded. Vector and tensor polarized deuteron beams were used, allowing the measurement of iT_{11} , T_{20} , and T_{22} as well as differential cross sections. Measurements were made with carbon and CH_2 ribbon targets; the CH_2 was included to provide more calibration points for the detector and a reference cross section and analyzing power for the pure carbon target. The magnitude for the beam polarization was also measured using d+C elastic scattering at 76 MeV and 40° in the Low Energy Polarimeter located in the cyclotron-to-COSY transfer line. In addition, measurements also exist at 200 and 270 MeV for both d+C and d+H scattering, so the values of the vector and tensor polarization may be checked there as well.

Online measurements of the vector polarization effect in d+C elastic scattering at 270 MeV are shown in Fig. 19. The data are of high statistical quality and behave as expected as a function of the azimuthal angle. These data match well previous measurements and the value of 0.49 for the average vector polarization between the spin up and down states. Analysis of these data has begun with the calibration of the detector responses against the expected energy loss values and the corrections for scintillator section, scattering angle, and time variations. Once completed, the data will be used in simulations of various polarimeter designs using Geant to track particles through the proposed detector elements. It is expected,

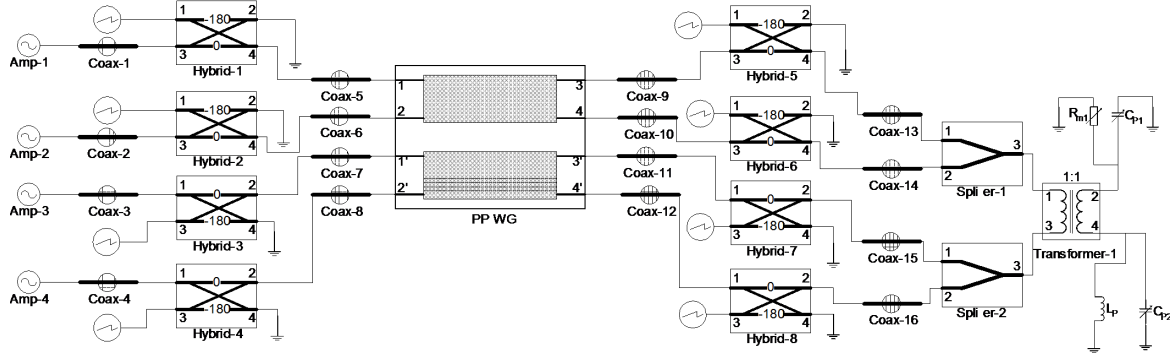


Fig. 20: The driving circuit of the RF Wien filter.

that the WASA Forward Detector will offer better angle coverage, efficiency, and polarization sensitivity, and that it may be used in place of the EDDA detector for further beam studies and the precursor experiment. This information will also guide the choice of the best energy for a deuteron EDM experiment and the design of a polarimeter for the dedicated EDM ring.

2.3 Technical developments

2.3.1 RF Wien filter development

The RF Wien filter is currently under construction and will be installed in COSY during spring 2017. After commissioning it is planned to have a first run of the precursor experiment at the end of the year. The scheme of the driving circuit of the RF Wien filter is shown in Fig. 20. On the source side, four power amplifiers are used, fed by a single signal generator. The power amplifiers are operated in push-pull mode. This means that the sources feeding the upper electrodes (labels Amp-1 and Amp-2) are in phase and they are 180° out of phase with the ones connected to the lower electrodes (labels Amp-3 and Amp-4). On each side of the device, four -30 dB power hybrids are used and connected to 50Ω terminations that emulate the current and voltage measurements devices.

Dedicated circuits are used to perform these tasks (these signals are used to adapt the operation of the RF Wien filter in real time). On each side of the electrodes, two feedthroughs are used to equally distribute the RF current providing therefore a more homogeneous electromagnetic field. At the load side of the RF Wien filter, two 3 dB combiners feeding a 1:1 transformer to which the load is connected. This forms a three-conductor system, *i.e.* two high potentials and 180° out of phase with a common ground.

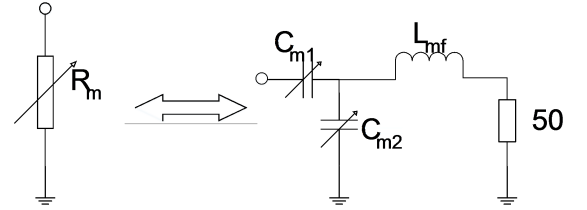


Fig. 21: The equivalent circuit of the variable resistor (left) using a T-type matching network (right).

Ideally, the load is pure resistive. A resistor does not introduce a phase shift between the voltages and currents flowing on the electrodes and therefore, the field quotient, Z_q , is expected to be real. The cables, unfortunately, add capacitive reactance to the load making Z_q complex, which corresponds to an undesired phase shift between the electric and magnetic fields. To solve this problem, a fixed inductor with two capacitors C_{p1} and C_{p2} , as shown in Fig. 20, are connected to the load. In practice, dealing with high power (10 kW) within the operating frequency range, while preserving the same levels of homogeneity, is a challenging task. The most critical part was the implementation of a stable, high-precision variable resistor at the required power level, which was realized with a matching network shown in Fig. 21. The inductor L_{mf} is fixed and is maintained at $30 \mu\text{H}$. L_{mf} is designed as an air core coil to avoid the effort of active cooling providing a maximum possible inductance of $33 \mu\text{H}$. This means that the frequency bands from 630 kHz to 1600 kHz can be covered but not the lowest operation frequency of

120 kHz. The vacuum capacitors C_{m1} and C_{m2} are characterized by very low tolerances on the order of 0.01 pF, which means a very stable and accurate system can be expected. They reside within the same rack with the inductor and they are connected via a high-current connector without any cables reducing the chances of mismatches and reflections.

2.3.2 Electrostatic deflector development

High-field electrostatic deflector development is required for a final ring with maximum field gradients of up to 17 MV/m. Ongoing development is carried out in a dedicated cleanroom laboratory at RWTH Aachen University with scaled electrode prototypes. Different materials and polishing procedures, as well as ultra-high vacuum techniques and a dark current measurement procedure were studied. Mechanically polished stainless-steel electrodes at distances of a few millimeters demonstrate the high dielectric strength close to the breakthrough conditions in ultra-high vacuum. Aluminum electrodes machined and polished with the same technique showed smaller values of the electric field strength. Nevertheless, both materials allow electrical field strength above the calculated values for a deflector prototype (17 MV/m). Good agreements with theoretical predictions of the breakdown conditions allow to continue investigations at higher voltages and larger distances between the electrodes. It will require a radiation protection laboratory, because of higher energy and intensity X-rays. The existing test bench for experiments (as shown in Fig. 22) with small deflectors will be used to develop non-destructive measurement techniques for electric-field measurements in ultra-high vacuum.

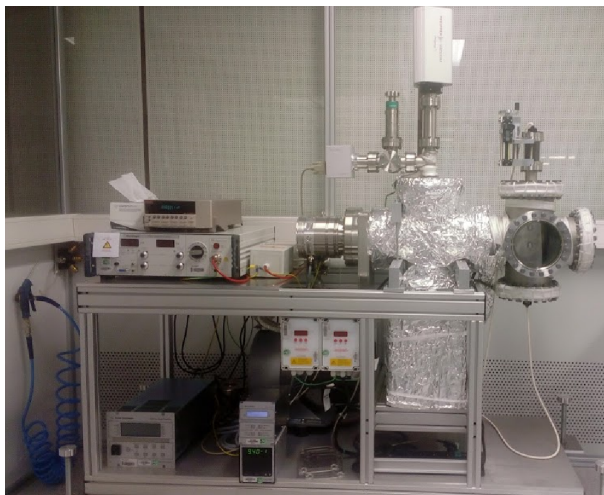


Fig. 22: The test bench for electrostatic deflectors.

This can be done with a hollow-core photonic crystal fiber developed in Max Planck Institute for the Science of Light in Erlangen. The sample of such a hollow-core fiber was provided for UHV tests at RWTH Aachen. The existing test stand was equipped with additional heating and a quadrupole mass spectrometer. The fiber was stretched be-

tween two vacuum flanges and fixed with TorrSeal epoxy. Heating tests of the fiber and hardened epoxy showed no outgassing. A measurement of the electric field using this fiber is only applicable with an oscillating voltage. Adding a sinusoidal signal with an amplitude of 1% of the main voltage should make these measurements feasible. The discharge protection scheme of the current setup was modified for this purpose.

A new signal converter box (see Fig. 23) using an external signal generator will produce a sinusoidal signal in a wide frequency range from 50 Hz up to 250 kHz.

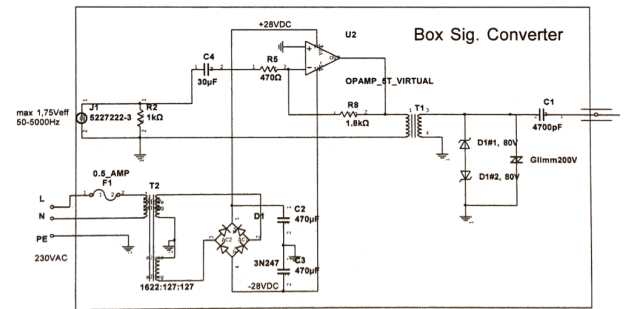


Fig. 23: Signal converter scheme for test stand.

The input voltage of the high-voltage power supply will be taken as a reference to define the modulated signal amplitude, which can be varied if necessary. New polished stainless steel electrodes (see Fig. 24) with a different surface were produced and are at present ready for installation. The special shape of the electrode on the right side of the Fig. 24 is made to test uncertainties in electrical field reconstruction.



Fig. 24: New electrodes for testing field-measurement technique.

First field measurement tests are foreseen to be completed in 2017. The result of these tests will be used to define the electrical field monitoring method during deflector operation.

2.3.3 Electromagnetic deflector design

For a proton EDM experiment, pure electrostatic ring elements would be sufficient, whereas for deuteron or ^3He EDM experiments combined electromagnetic ring elements are required. A large gap dipole magnet - ANKE

D2 - will be equipped with $1\text{ m} \times 0.1\text{ m}$ large capacitor plates. The capacitor will nominally operate at +160 kV. The average electric field strength at a gap distance of 2 cm is then 8 MV/m. The setup will be used to study the behavior of dark current in the vicinity of moderate magnetic fields. Moreover, dedicated diagnostics will be applied that detect and measure dark currents and electric fields. As the design of the electrostatic septum at COSY has proven its reliability for decades, high-voltage components from the septum have been adapted in a first approach. In contrast to the vacuum chamber of the electrostatic septum, the D2 vacuum chamber is rather small in vertical direction. The reduced distance between vacuum chamber and components that are on a high potential causes an increased electric field strength. Although the vacuum chamber is on ground potential, the field strength can locally be equal to the field strength in the gap between the capacitor plates. These field peaks are caused by the geometry, i.e. sharper geometries cause higher fields compared to smooth, round geometries. Additionally, the industry has developed new high-voltage components for medical X-ray devices. Due to the high availability of those industrial standard components and due to their reduced size, the design of the overall setup was modified in a second evolution step. In each evolutionary step the electric field distribution was simulated with software tools and afterwards analyzed and evaluated. Main criteria in the evaluation are the avoidance of field peaks. After this first major evolutionary step, design recommendations from Jan Borburgh from CERN have been considered. In the septum's design there is a component where a coil is wound around an alumina cylinder with the specific resistance of 330Ω . The coil is a protective resistor to dissipate the energy stored in the cable section between anode/cathode and main protective resistor in the event of a breakdown. The method proved its reliability, but it involves the disadvantage of having a lot of so-called triple points. Triple points are junctions between metal, vacuum, and insulator. In general, these points are considered as origin for breakdowns and therefore demand special shieldings and electric field grading. In order to circumvent these disadvantages, ceramic resistors are used, which conduct throughout the whole body. The overall design of the HV feed-through becomes much slimmer and the electric field strength is significantly reduced in these areas. The vacuum performance of the ceramic resistor was tested in a vacuum test-stand. Although the resistor stored a lot of water, the pressure was smaller than $5 \cdot 10^{-9}$ mbar after heating a few days at 300°C. The general, electric field design is finished. Engineers are working now at the detailing of the construction. Two obstacles have been found which are causing some delay of the project. The upper yoke of the D2 magnet is supported by two pillars. The pillars impede the access for the inner flange, so that the pillars have to be exchanged by a new design. The upper and lower yoke are physically connected by the vacuum chamber. Thus, the yoke must be lifted very sensitive dur-

ing the exchange in order to avoid any deformation of the vacuum chamber. The second obstacle affects the shields above and below anode and cathode. These shields are placed in vacuum and are on ground potential. The upper and lower vacuum chamber walls are also on ground potential, but deform during pumping in an unpredictable manner. The shields shall remain their shape, so that the electric field is always the same. In order to fulfill this requirement a certain bending stiffness is necessary to avoid any significant sag, but this leads to rather thick plates. Moreover, the installation and mounting of such plates is very time consuming and difficult. As the occurrence of breakdowns between capacitor plates and the shields is very likely due to the magnetic field, the shield must be easy to exchange after a breakdown. The breakdown destroys the surface with a crater that will cause further breakdowns. The latest design of the shield is a foil that can be tightened from the outside after installation. In preparation for the installation of the high-voltage components into the D2 vacuum chamber, the D2 magnet has been moved from its position in the COSY ring into the COSY eye. The ANKE target chamber has been dismantled besides the D2 magnet. D1 and D3 remain without any usage in the ring. A dummy pipe is installed in place of the D2 magnet and the target chamber. The new place of the D2 magnet allows the continuous work at the magnet even during COSY operation.

2.3.4 EDM polarimeter development

EDM experiments of charged particles, based on the storage ring method (srEDM), require a dedicated high precision polarimeter. In spite of the simplicity of the measurement principle – following the time development of the polarization vector of the particles subject to a perpendicular electric field – the smallness of the effect provides exceptional challenges, e.g., to identify and/or avoid any fake signal. This minuscule spin rotation (about $1\text{ }\mu\text{rad/s}$ for an EDM of $10^{-26}\text{ e}\cdot\text{cm}$) can be determined with the help of a polarimeter, a detector to determine the spin direction.

For these extremely precise beam polarization measurements, it is absolutely necessary to build a dedicated polarimeter which is capable to measure and control the circulating beam transverse polarization direction. The general requirements for the EDM polarimeter can be summarized as: an excellent capability to measure very low (close to zero) beam transverse polarization, to distinguish reliably useful events from accompanying background, to eliminate the systematic errors, and to operate continuously on-line with high efficiency. We have developed a new concept (see Annual report 2015, section 3.3.3) and made major steps in the R&D program towards the dedicated JEDI polarimeter. A first task of this program was to study the choice for the detector material. The experimental information collected during the measurements in lab first, and then at COSY, allowed us to construct the setup, with the modular assembly based on a standardized aluminum support structure shown on



Fig. 25: Test setup at the BIG KARL experimental area.

Fig. 25. The setup comprises of 24 LYSO modules divided into two arms, each consisting of 12 calorimeter modules (2 x 6 crystals). The LYSO crystals were obtained from the company Saint-Gobain (SG). Such a construction allows us to build the polarimeter with a different number of crystals and with a different geometrical configurations.

The measurements taken at COSY during 2016 with various types of solid targets (with different thicknesses of 5 to 10 mm), used a slowly extracted polarized deuteron beam at the BIG KARL experimental area. The goal was to investigate and optimize the performance of the DAQ and new SiPM based LYSO modules, with the aim to extract differential cross sections and vector analyzing powers for deuteron induced elastic reactions on different targets. With the help of specific target revolver, the above-mentioned physical parameters for the magnesium, carbon, silicon, and aluminum have been studied. The preliminary (on-line) result of this measurements confirm the clear identification of elastic deuteron-carbon scattering events as shown in Fig. 26. The detailed off-line analysis is in progress.

The next step will be the production run in March 2017 with the already commissioned setup and preparation of the concept for an internal polarimeter at one of the COSY straight sections. A new idea for the target design is also under investigation, based on the use of small diamond pellets ($10 \div 100 \mu\text{m}$) to sample the beam and provide a two-dimensional polarization profile of the beam's cross section. Laboratory tests of the target system elements will be the subject of the ongoing activities in 2017 as well.

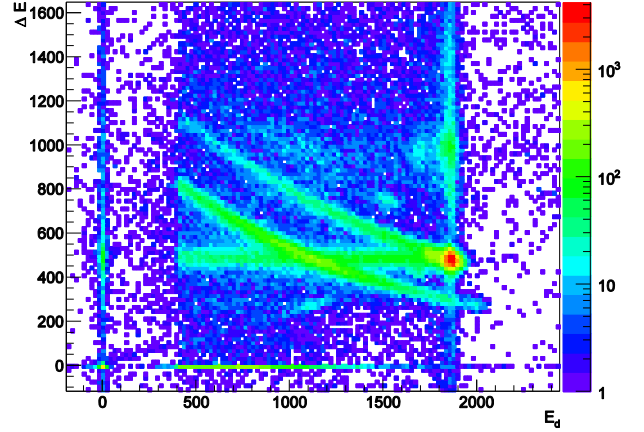


Fig. 26: A typical $\Delta E/E$ spectrum for deuterons stopped in one of the LYSO modules for a beam energy of $T_d = 270 \text{ MeV}$.

2.4 Beam and spin dynamics

2.4.1 Simulation of closed orbit influencing effects at COSY

The proposed measurement method for EDMs at COSY makes use of a RF Wien filter. Initially, the particle spins are precessing perpendicular to the stable spin direction of spin motion. To excite a spin resonance, the frequency of the RF fields is adjusted to this spin precession frequency. In an ideal storage ring, the corresponding resonance strength is directly proportional to the EDM magnitude, resulting in a slow oscillation of the vertical polarization component. To first order this oscillation is fully characterized by the slope of the vertical polarization buildup. Additional electromagnetic fields introduced by magnet imperfections and misalignments bias the observed build-up.

Assuming Gaussian distributed magnet misalignments with a standard deviation of 0.1 mm leads to a vertical closed orbit RMS of roughly 1 mm. The resulting signal corresponds to a false EDM signal of $d \approx 5 \cdot 10^{-19} e \text{ cm}$. With the current set-up of COSY, the vertical closed orbit RMS after applying an orbit correction is in the order of 2 mm. In order to reduce the contribution of a false EDM signal, its main sources must be identified. Using the MAD-X program, the effect of displaced magnets and power supply oscillations can be modeled by implementing the current COSY lattice and applying randomly distributed magnet displacements and field values.

Different sets of randomly distributed vertical shifts of the quadrupole magnets are introduced and the impact on spin motion is studied. The RMS of the vertical orbit has

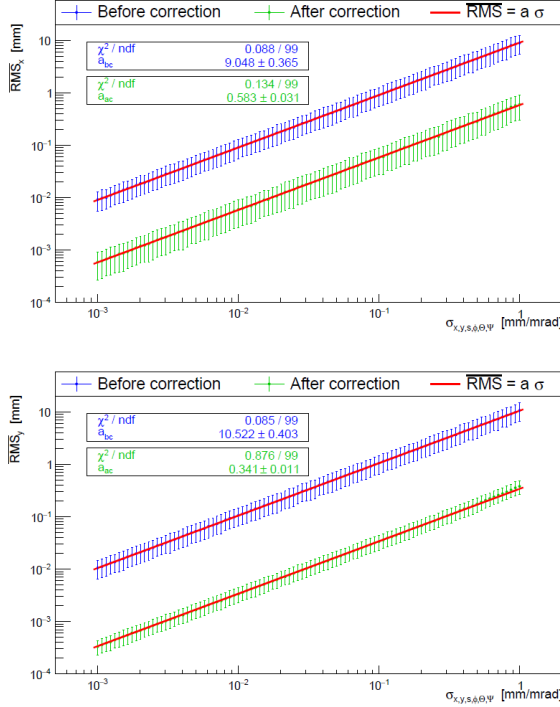


Fig. 27: Mean closed orbit RMS in horizontal and transverse direction. The blue markers indicate the results before an orbit correction is applied. The simulation results after the orbit correction are shown in green. The indicated errors correspond to the span of the values from generating magnet errors with 100 random seeds. The behavior is linear in both directions.

been used as measure of the additional radial magnetic fields. The results are shown in Fig. 27.

Additionally, the effect of residual power supply oscillations is investigated. Incorporating the generated field variations in the model and calculating the closed orbit leads to a snapshot of the dynamic scenario. By creating several of these snapshots, one can investigate the average influence of power supply oscillations on the transverse closed orbit. In the simulation 1000 closed orbits calculations, each for a different set of current values, are generated. For the reference orbit a fixed set of misaligned dipoles and quadrupoles was chosen. The deviations from the reference orbit at each beam-position monitor (BPM) are collected in a histogram for all 1000 simulations and a Gaussian fit is performed. The width of the fit indicates the influence of the field oscillation at this specific BPM. The average width over all BPMs indicates the influence on the closed orbit RMS in x- (y-) direction due to field changes caused by residual power supply oscillations. None of the RMS changes is of a larger order of magnitude than $10\mu\text{m}$. Thus, regarding the precur-

sor experiment at COSY, the residual power supply oscillations play a minor role when trying to improve the quality of the closed orbit to reach a transverse RMS of about $100\mu\text{m}$. The effects of displaced and rotated magnets dominate the effect of power supply oscillations by many orders of magnitude.

The former results show that magnet misalignments are one of the main sources of closed orbit deviations at COSY. It is therefore necessary to determine the current positions of all dipoles and quadrupoles and to correct large displacements and rotations towards the target position. A corresponding survey was conducted in April 2016 by the external company Stollenwerk. The dipoles and quadrupoles at COSY are armed with reference marks at which a laser-based position measurement according to a fixed reference point can be carried out.

Finally, the deviations of all magnets from the achieved best-fit-plane were calculated in each direction using the different reference marks. Implementing the measured magnet misalignments into the COSY model leads to the uncorrected closed orbit. The closed orbit RMS values are similar to the ones that are measured at COSY, which supports the assumption that magnet misalignments are the main source for closed orbit deviations.

2.4.2 Final ring design

The "frozen spin (FS)" and "quasi-frozen spin (QFS)" concept are investigated for a deuteron EDM storage ring. In the FS concept the spins are always aligned to the momentum vector [Phys. Rev. Lett. 93, 052001 (2004)]. The QFS concept is based on the fact that the anomalous magnetic moment has a small negative value [Yu. Senichev et al., Proceedings of IPAC 15, MOPWA044]. Magnetic and electric fields can be spatially separated with magnetic arcs and either pure electric field or combined magnetic and electric fields sections connecting the two arcs. The rotation of spin relative to the momentum in two parts of ring – the arc and the connecting sections – can compensate each other, leading a quasi-frozen spin rotation turn by turn.

Two possible options for a QFS lattice are considered and compared to a frozen spin lattice (see Fig. 28), where the elements with the combined electric and magnetic fields are used.

In the first QFS option, completely separated electric and magnetic parts are used that form a structure. In the second option, we suggest using only two magnetic arcs with two straight sections having combined straight elements with magnetic and electric fields. The straight elements have a horizontal electric field of 120 kV/cm and a vertical magnetic field of 80 mT . They provide the compensation for the spin rotation in the arc and at the same time allow having straight electric plates without the higher orders field.

This scheme could be tested in the COSY ring to prove the quasi-frozen spin concept. Obviously, this oscillation should lead to an EDM signal reduction. However, due

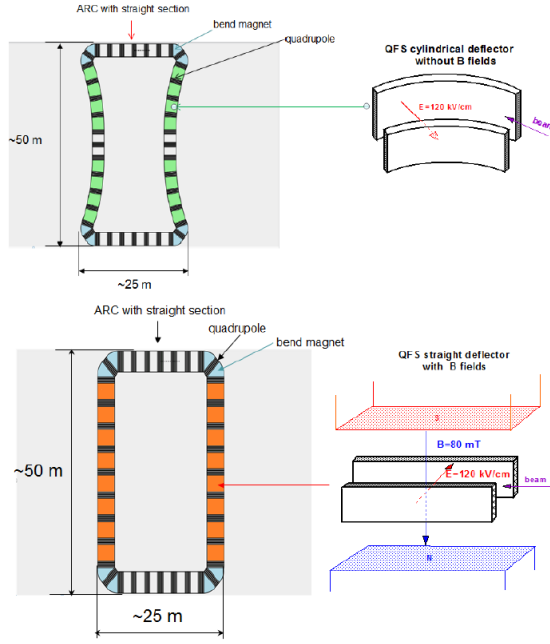


Fig. 28: Two options of QFS lattices with curved (top) and straight (bottom) electrostatic deflectors.

to the small amplitudes oscillation the EDM signal is reduced by approximately a factor of 0.98 compared the FS case. In both options, the free dispersion straight sections are placed between the magnetic arcs and are necessary to accommodate the polarimetry, the beam extraction and injection systems, and RF cavity.

Also a frozen-spin (FS) lattice has been designed based on deflectors with incorporated E and B fields (see Fig. 29). Despite the difference in the concepts, the basic parameters, namely the size of the rings, the length of the straight sections, the number of focusing periods, and the number of deflecting and focusing elements and sextupoles, all remain approximately the same.

As a special role is given to sextupoles, all structures have at least six families of sextupoles for a flexible control of spin coherence time and chromaticity in all coordinates, and each family carries out its own functions. The proposed QFS method could simplify the lattice and would allow diagnosis of the presumably existing EDM signal, but it needs to be investigated in detail from the point of view of the systematic errors.

Detailed beam and spin tracking simulations have been performed to investigate the effect of systematic errors for the EDM buildup. The influence of gradient fields in the FS lattice is negligible compared to the influence in the QFS lattice. Furthermore, these simulations including ring elements misalignments show that the largest difference of systematic EDM buildup between FS and QFS are due to longitudinal fields. The orientation of

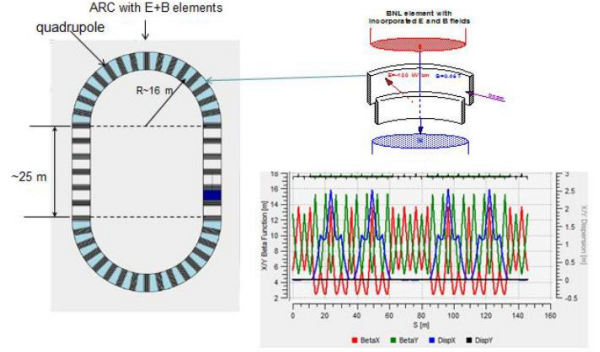


Fig. 29: FS lattices with incorporated electrostatic and magnetic fields.

the polarization parallel aligned to the beam motion longitudinal fields do not disturb the spin motion in the FS concept in comparison to the QFS concept. Therefore, most sensitive for the QFS lattice are rotations of deflectors and quadrupoles around the radial axis. As an example, the simulation results for deflector shifts are shown in Fig. 30. It is proved that for a perfect ring without misalignments the FS and QFS concept works in the same way. However, unavoidable misalignments in the ring prevent a measurement of the EDM with highest sensitivity. In connection with this the Clockwise-Counter Clockwise method, assuming a perfect reversal of magnetic fields for deuteron EDM measurements, is a certified measure to handle errors caused by rotations of the deflectors. Furthermore this method corrects the misleading effect by shifts of quadrupoles.

2.5 Summary and goals

The precursor experiment at COSY will be performed after the commissioning of the RF Wien filter in 2017. Therefore, the COSY accelerator magnets are presently aligned with a precision below 0.2 mm. One of the most important developments for this measurement is the fast feedback system for an active control of the spin tune and the progress made to analyse the spin tune. Another important tool in this context is the spin tune mapping to probe the spin dynamics in COSY and data base experiments in support of a deuteron EDM polarimeter.

The design study of a dedicated EDM storage ring is in preparation taking different concepts into account. All in all, the FS method has advantages with different kind of misalignments and artificial vertical spin build up due to the fact that the spin is frozen in comparison with the QFS method. Nevertheless the QFS method would be the right choice for an upgrade of the existing COSY ring, keeping the magnetic dipoles in the arcs and adding additional electromagnetic deflectors in the straight sections.

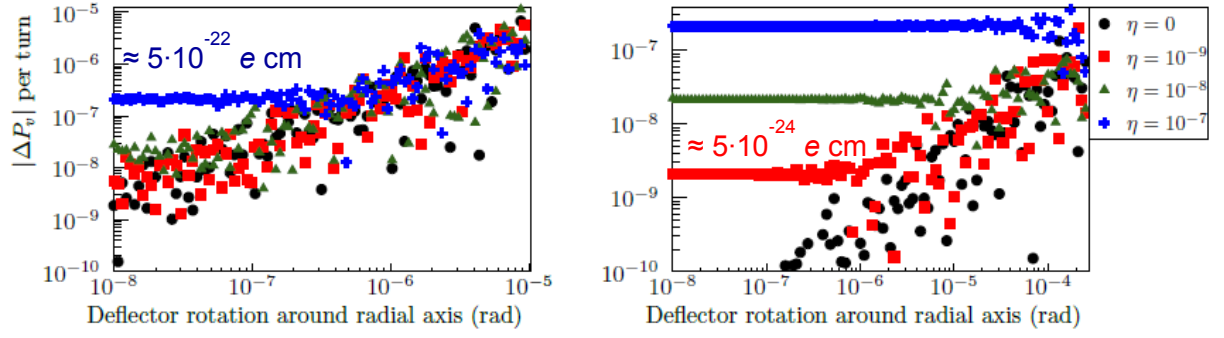


Fig. 30: Vertical spin build up for different magnitudes of EDM and Gaussian distributed rotations of $E \times B$ deflectors (RMS values) around the radial axis. Each simulation has different randomly generated misalignments and the dimensionless scaling factor η , with $\|d_{\text{edm}}\| \approx \eta \cdot 5.3 \cdot 10^{-15} e \text{ cm}$. The left shows the QFS and the right plot the FS simulation.

The JEDI collaboration is performing the necessary R&D work at COSY, prototyping critical hardware and performing dedicated beam and spin dynamics studies. High-field electrostatic field tests have been performed and ultra-high field gradients could be reached. A first design of a combined electromagnetic deflector has also been carried out.

In the upcoming years the anticipated precursor experiment has to be performed at COSY with the optimum performance and the design of a dedicated Deuteron EDM storage ring finalized including the necessary prototype developments of critical hardware.

3 The HESR at FAIR

3.1 Project status and interface to FAIR

IKP is leading the international consortium dedicated to build the HESR. It is strongly supported by colleagues from the Central Institutes for Engineering and Analytics (ZEA) of the Research Center Jülich. About 50% of the total project investment money is already either spent or bound by contract. IKP aims to have as many components ready for delivery to Darmstadt as possible during 2018 following the strategic decisions of the Board of Management of the Research Center Jülich. However, as the start of construction of the buildings at Darmstadt where the HESR components will be installed has been shifted to 2020 the acquisition of several components will have to be delayed to at least 2020. This affects e.g. vacuum pumps which then can go into operation with the warranty still active. In the case of the main dipole magnet power converter the reason is different: The site acceptance test of the power converter requires a suitable load which only can be achieved with the installed magnets. The detailed planning how to move the approx. 200 pre-assembled units into the HESR buildings has started in close co-operation with the FAIR colleagues. Presently, moving the first of these units into the HESR buildings is scheduled for 2022.

More than 230 magnets and 120 power converters are being produced for HESR. 575 m vacuum chambers are prepared for installation together with dedicated chambers with pumping ports. The beam pipes in the dipole magnets are NEG coated, will be thermally insulated and can be activated if they are heated up to 230 °C. About 1200 individual interlock and coaxial load cables are planned to connect the magnets to their power converters. To keep the vacuum pressure as low as 10^{-8} mbar about 500 pumps, 25 sectional valves, and 150 vacuum gauges are planned. All technical details and all interfaces to the building are being negotiated with the contacts at FAIR and GSI in Darmstadt. The technical follow-up is established with the producing companies and with institutions in the FAIR member states which contribute to HESR at FAIR as in-kind. New sensor and actor structures have been invented at IKP for a state-of-the-art stochastic cooling system which will allow experiments with highest beam quality and luminosity. HESR will be equipped with modern barrier bucket cavities driven by solid state amplifiers. Established user communities are (i) the PANDA collaboration for physics with antiprotons and (ii) the SPARC collaboration for heavy ion physics. To minimize the time needed for installation in the HESR tunnel, all equipment is being pre-assembled in Jülich. Approx. 200 girders will finally be needed to carry all devices. The heaviest load is the dipole magnet on its girder. It will be moved inside the storage area or inside the tunnel with remotely controlled motor driven wheels designed for a load of 40 t, see Fig. 32. To prevent damages to the vacuum vessels, the vacuum pumps will be installed once the girders are in place in the tunnel.

To guarantee stable operation of the HESR, beam dynamic simulations are performed. The stability of the beam is strongly influenced by small imperfections of the magnetic fields of the quadrupole and dipole magnets. Thus, the results of the measurements, that are carried out at the already produced magnets, are used as the basis for simulations. These simulations deliver the trajectory of single antiprotons through the HESR. With a so-called Lyapunov indicator the tracking results are categorized in stable and non-stable trajectories. The volume that contains only stable trajectories defines the dynamic aperture. If it is smaller than the geometric acceptance of the storage ring, it decreases the available volume for the antiproton beam. For the antiprotons at injection energy a tune scan has been performed, where the dynamic aperture was estimated as function of the number of oscillations of the antiprotons around the central beam orbit (the so-called tune), see Fig. 31. It reveals areas where stable particle motion can be expected, and serves as a starting point for further investigations.

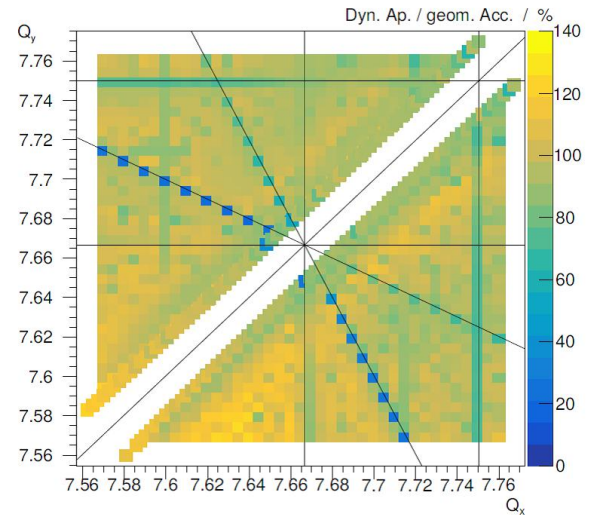


Fig. 31: Estimated dynamic aperture at different horizontal and vertical tunes normalized to the geometric acceptance. The black lines are the positions of tune resonances, where a reduced stability of motion is expected.

3.2 Magnets, power converters and radio frequency system

The delivery of dipole and quadrupole magnets is proceeding routinely. By the end of 2016 a total of 39 of 46 dipole magnets and 61 of 84 quadrupole magnets have been produced. 16 completely assembled dipole magnets could already be delivered to Darmstadt (see Fig. 32). Delivery of the last dipole magnet is expected in March 2017, last quadrupole magnet is expected in June 2017. Pre-assembly of one dipole magnet comprises (i) magnet opening, (ii) surface cleaning, (iii) attaching fixed and floating bearings for the vacuum chamber, (iv) attaching



Fig. 32: Complete HESR dipole magnet being moved to the final storage place inside the storage hall in Darmstadt. Motor driven wheels allow a denser packing than using conventional trolleys.

the heating jackets to the vacuum chamber, (v) installation of the vacuum chamber, (vi) closing the magnet, and (vii) document the chamber position relative to the fiducials on the magnet. All these steps typically take 1 week per magnet.

The pre-assembly of the quadrupole groups (sextupole, quadrupole and steerer magnets with vacuum chambers on a common girder) can start once the magnets of the Romanian In-Kind contribution arrive in Jülich. Their delivery is expected to start in Q2/2017 and to be finished in Q2/2019. Last pre-assembly in Jülich can be expected until end of 2019.

The injection dipole magnet, injection septum magnets and the chicane dipole magnets are in tendering. Bids are expected in January 2017.

The measuring machine for the multipole components of the HESR curved dipole magnets (bending radius nearly 30 m) is currently being manufactured. The measurement results will allow a detailed understanding of the particle trajectories in HESR.

The 27 power converters for the quadrupole magnet families are stored in Jülich. Until installation in Darmstadt, they have to be powered in regular intervals to avoid capacitor aging.

The power converters of the PANDA chicane dipoles have passed the site acceptance tests successfully. The acquisition of the septum power converter is launched. All power converters that can be ordered already now, have been delivered or are in fabrication or the order is close to awarding. The two power supplies of the main dipole magnets need special attention as for planning purposes the geometry of the layout has to be known early, but the delivery date depends on the finished installation of all dipole magnets in the tunnel.

The prototype power converter for sextupole and steering magnets, which is part of the Romanian In-Kind contribution to the FAIR project, has to be modified to pass the test for electromagnetic compatibility. Subsequently, the series production can be released. This is expected for Q2/2017.

Work on detailing the mechanical design of the RF system has been resumed. All other large RF components are already in stock.

3.3 Injection, beam diagnostics and vacuum

3.3.1 Injection

The test tank for the injection kicker magnets has been fabricated and tested completely together with all peripherals in Jülich. Now it has been sent to the producer of the kicker magnets and pulser to optimize the magnet and the feedthrough. The latest set-up is shown in fig. 33. The lifting and holding mechanism is surrounded by covers to avoid touching parts on high voltage. The pulser development at the manufacturer based on semi-conductor switches is close to fulfill all specifications. The most recent measurement proved operation at 35 kV / 4185 A with rise time 207 ns.



Fig. 33: Photo of the injection kicker test tank with lifting mechanism, protective covers, heating jackets, pumps, and control rack. It will be used to determine the stray capacitances and stray inductances with the magnet installed.

3.3.2 Beam Diagnostics

Efforts have been concentrated on finalizing the design of the Beam Position Monitor (BPM) and on working out the concept of ion clearing i.e. removing residual gas ions from the beam, needed for antiproton operation.

For the BPMs in the arcs a diagonally cut cylindrical design has been chosen. The BPMs will be mounted between the quadrupole and the sextupole magnets. The lack of free space in the arcs requires the BPMs to be

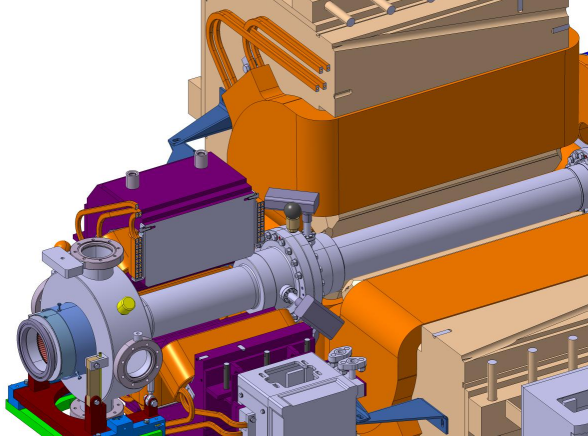


Fig. 34: Integration of the beam position monitors into the HESR arc sections. Image courtesy ZEA-1.

partially placed into the sextupole magnets (Fig. 34). The design has been optimized for acceptable signal strength for low beam intensity operation within the mechanical constraints such as overall length and outer diameter of the BPM vacuum chamber. The capacitances of the electrodes to ground as well as the ones between all electrodes were simulated using the COMSOL software. The exact knowledge of these values allows predicting the performance of the BPM. Fig. 35 shows the final design to be installed in the arc sections of the HESR.

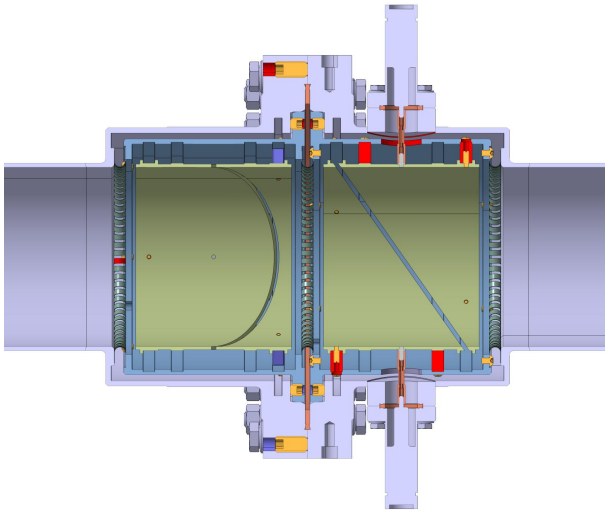


Fig. 35: The final design of the BPM for the arcs. Image courtesy ZEA-1.

Fiducial marks have been added to the design to allow accurate knowledge of the BPM position. In addition, reference pins can be inserted into the outer vacuum flanges of the BPM to allow accurate determination of the electrical characteristics on the test bench. The pickup does not restrict the aperture available to the beam. Care has been taken to provide the shortest possible path for the image current of the beam in the chamber walls.

To confirm the design parameters and to verify the performance of the series production of the BPMs a test bench has been constructed. A stretched wire is moved in X and Y planes by four linear drives. The position of the wire as well as the reference pins mounted on the outer flanges are measured by means of optical micrometers. This approach ensures high accuracy of the measurements despite possible mechanical tolerances of the wire mounting. The performance of the prototype BPM manufactured at ZEA-1 (Fig. 36) has been studied on the test bench. All design parameters could be reached.

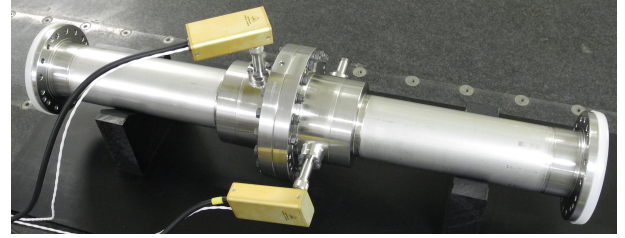


Fig. 36: A photograph of the prototype BPM mechanically designed and manufactured by ZEA-1.

The first BPM produced is expected for Q3/2017. Possibilities to design a non-destructive capacitive beam size sensitive pickup have been considered theoretically in Appendix K: "Theoretical Considerations of a Beam Position Independent Capacitive Quadrupole Pickup" by A.Halama.

To ensure adequate clearing of residual gas ions, dedicated electrodes distributed around the ring are envisaged. Each orbit correction magnet will house a widening of the beam pipe which allows insertion of clearing electrodes keeping the aperture of the HESR (89 mm diameter) unrestricted. Fig. 37 illustrates the concept of the electrode mounting.

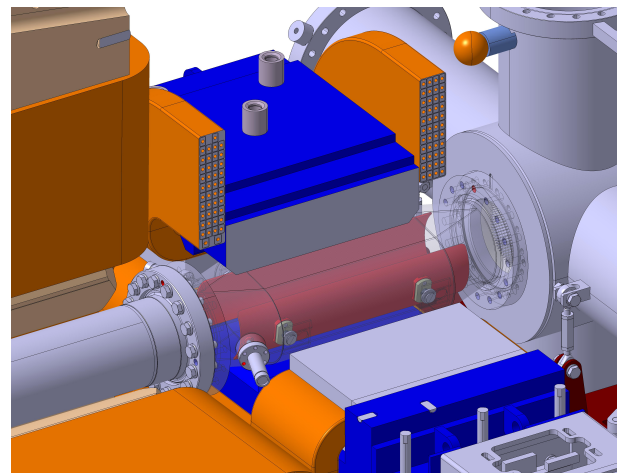


Fig. 37: The concept of dedicated electrodes for removing the residual gas ions.

Simulations using the COMSOL software have been performed to verify the ion-clearing concept.

3.3.3 Vacuum

The main topics were the vacuum control and the heating system for the arcs, the test facility for the injection kicker tank, stochastic cooling tanks as well as the coating of the dipole chambers and the series production of the pumping bodies.

All heating jackets for the dipole chambers are produced so that assembly of the dipole magnets with vacuum chamber and heating jackets could be started (Fig. 38). The manufacturing of all other heating jackets for vacuum chambers in the arc sections has started.



Fig. 38: Dipole chamber with heating jacket during installation inside the dipole magnet.

The pumping bodies are vacuum chambers with dedicated pumping ports. Their design has been finished, bids have been collected and the contract has been awarded. First delivery is announced for Q1/2017.

The series production for all alignment feet for the main magnets and their girders has started and in addition the support frames for the quadrupole-units are designed and ready for tendering.

The assembly of the stochastic cooling tanks inside the clean room with all elements and electronics is going on and finished for two of them (Fig. 39). These two are installed and commissioned in COSY already.

Both the development of the vacuum control system and the heating (bake-out) system is ongoing in close cooper-



Fig. 39: Stochastic cooling chamber (pick-up) before final installation in the clean room.

ation with GSI and is already defined for one sample section which now can be used as an example for the whole HESR.

All vacuum test facilities were reconstructed and are operating for new and final tests to finish the pump layout both of the arcs and the straights. Even the tests for the injection kicker test tank are completed and the whole test facility is transported to the producer for further tests with the magnets.

3.4 Stochastic cooling and experiment installations



Fig. 40: Installation of the first HESR pickup tank in COSY.

The stochastic cooling system of the HESR is based on completely new structures especially designed for the HESR. Each slot, surrounding the circulating beam, of these so called slot-ring couplers covers the whole image current without a reduction of the HESR aperture and without any plunging system. One pickup and one kicker have been already assembled in the clean room of ZEA-1. The second pickup of the main stochastic cooling system is currently in the clean room for final assembling. Experience is that the assembly of each stochastic cooling tank



Fig. 41: Installation of the first HESR kicker tank in COSY.

takes 6 months which leads to summer 2019 for finishing the last cooling tank.

The series production of the high power amplifiers (2-4 GHz) based on GaN has started. The first two amplifiers are expected in January 2017 and an additional pair in February. After installation of these four amplifiers the complete feedback loop can be commissioned at COSY. The first HESR pickup was installed during the winter-shutdown 2015-2016 replacing the vertical pickup of the old COSY stochastic cooling system. The first HESR kicker was installed during the summer shutdown 2016 (Fig. 40, 41).

The inner structure of the pickup was cooled down to less than 20K within 10h. Although the tank is not bakeable the vacuum quickly reached $5 \cdot 10^{-10}$ mbar.

During a beam-time in September 2016 Schottky spectra of each output in the frequency range 1.5 - 4.5 GHz were taken. Figure 42 presents the transverse sidebands measured with only $8 \cdot 10^8$ particles.

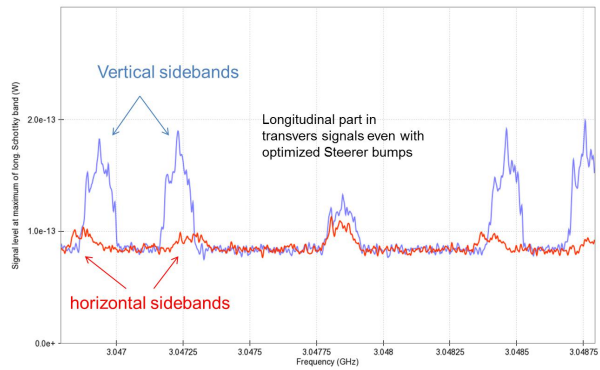


Fig. 42: Transverse sidebands as measured with a single module of the first HESR pickup tank in COSY.

Each single output of the various groups has been measured in the whole frequency range. The signal combinations including the programmable delay-lines to cover the whole HESR energy range were tested successfully, see Fig. 43.

The original plan to equip the last cooling tank with structures for a 4 - 6 GHz cooling system has been abandoned in favor of new structures for lower beta values. The gain

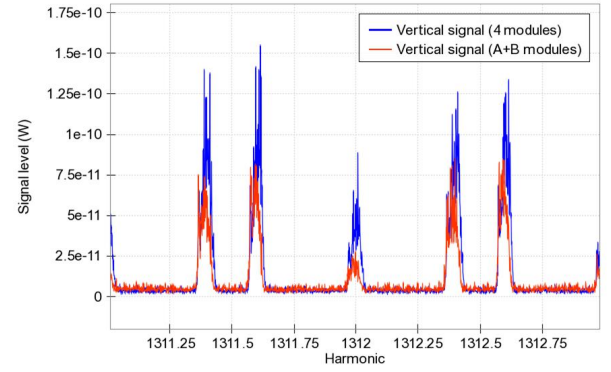


Fig. 43: Measured side bands and longitudinal signal at the 1312th harmonics. The red line shows the sum of the signals of 2 modules, the blue line shows the sum of the signals of 4 modules.

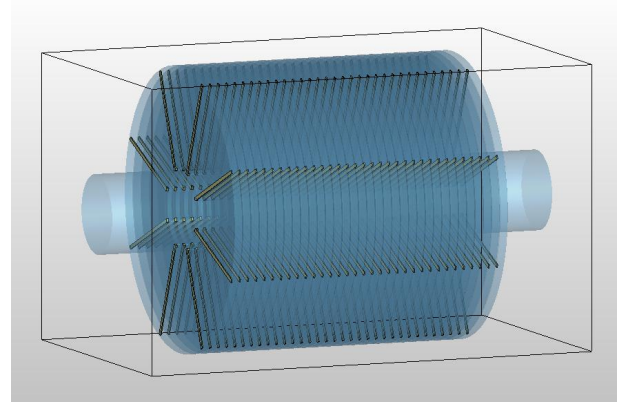


Fig. 44: First layout of the low beta cooling structure.

in cooling time turned out to be too small compared to the advantage to have a cooling system available for slower particles.

The new HESR stochastic cooling system (as well as the old COSY one) was designed for a minimum proton momentum of at least 1.5 GeV/c. Slower particles as e.g. heavy ions in HESR or deuterons in COSY can only be cooled with structures of high sensitivity in the low frequency band of 400 - 800 MHz. These new structures have been developed based on the slot-ring couplers of HESR. Since the structures get much bigger in comparison to the HESR 2-4 GHz version, mechanical properties and a matching between electrical properties, cooling performance and constructability was considered. The structure has been optimized using CST microwave studio. The first layout is shown in Fig. 44.

Shunt impedance from the electro-magnetic calculations together with typical (in the case of COSY: EDM-) beam parameters has been used as input data for the cooling simulations. Two different programs offer good cooling performances at very moderate RF power levels. Both programs show comparable results.

The plan to use optical fibers to close the feedback loop had to be modified: A conventional mode fiber would

transmit the light only with a speed of 60% of the vacuum value. Hollow fibers instead will bring back the system into feasibility, otherwise the corrections signal would arrive too late at the stochastic kicker.

3.4.1 Experiment Installations

The magnets for the PANDA chicane are in tendering. Bids are expected in January 2017. The corresponding power converters are already on site.

For the SPARC collaboration the two missing-dipole drifts on the western side of HESR are reserved. Two dipole magnets will need dedicated vacuum chambers with an inlet for a laser beam. This triggers modifications to the yoke of adjacent quadrupole magnets. This modification will be applied to the eastern quadrupole magnets on symmetric positions as well. The basic layout of the SPARC installation as used presently in the ESR synchrotron at GSI is shown in Fig. 45

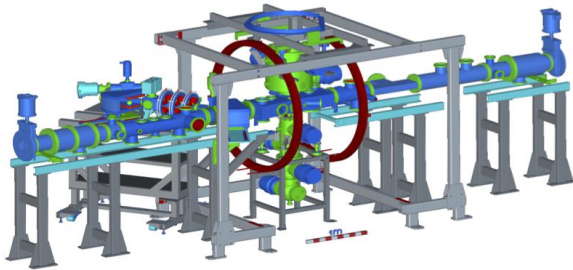


Fig. 45: SPARC experiment set-up as used presently in the ESR synchrotron at GSI.

4 The PANDA Experiment at FAIR

The future Facility for Antiproton and Ion Research (FAIR) will be one of the largest accelerator facilities in the world giving access to new experiments to gain insights into the structure of matter and the evolution of the universe.

The antiProton ANnihilation at DArmstadt (PANDA) experiment is one of the main experiments of FAIR. It will utilize the intense anti-proton beam with excellent momentum resolution provided by the High Energy Storage Ring (HESR) to perform precision measurements in the charmonium energy regime to improve the understanding of Quantum Chromo Dynamics.

In this regime many new and unexpected hidden and open charm states were found in the last decade where the nature of many of these states is not clear. Prove was found that at least some of the new states are exotic particles with more than three valence quarks. To distinguish the various theories about their origin a precise knowledge of mass and width is important. Here PANDA is the only experiment in the world which will be able to determine the width of these states down to 50 keV, compared to an upper limit of a few MeV now.

One challenging aspect not only in the analysis of the small charmonium-like states is the separation of the signal events from the huge background. To develop the needed algorithms and to determine the performance of PANDA once the experiment is running an intense simulation program is ongoing. One very complex measurement is the determination of the form factor in the decay $D_s^+ \rightarrow e^+ \nu_e \eta$. For this measurement all components of PANDA are of equal importance: Due to the neutrino in the decay chain which cannot be measured in the detector, all other involved particles have to be reconstructed, high resolution energy measurements of the involved photons are needed, and precise tracking of the charged particles to determine the decay point of the D_s mesons.

The IKP is one of the main institutes inside the collaboration developing tracking detectors for PANDA. The first tracking detector it is involved in is the Micro Vertex Detector (MVD) which sits directly around the interaction point to determine the primary and secondary vertices of charged particles. In 2015 a new front-end ASIC called PASTA was produced which was tested in detail in 2016. The second tracking detector is the gaseous Straw Tube Tracker (STT) which surrounds the MVD and covers a much larger volume to precisely measure the momentum of charged particles.

The complete data-set of PANDA has to be processed online to select only those events which are physically interesting for permanent storage. In this way the amount of data should be reduced by a factor of 1000 down to about 1 PByte per year. The processing of the data has to happen with the same speed as the data is produced with about 200 GByte per second. One very time consuming aspect of the processing of the data is the finding and fitting of charged particle tracks. To improve the processing

speed dedicated online algorithms are under development with the goal to run on parallel processing hardware like GPUs.

4.1 Feasibility study to measure the $D_s^+ \rightarrow e^+ \nu_e \eta$ decay form factor

In order to measure the semileptonic $D_s \rightarrow \eta$ decay form factor $f(q^2)$ ($q^2 = M^2(e^+ \nu_e)$), the $\bar{p}p$ interaction has been simulated to evaluate the performance of the PANDA detector. The simulated decay chain is: $\bar{p}p \rightarrow D_s^+ D_s^-$; $D_s^+ \rightarrow e^+ \nu_e \eta$; $\eta \rightarrow \pi^+ \pi^- \pi^0$; $\pi^0 \rightarrow \gamma \gamma$ with two tagging modes for the D_s^- , i.e. $D_s^- \rightarrow K^+ K^- \pi^-$ (A) and $D_s^- \rightarrow \pi^+ \pi^- \pi^-$ (B). After all selections and fits, the reconstruction efficiency of q^2 is 0.6% in tag mode A, and 0.9% in tag mode B. With these results, the count rate of useful events to measure $f(q^2)$ is estimated to be about 52 events in 35 days for a luminosity of $2 \times 10^{32} \text{ cm}^{-2} \text{ s}^{-1}$. The statistics of tag mode A is $\sim 40\%$ lower than in tag mode B. This is for two reasons. One is that the acceptance of pions is about 10% higher than for kaons, which has been seen in the reconstruction of D_s^- . The other is the remaining combinatorial background in the vertex reconstruction of $D_s^- \rightarrow \pi^+ \pi^- \pi^-$.

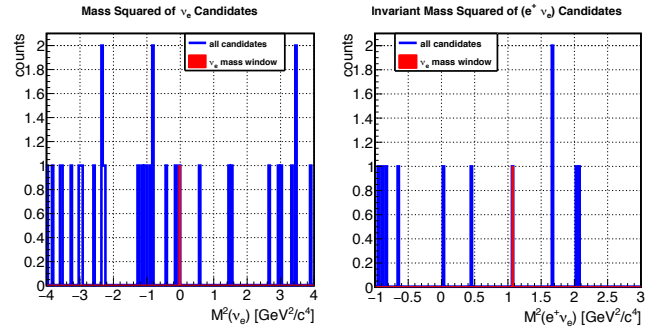


Fig. 46: The mass squared distributions of the reconstructed $(e^+ \nu_e)$ in $\bar{p}p \rightarrow \text{everything}$ events for tag mode A. Left: mass squared distribution of ν_e candidates in tag mode A. Right: invariant mass squared distribution of the lepton-neutrino system. In both figures, the blue line shows the distributions of all candidates; the red solid histogram indicates the distribution after applying a cut of $|M^2(\nu_e)| \leq 0.1 \text{ GeV}^2/c^4$.

100 million events of $\bar{p}p \rightarrow \text{everything}$ contains about 50 events of $\bar{p}p \rightarrow D_s^+ D_s^-$, assuming the cross section is 20 nb. Considering the branching ratio of $D_s^+ \rightarrow e^+ \nu_e \eta$ is 2.67%, there are around two ν_e events generated. On the side of reconstruction, only one candidate of ν_e and the $(e^+ \nu_e)$ system was found after all selections (as shown in Fig. 46). In tag mode B, 80 candidates were constructed. Considering the reconstruction efficiencies of q^2 mentioned above, the ratio of signal to background rates is found to be $S/B \approx 1/80$ for tag mode A, and $S/B \approx 1/4400$ for tag mode B. It is estimated that a cut

on the distance between D_s^- and D_s^+ , i.e. $|\Delta Z| \leq 0.1$ cm, might help to suppress the background events. More simulated background events are needed to study the background suppression in more detail.

4.2 Silicon strip readout chip ASIC

At the end of 2015, the first prototype of the ASIC designed to read out the strip part of the MVD, called PASTA (PANDA strip ASIC), has been produced and received from the foundry. Together with the collaborating institutes, a PCB (printed circuit board) to host the ASIC has been produced and integrated into the existing readout chain: the Jülich Digital Readout System (JDRS). A set of data analysis tools, together with automatic routines to test the ASIC channels one by one, have been developed in order to study the performances of PASTA. A campaign of detailed measurements has started and is currently ongoing. The quantitative results are very promising. In fact, they show that the working principle of the ASIC is functioning as expected. PASTA can be successfully connected, configured and controlled using the read out elements. The data output can be successfully read out and decoded for further analysis.

As an example, Fig. 47 shows the time over threshold as a function of the pulse amplitude for a test signal injected into the ASIC time-to-digital converter (TDC), for a specific channel. The trend is linear as expected and the data points are affected by a very small statistical uncertainty. This result shows that the front-end part of the ASIC is behaving as designed. More quantitative results will be obtained after measuring the intrinsic resolution of the TDC and calibrating the input signal.

The intrinsic digital time resolution of the ASIC is 6.25 ns, at the maximum nominal frequency of 160 MHz. A finer resolution, below 50 ps, can be achieved using a timing interpolation technique. To verify that the designed values are actually achievable, time resolution measurements have started. The first tests, on single optimized channels, show an achievable value of approximately 48 ps.

In the upcoming months the study of the performances of PASTA will continue, in order to get more quantitative informations on the behavior of the ASIC, with the aim of establishing if the prototype fulfills all the requirements imposed during the design phase.

4.3 Online tracking on GPUs

Online particle track identification and reconstruction is an essential step of the PANDA DAQ scheme, since track information is used as input in all following phases. Online tracking algorithms must ensure a delicate balance between high tracking efficiency and quality, and minimal computational footprint. To fulfill these requirements, a massively parallel solution exploiting multiple Graphic Processing Units (GPUs) is under investigation. The activity of the group is focused on devel-

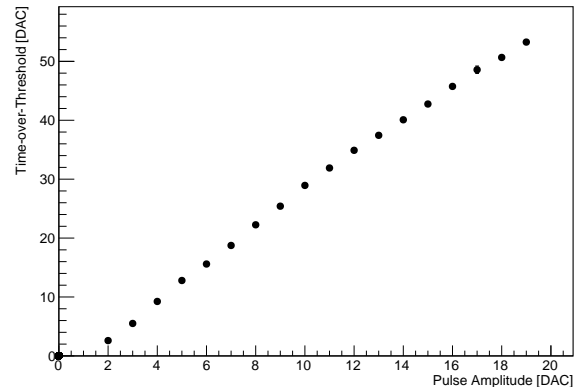


Fig. 47: Time over threshold as a function of the pulse amplitude of the incoming signal.

oping algorithms using PANDA's central tracking subsystems, the MVD and the STT, and their implementations for parallel hardware processors such as CPUs (multicore/multiprocess) and GPUs using C++, CUDA and OpenACC.

Circle Hough algorithm The Circle Hough (CH) algorithm is based on the Hough Transform, an image processing algorithm used to find instances of a given shape within an image. The main idea behind the CH is to generate, for each hit in a given input set, all possible tracks compatible with the hit. The resulting track parameters are collected in an accumulator array (AA), representing the Hough space. Peak values in the AA, where many track parameters cluster, correspond to real tracks in the input hit set. The main advantages of the CH are its good track finding efficiency, even for tracks with lower transverse momentum, and the possibility of operating in parallel on single hits. This aspect is particularly important for the application on GPUs, as exposing additional layers of parallelism makes it possible to exploit the full capabilities of the GPU programming paradigm.

Variants of the circle Hough algorithm Currently, the development is concentrated on two variants of the CH algorithm. The first is based on the same single-hit approach as the original CH, but calculates the track parameters in a more direct way, leveraging properties of the geometric locus of the hit-track compatibility condition, and using a grid-based approach for the sampling of the Hough space, instead of generating and then accumulating separate sets of values for each hit. The resulting AA is thus both easier to create and to process in the peak finding phase.

The second is based, in contrast with the original version, on tracks compatible with a pair of hits. The hit-track condition can be solved analytically, both exactly and with approximations. A simple selection criteria, based on the angular distance between hits in the transverse plane, eliminates spurious combinations before the

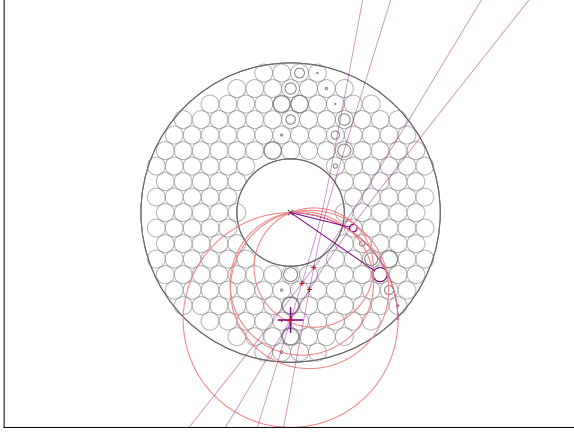


Fig. 48: Circle Hough algorithm, hit pair variant, showing one example hit pair (purple) and all possible tracks compatible with it (red). In light purple, the track center loci for the two hits in the pair are shown. The centers of each track (red marks) lie on their intersections. The large purple mark indicates the center of the true track.

AA is created. The different structure of the AA makes it possible to use simpler, and thus more efficient, criteria for the peak finding.

Results and outlook Preliminary results show that both versions of the algorithm match the reconstruction performance of the previous versions. All versions of the algorithms depend on parameters which can be tuned *ad hoc* to match different requirements in reconstruction and computing performance for different stages of the data processing chain. A more detailed performance analysis, using the samples and the tools integrated in the PandaRoot software framework, is currently ongoing. Implementations of the algorithm targeting both CPU and GPUs, optimized for computing performance, are planned for a subsequent step.

4.4 The straw tube tracker

In 2016 a new experimental area in the former COSY-TOF beam area was set up. This new experimental area required new installations of the various test detector systems, cable routing, supply and network lines. Two PANDA-STT test systems and one PANDA Forward Tracker prototype detector were installed in the beam line with a height of about 2 m. Additional Multi-Wire Proportional Chambers, a GEM chamber, straw stations and various scintillators measured the beam profile, emittance and beam intensity. Fig. 49 shows the setups in the new beam line.

An important topic of the beam tests for the PANDA-STT is the determination of the particle identification (PID) capabilities by a measurement of the particle specific energy-loss (dE/dx) in the straw gas which is a non-standard application for straw detectors, in particular



Fig. 49: Installation of the test systems in the former COSY-TOF beam area. The beam enters from the back.

for the challenging PANDA environment of high particle rates, broad momentum range and all particle species involved. The PID task of the STT is the separation of the protons, kaons and pions in the momentum region below 1 GeV/c. The same dE/dx range is covered by the proton and deuteron beams at COSY in the momentum range from about 0.5 to 3.0 GeV/c, which makes the COSY beams an ideal test facility.

Two different readout methods are under study to measure the drift time and dE/dx of a particle track. One method consists of a signal pulse shape sampling by an ADC and FPGA-readout of the pulse leading edge time and integrated pulse shape. The straws are directly connected to coax-cables and the amplifier circuit, ADC and FPGA readout, developed by ZEA2, are located backend. This solution minimizes the electronic components and required space at the detector front-end side.

The other method uses a new application-specific PANDA-STT Readout Chip (PASTTREC), design by the AGH University of Science and Technology Krakow to measure the signal leading edge time and the signal time over threshold for the dE/dx information. The front-end mounted ASIC is readout and controlled by FPGAs on Trigger Readout Boards, version3 (TRB3) design by GSI.

The decision which will be the final readout system for the PANDA-STT will be based on the performance results, like time and dE/dx resolutions. The first beam tests in 2016 consisted of one week proton beam in April with momenta of 3.0, 1.0, 0.75 and 0.55 GeV/c and one week of deuteron beam in December with momenta of 1.5, 0.75 and 0.6 GeV/c. With both beams a broad dE/dx range from about 5 to 50 keV/c was covered. Fig. 50 shows as an example for the ASIC/TRB3 readout and a 144 straw setup the measured separation by the time-over-threshold for the four different proton beam momenta.

The next step is to set up test systems and pre-series readout systems with some 100 straw channels for both methods and perform a dedicated test campaign with proton

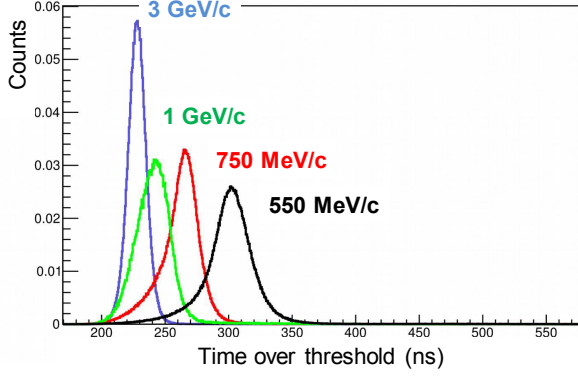


Fig. 50: Separation of the proton beam with four different momenta by the time-over-threshold measurement.

and deuteron beams at COSY to gain a clean and reliable data basis for the final readout decision.

4.5 The phase-0 straw trackers together with HADES

The advanced state of the production and developments for the PANDA-STT makes it possible to use components of the detector system in an already existing experiment installation, prior to the final installation of the STT at PANDA in the experiment hall at FAIR in the year 2023. HADES is a well-established experiment for hadron physics studies and will start a phase-0 experiment program at the SIS 18 synchrotron at FAIR with the first beam operation expected by the end of 2018. The physics program consists of proton scattering on protons or nuclear targets (A). In particular, the study of the hyperon structure by measuring radiative hyperon decays ($p(A) \rightarrow Y X \rightarrow \Lambda e^+ e^- X$, with Y =any hyperon, X =rest) is of interest and well connected to the PANDA physics program.

A proposal to upgrade the existing HADES detector system with two new PANDA-type Straw Tracker Stations (STS) in the small polar-angle forward region was worked out in 2016 and approved by both, the PANDA and HADES collaborations. The tasks of the new STS will be the reconstruction of particle tracks in the small polar-angle region up to 6.5° , whereas the HADES system measures the di-leptons and mesons emitted under larger polar angles. Fig. 51 shows the HADES setup with the two new straw stations.

The station STS1 consists of 640 straws, arranged in four double-layers which are oriented at azimuthal angles of 0° , 90° , 0° and 90° . The straw length of 766 mm allows to use the modules (each containing 2×16 straws) later also in the Forward Straw Tracker Station FT3 and FT4 at PANDA. The active area will be about $750 \times 750 \text{ mm}^2$. The station STS2, covering a larger active area of about $1130 \times 1130 \text{ mm}^2$, consists of 896 straws, each with a length of 1250 mm and arranged in four double-layers at

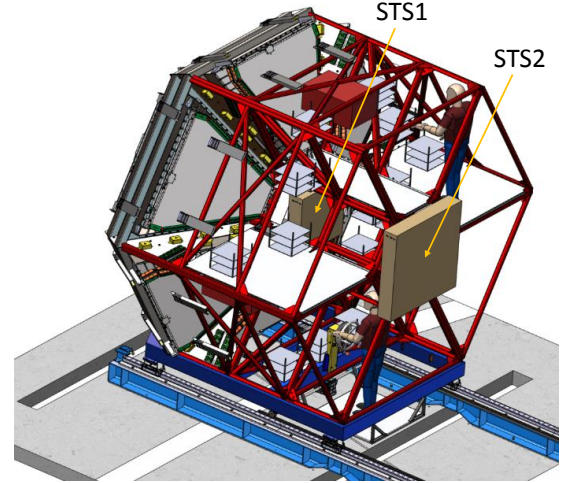


Fig. 51: Sketch of the HADES apparatus with the proposed two new straw tracker stations (STS1, STS2) in the forward region. The beam enters from the left.

azimuthal angles of 0° , 90° , $+45^\circ$ and -45° . The modules, each with 2×16 straws each, can be used later in the Forward Stations FT5 and FT6 at PANDA. Fig. 52 shows a sketch of the STS stations, with a distance of 160 cm to each other and about 315 cm distance of the STS1 to the target at HADES.

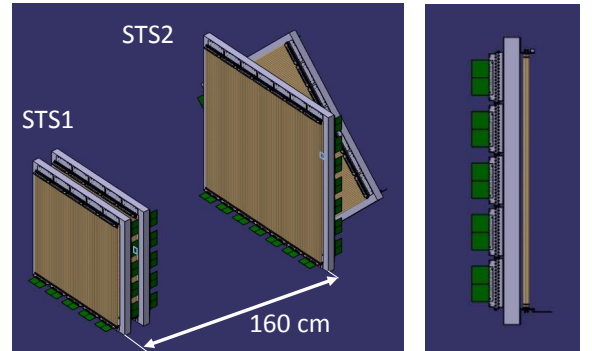


Fig. 52: Sketch of the two straw stations STS1 and STS2 and view from top on one double-layer with the front-end electronic cards (in green).

A simulation of the proton beam scattering on a carbon target yielded an expected count rate of 128 reconstructed radiative hyperon decay events per day ($\Lambda(1520) \rightarrow \Lambda e^+ e^-$). The Λ -tagging by the $\Lambda \rightarrow p \pi^-$ decay particles in the forward STS station increased the count rate by a factor of 2.5 compared to the event reconstruction with the HADES spectrometer alone.

The electronic readout and data-acquisition system consists of front-end boards containing the PASTTREC-ASIC and TRB3 readout boards. Readout systems containing the same components are currently being set up for a PANDA-STT pre-series detector and PANDA Forward Tracker (FT) prototype detector. The systems will

become available for the STS detectors in 2018, after the completion of the STT pre-series and FT prototype tests. The construction, assembly and installation of the STS detector system will be carried out together with groups in Krakow, Orsay and Uppsala. The contributions of IKP-1 are the STS1 assembly, including the production of the 640 straws, and the electronic readout system for both STS stations. The STS2 will be assembled in Krakow by the PANDA-FT group. Due to the large exploitation of synergies with the PANDA STT and FT projects, the production time for the STS system will be rather short and the installation at HADES is scheduled already for the end of 2018. The experiment measurements at the SIS 18 beam are planned for the years 2019 to 2021, typically with a few weeks beam time each year.

4.6 KOALA at HESR

One challenge of the PANDA experiment is to achieve a precision of 3% of absolute luminosity determination by using antiproton-proton elastic scattering as reference channel. It is limited by the available data of antiproton-proton elastic scattering differential cross section in the relevant beam momentum range of PANDA. Therefore, the KOALA experiment at HESR has been proposed to provide the required knowledge of antiproton-proton elastic scattering. The KOALA experiment will measure a large range of the squared 4-momentum transfer t -distribution of antiproton-proton elastic scattering in order to determine the parameters of total cross section σ_{tot} , the ratio, ρ , of the real part to the imaginary part of the forward elastic scattering amplitude and nuclear slope B , thus the differential cross section.

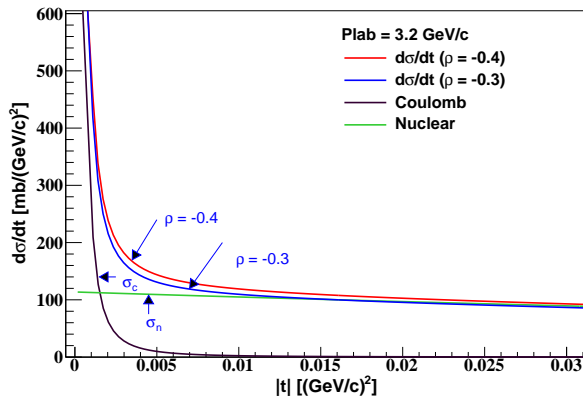


Fig. 53: Calculated contributions of differential cross section of proton-proton elastic scattering at 3.2 GeV/c with typical values of σ_{tot} , ρ and B . The difference of differential cross sections for $\rho = -0.4$ and $\rho = -0.3$ are indicated by arrows.

It is clearly indicated in Fig. 53 that the parameter ρ is most sensitive in the CNI (Coulomb Nuclear Interference) region of t -distribution. Therefore, the KOALA experiment should be able to measure the t -distribution

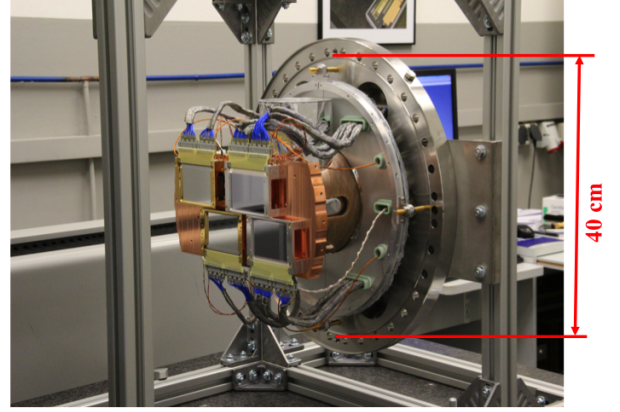


Fig. 54: Recoil detector assembled for a beam test at COSY.

covering the CNI region. The Koala experiment was designed to measure the scattered beam particles at forward angles by tracking detectors and the recoil target protons near 90° by energy detectors. The PANDA luminosity monitor detector can be used for the forward measurement and the recoil protons will be measured by a recoil detector. The forward measurement will track the scattered antiprotons. The recoil detector will measure both the kinetic energy and the polar angle of the recoil protons since t is directly proportional to the proton's kinetic energy T_p , i.e. $|t| = 2m_p T_p$. The recoil detector will measure the energy of the recoil protons within an angular range (recoil angle defined as $\alpha \equiv 90^\circ - \theta_{\text{lab}}$) $0^\circ < \alpha < 19^\circ$.

One of the recoil arms of the KOALA experiment has been designed and built. A picture of the recoil detector as used for the commissioning is shown in Fig. 54. Two silicon strip sensors with dimensions of 76.8 mm (length) x 50 mm (width) x 1 mm (thickness) have been placed at about 1 m from the target to cover the recoil angles, $\alpha = 0^\circ - 5.7^\circ$. Each silicon detector has 64 strips with 1.2 mm pitch. In addition, two germanium strip detectors with 5 and 11 mm thickness have been set up in 2 rows as well. Both germanium detectors have 67 readout strips and a strip pitch of 1.2 mm in a sensitive area of 80.4 mm (length) x 50 mm (width).

In order to validate the proposal of the KOALA experiment the recoil detector was commissioned at COSY by measuring proton-proton elastic scattering since the recoil particles are exactly the same for both antiproton-proton elastic scattering at HESR and proton-proton elastic scattering at COSY. Fig. 53 shows the calculated partial and total different cross section of proton-proton elastic scattering at 3.2 GeV/c with typical parameterization using two different ρ -values. The commissioning experiment has been performed at the ANKE hydrogen cluster target station at COSY. Data of the proton-proton elastic scattering at beam momenta of 2.5, 2.8 and 3.2 GeV/c have been taken in commissioning weeks. The t -distribution has been reconstructed and the parameters

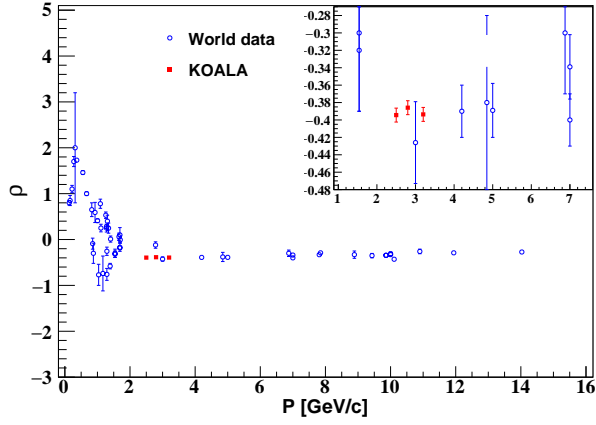


Fig. 55: The determined parameter ρ at 3 beam momenta is well consistent with existing data of proton-proton elastic scattering.

of σ_{tot} , ρ and B have been determined with small errors. As shown in Fig. 55 the determined parameter ρ is well consistent with existing data of proton-proton elastic scattering. The preliminary results of the commissioning experiment is very encouraging to achieve the goals of measuring antiproton-proton elastic scattering with high precision.

5 Neutrino Physics

The IKP-2 Neutrino Group was established by the recruitment of Livia Ludhova as the head of the group in November 2015. Thanks to her success in the recruitment initiative of Helmholtz Association, the group has significantly increased in size: now it comprises one Post-Doc and five PhD students. More details about the group can be found on the web site: <http://collaborations.fz-juelich.de/ikp/neutrino/>

The three sections below, Borexino, SOX, and JUNO, describe the three main neutrino physics projects, in which the group is involved. The focus is made on the work and achievements since the last Annual Report 2015.

5.1 Borexino latest results and perspectives

Borexino is a 300 ton liquid scintillator detector placed in the Laboratori Nazionali del Gran Sasso in central Italy, the largest underground laboratory in the world. The unprecedented radiopurity of the scintillator was at the base of a series of spectroscopic measurements of neutrino species from the pp-cycle (pp, pep, ^7Be , and ^8B neutrinos), a unique success of Borexino. Geoneutrinos, antineutrinos emitted along the decays of long-lived radioactive elements inside the Earth, are unique probes to determine the radiogenic heat produced in the deep Earth. Borexino, together with KamLAND in Japan, are the only two experiments being currently able to measure geoneutrinos. Thanks to an unprecedentedly high radiopurity and relatively large volume, Borexino has placed stringent limits on several rare processes. The IKP-2 became an official member of the Borexino/SOX collaboration, with L. Ludhova being a member of the Borexino Institutional Board.

During spring 2016, a new trigger of the Borexino data acquisition system has been installed. L. Ludhova, as the data quality manager, has coordinated an effort to guarantee the high-quality of the data taken with the new system, being compatible with the old one.

A new publication "A test of electric charge conservation with Borexino" was issued in December 2015. The analysis is very similar to the one, which lead to the pp-neutrino result published in Nature in 2014. Thanks to the unmatched radiopurity of the scintillator, and to the well understood detector response at low energy, a new limit on the stability of the electron for decay into a neutrino and a single 256 keV photon was obtained. The new bound, $\tau \geq 6.6 \times 10^{28}$ yr at 90 % C.L., is demonstrated in the energy spectrum shown in Fig. 56.

L. Ludhova has coordinated an effort leading to the publication "Borexino's search for low-energy neutrino and antineutrino signals correlated with gamma-ray bursts" (GRBs). No statistically significant excess over background was observed. Electron antineutrinos ($\bar{\nu}_e$) that inverse beta decay on protons were searched for up to 15 MeV and the best limit on the neutrino fluence from GRBs below 8 MeV was set, see Fig. 57. The signals

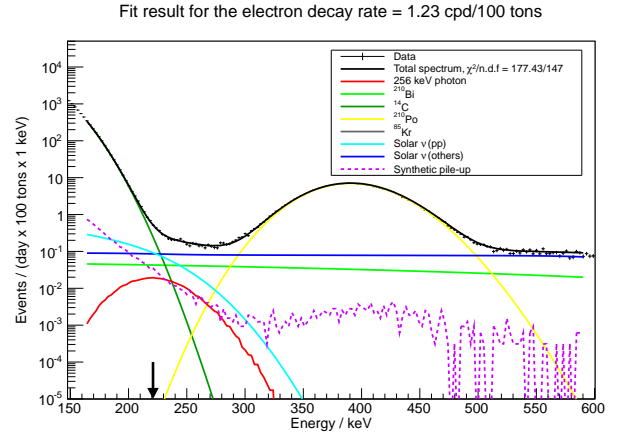


Fig. 56: Borexino energy spectrum between 150 and 600 keV. The hypothetical mono-energetic 256 keV γ line is shown in red at its 90% exclusion C.L. with an arrow indicating the mean value of the detected energy.

from neutrinos and antineutrinos from GRBs that scatter on electrons were also searched for, a detection channel made possible by the particularly radiopure scintillator of Borexino. Currently the best limits on the neutrino fluence of all flavors and species below 7 MeV were obtained, see Fig. 58. Finally, time correlations between GRBs and bursts of events were investigated. This analysis combined two semi-independent data acquisition systems for the first time: the primary Borexino readout optimized for solar neutrino physics up to a few MeV, and a fast waveform digitizer system tuned for events above 1 MeV.

The data gathered starting from 2011 (Phase II), is characterised by even lower background than Phase I (2007-2010). These data are currently the main focus of the solar neutrino program, in which the IKP group is deeply involved. In contrast with the previous analysis, the spectral fit is being performed on the whole energy scale up to about 1.5-2 MeV, providing a simultaneous result for ^7Be , pp, and pep neutrinos.

The new release of the solar neutrino results of Borexino, including update on the ^7Be , pp, pep, and CNO limit, is planned by the middle of 2017. All members of the Borexino part of the IKP group are involved and L. Ludhova was appointed by the collaboration as one of the 4 authors responsible for writing the new paper.

Thermal isolation of the Borexino detector has been recently installed. This might make possible to determine the constant term of the ^{210}Po contamination, in equilibrium with the ^{210}Bi one. The ^{210}Bi decay spectrum is almost fully degenerated with the energy spectrum of CNO neutrinos. The possibility of the first measurement of these neutrinos, expected to contribute to the solar power by less than 1%, is currently under investigation.

Insertion of the SOX antineutrino generator below the Borexino detector in spring 2018 will naturally end the geoneutrino data set. The final geoneutrino release with

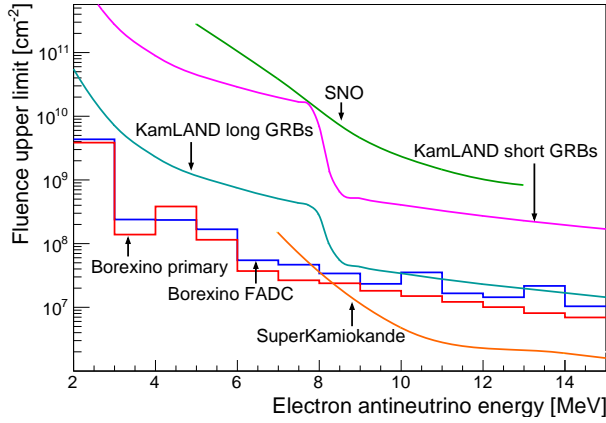


Fig. 57: Fluence upper limits for electron antineutrinos from GRBs versus antineutrino energy. Borexino results are shown in comparison with results from SuperKamiokande (Fukuda et al. 2002), Sudbury Neutrino Observatory (SNO) (Aharmim et al. 2014), and KamLAND (Asakura et al. 2015).

updated selection cuts and possibly no fiducial volume cut is foreseen with up to a double exposure with respect to the last release in 2015. Since L. Ludhova has a double education, master and PhD both in geology and physics, as well as an experience with coordination of the geoneutrino analysis, the group has already started to work on this improved analysis with the currently available data.

5.2 Short distance neutrino oscillations with Borexino

The measurement of decays of Z^0 boson at LEP has confirmed that there are 3 families of light neutrinos interacting through weak interactions. In recent years, however, several experimental results indicate that the 3-flavor picture might not be complete: deficit observed in reactor antineutrino short-baseline experiments, the so called reactor anomaly, the deficit observed in calibration of Gallex and SAGE experiments with neutrino sources, the famous appearance of $\bar{\nu}_e$ in $\bar{\nu}_\mu$ beam seen by LSND and further tested by MiniBooNe. All these anomalies could be at least partially accommodated if at least one sterile neutrino exists. It is called sterile because it would not interact through the forces described by the Standard Model. A global analysis of short-baseline neutrino oscillation data in 3+1 parameter space leads to Δm_{41}^2 around 1 eV². In order to probe this region with MeV (anti)neutrinos, the oscillation experiments at distances of few meters have to be performed. In such an experiment, the hypothetical existence of sterile neutrino could be observed not only through an absolute disappearance but also through the oscillation pattern in (L, E) parameter space deviating from the standard 3-flavor scenario. That latter would provide a "smoking gun" signature of

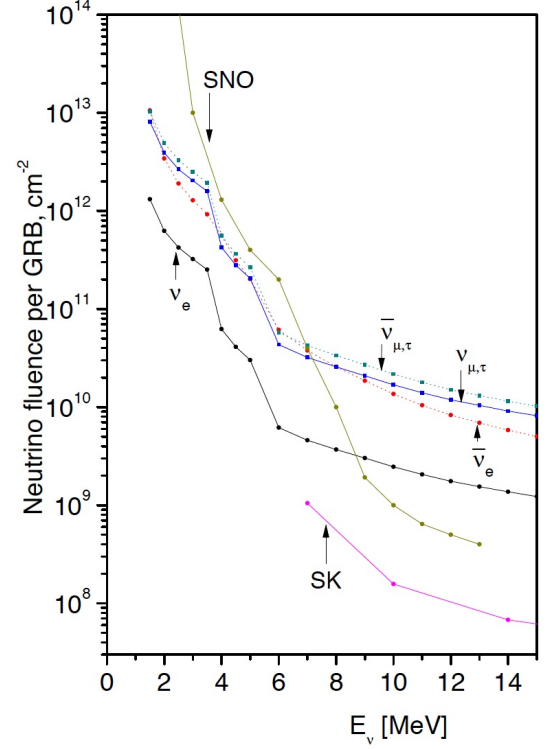


Fig. 58: Borexino 90% C.L. fluence upper limits obtained through neutrino-electron elastic scattering for ν_e , $\bar{\nu}_e$, $\nu_{\mu,\tau}$, and $\bar{\nu}_{\mu,\tau}$. Given are also the limits obtained for ν_e by SNO (Aharmim et al. 2014) and SuperKamiokande (SK, Fukuda 2002).

the sterile neutrino, a clear indication for physics beyond the standard model.

The very low radioactive background of the Borexino detector, its large size, and the well proved capability to detect both low energy electron neutrinos and antineutrinos make an ideal case for the study of short distance neutrino oscillations with artificial sources at Laboratori Nazionali del Gran Sasso in Italy. The SOX project, short-distance neutrino Oscillations with BoreXino, aims at the complete confirmation or at a clear disproof of the existence of such a light sterile neutrino. A 4 to 5 PBq (>100 kCi) ^{144}Ce - ^{144}Pr antineutrino source, producing about 10^{15} $\bar{\nu}_e$ /s, will be placed below the Borexino detector at a distance of 8.3 m from the detector's centre. The Mayak Production Association, one of the biggest nuclear facilities in the Russian Federation, will produce the source based on the contract, which was successfully signed after a long period of negotiations at the end of 2016. The data taking will continue for about 1.5 years. The expected SOX sensitivity to sterile neutrino is shown in Fig. 59.

The isotope of ^{144}Ce decays with the lifetime of 285 days to ^{144}Pr , which then with much shorter lifetime decays to ^{144}Nd . SOX will measure antineutrinos above the IBD threshold, emitted by ^{144}Pr with the end-point at about 3 MeV. The 2.2 MeV gammas from the de-excitation of

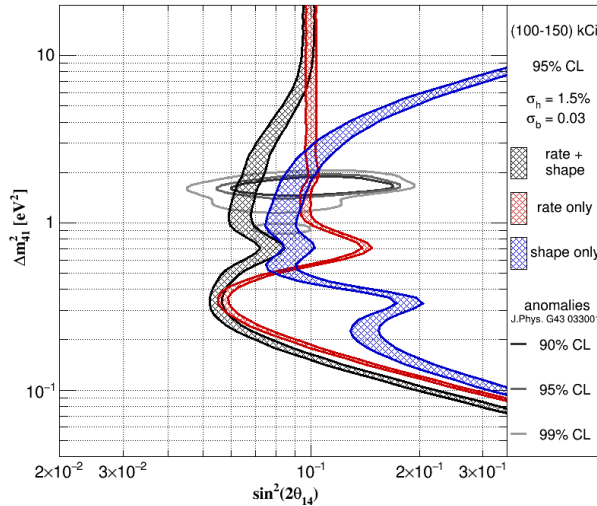


Fig. 59: The expected SOX sensitivity to test the hypothesis of sterile neutrino.

^{144}Nd will be efficiently shielded by a thick tungsten case. Two independent calorimeters are developed in order to measure the released heat with $\sim 1\%$ precision. In order to convert the measured heat to the activity with sufficient precision, a new more precise measurement of the $^{144}\text{Pr}(\beta)$ spectrum is needed. The group will participate in the finalisation of such a measurement, which is on-going at Saclay in France.

L. Ludhova and M. Wurm from Mainz University are coordinators of the SOX analysis group. All members of the Borexino/SOX part of the IKP group are involved in the analysis. Currently, the focus is on the optimisation of the IBD selection criteria, background estimations and sensitivity studies. A significant effort will be devoted to the estimation of different systematic effects on the final sensitivity.

The SOX analysis aims to consider the whole scintillator volume without any fiducial volume cut, unlike any previous Borexino analysis. In order to do so, a new calibration campaign with AmBe neutron source, as well as several other radioactive sources, is planned in a near future. The IKP-2 Neutrino Group will contribute to this effort which will last 2 to 3 months.

5.3 Towards neutrino mass hierarchy: JUNO

The first multi-kton liquid scintillator detector ever constructed will be placed at Jiangmen Underground Neutrino Observatory (JUNO). This 20 kton detector is under construction in Jiangmen, China. The collaboration comprises about 450 members from 66 institutions mostly from China and Europe. The main aim of this project is to determine the neutrino mass hierarchy by measuring reactor neutrinos with 53 km baseline. The expected sensitivity is at the level of 3 to 4 σ in 6 years of measurement with the total power of 36 GW of all nuclear cores in Yangjiang and Taishan, partially existing, and partially

under construction or planned. The construction work of the underground lab placed 720 m below the surface is on-going. The IKP-2 became an official member of the JUNO collaboration, with L. Ludhova being a member of the JUNO Institutional Board.

The energy spectra corresponding to the normal and inverted mass hierarchies differ. There is a small difference in the position of the relative peaks and maxima related to the "fast oscillation" in the electron antineutrino survival probability. In order to be able to distinguish between the two respective patterns, several challenges have to be overcome. An excellent energy resolution, so far never obtained with a large scintillator detector, of 3% at 1 MeV has to be reached. This corresponds to a large light yield of about 1200 photoelectrons/MeV. For comparison, the highest existing light yield is 500 photoelectrons/1 MeV, reached by Borexino. Special PMTs with high quantum efficiency have to be developed. High light yield LAB-based scintillator of excellent transparency is under development. The purification procedure is going to be tested by measuring the purified 20 tons "sample" employed in one of the Daya Bay detectors. The detector's PMT geometrical coverage will reach 80% by mounting 18000 large 20-inch PMTs and 36000 small 3-inch PMTs. A new ADC chip called VULCAN for PMT read-out is developed at ZEA-2 institute at FZJ.

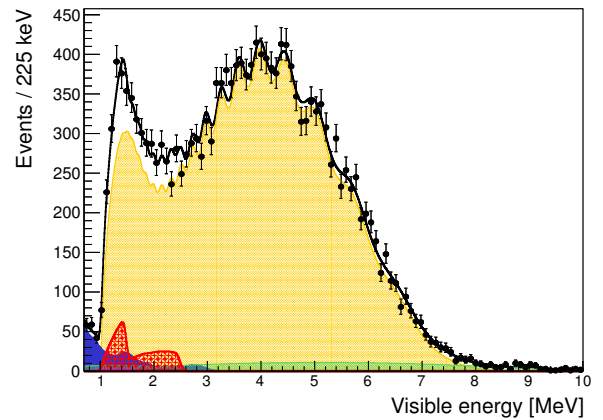


Fig. 60: Toy Monte Carlo for 1-year JUNO measurement.

The different spectral components are shown as they result from the fit; black line shows the total sum for the best fit. The geoneutrino signal is shown in red. The following colour code applies to the backgrounds: orange (reactor antineutrinos), green ($^9\text{Li} - ^8\text{He}$), blue (accidental), small magenta (α, n).

IKP-2 group concentrates on analysis and simulations. Coordination among European groups in this area was triggered by the meeting organized by the group at IKP in April 2016. In total, there have been 28 participants, including 3 tutors from China. The idea of such meetings was very successful and another meeting followed in November 2016, organized at LLR, France. These meet-

ings have also triggered the creation of a working group, responsible for the Monte Carlo production and validation, in which PhD students from IKP play a key role.

The group has gained one of the best European expertise in the JUNO software framework, which is mostly developed in China. Strong effort is put into muon-tracking and wave-form reconstruction algorithms. Shortly, this effort will be extended to clustering algorithm, electronics simulations, and the study of different systematic effects on the JUNO sensitivity to mass hierarchy measurement. JUNO PhD students have spent 2 weeks in July at IHEP in Beijing, in order to become even more familiar with the existing software through a close collaboration with Chinese colleagues. This process will become even more effective, when new colleagues from China will join the group: a PhD student in January and a PostDoc in spring 2017 (Jülich - OCPC - Programme).

The group has also an expertise in the evaluation of the JUNO sensitivity to geoneutrinos (see Fig. 60) and solar neutrinos.

6 COSY - Highlights from Hadron Physics

The experimental hadron physics program at COSY terminated at the end of 2014. In order to summarize the results obtained at COSY during this era, which started more than 20 years ago, the Directors of the Institut für Kernphysik have asked Colin Wilkin (UCL, London, UK), a long-term collaborator with deep insight into the science, to collect and write down "The legacy of the experimental hadron physics program at COSY". After a year of hard work his résumé has recently been put to the e-print archive [arXiv:1611.07250] and has been submitted for publication in European Physical Journal A.

6.1 Precision studies on angular asymmetries of the $d + p \rightarrow {}^3\text{He} + \eta$ reaction

The total and differential cross sections of the reaction $d + p \rightarrow {}^3\text{He} + \eta$ are of special interest since they differ strongly from a pure phase space behaviour. Assuming there is no final state interaction (FSI) between the ${}^3\text{He}$ nucleus and the η meson one would expect that close to the threshold the total cross section will in good approximation increase proportional to \sqrt{Q} with Q being the excess energy. Nevertheless, previous measurements at ANKE showed a rapid rise of the total cross section within the first 1 MeV in Q , which can be explained by a pole near threshold and suggests a possible quasi bound state of the ${}^3\text{He}\eta$ -system. If this pole near threshold is responsible for the unusual non pure phase space behaviour of the total cross section, one should also notice a change in the phase of the s-wave amplitude. In order to further investigate this, the extraction of precise differential cross sections is mandatory. Due to the fact that the cross section is proportional to the absolute square of the scattering amplitude $|f_s|^2$, the phase information is lost. However, the information of the relative phase variation of the s-wave can be gained by the interference with possible higher partial waves, like p-waves. At ANKE precision data on this topic are currently evaluated since the available data sets are afflicted by large overall uncertainties. The data have been taken close to the threshold at 18 deuteron beam momenta p_{beam} between 3120.17 MeV/c and 3204.16 MeV/c using the supercycle mode. Each of the 18 beam momenta were determined accurately with a precision of $\Delta p_{\text{beam}}/p_{\text{beam}} < 6 \times 10^{-5}$ using the spin resonant depolarization technique.

The identification of the reaction is ensured by using the energy loss information of the ${}^3\text{He}$ nuclei in the scintillator hodoscopes of the forward detection system. Due to the full angular coverage of the reaction in combination with the high statistics of more than 10^5 ${}^3\text{He}\eta$ events per energy, the measurement allows a precise study of the angular distribution as shown in Fig. 61.

Up to a final state momentum of $p_f^{\text{CMS}} \approx 100$ MeV/c the differential cross sections are linear in $\cos(\vartheta_\eta^{\text{CMS}})$. Considering the anisotropy of the differential cross sections,

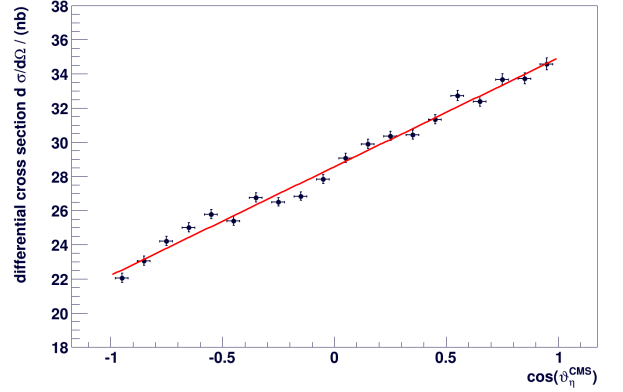


Fig. 61: Preliminary differential cross section of the η production channel $d + p \rightarrow {}^3\text{He} + \eta$ at a final state momentum of $p_f^{\text{CMS}} = 76.92$ MeV/c ($Q = 6.33$ MeV). The uncertainties in $\frac{d\sigma}{d\Omega}$ represent the statistical uncertainties only and the solid line is a linear fit to the data points.

with the η preferably scattered in forward direction, the introduction of an asymmetry parameter α is reasonable:

$$\alpha = \frac{d}{d \cos(\vartheta_\eta^{\text{CMS}})} \ln \left(\frac{d\sigma}{d\Omega} \right) \Big|_{\cos(\vartheta_\eta^{\text{CMS}})=0}. \quad (3)$$

The solid red line in Fig. 61 represents a linear fit to the data of the form

$$\frac{d\sigma}{d\Omega} = A \cdot (1 + B \cdot \cos(\vartheta_\eta^{\text{CMS}})) \quad , \quad (4)$$

so that the fit parameter B is tantamount to the asymmetry parameter α . Additionally, this parametrization has the advantage that the result of the fit parameter B is independent of the absolute normalization. This has been done for each of the 15 calibrated beam momenta, which are above the η production threshold. The corresponding preliminary results for the asymmetry parameter α are shown in Fig. 62.

In general, at low final state momenta $p_f^{\text{CMS}} \leq 50$ MeV/c, the angular asymmetry seems to be constant, whereas with rising p_f^{CMS} also the angular asymmetry increases. The observed behaviour at higher p_f^{CMS} was also seen by previous measurements at ANKE and COSY-11 and can be explained by a phase variation of the s- and p-wave interference. Furthermore, it is conspicuous that all preliminary α values are positive, which seems to show a different trend as the ANKE, COSY-11 and SPESII results with their slightly negative values near threshold. It is generally interpreted that this effect can only occur, if the interference of the s- and p-wave production amplitude changes significantly, while strictly positive α values do not lead to such a rapid phase variation.

Moreover, the result of the data at $p_f^{\text{CMS}} = 117.84$ MeV/c ($Q = 15$ MeV) shows a non linear behaviour of the differential cross sections. Accordingly, higher partial waves,

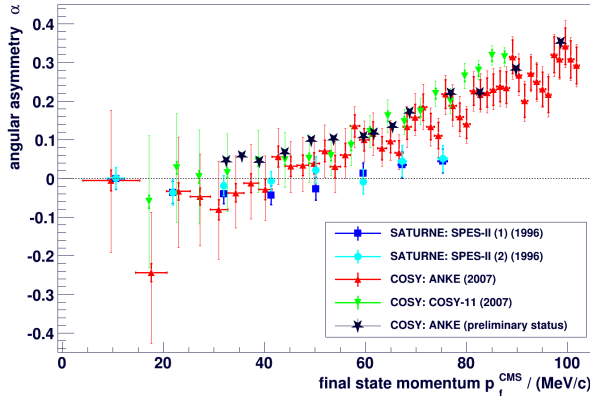


Fig. 62: Preliminary values of the asymmetry parameter α (black stars) with rising final state momentum of the η meson in the center of mass system. Due to the preliminary status, the uncertainties of the data points are not shown.

like d-waves, have to be taken into account and can be introduced by a $\cos(\vartheta_{\eta}^{CMS})^3$ term in the description of the angular distribution. This observed behaviour at $p_f^{CMS} \geq 110$ MeV/c is also consistent with new preliminary data of the WASA-at-COSY experiment.

6.2 Model-independent measurement of the spin triplet $p\Lambda$ scattering length

The Λ hyperon production in the $\bar{p}p \rightarrow pK^+\Lambda$ reaction was measured with a polarized proton beam which allows the extraction of the spin-triplet $p\Lambda$ scattering length. This requires the measurement of the symmetric contribution of the beam analyzing power determined from the asymmetry of the produced kaon. Compared to existing analyses of spin resolved scattering length studies by combined fit procedures of spin-singlet and spin-triplet contributions this study is the first direct model-independent determination of the $p\Lambda$ spin triplet scattering length.

The measurement was performed with the COSY-TOF detector at a beam momentum of 2.7 GeV/c with a mean polarization of $77.9 \pm 1.2\%$. The detector covers the full phase space of the reaction as can be seen in the Dalitz plot in Fig. 63. The reconstruction efficiency is nearly constant over the full kinematic range and amounts to about 15%, and the achieved mean $p\Lambda$ invariant mass resolution is 1.3 MeV. The scattering length a is determined from the shape of the $p\Lambda$ invariant mass spectrum ($m_{p\Lambda}$). If polarization observables are not considered the determined value is an effective scattering length a_{eff} . Fig. 64 shows a fit to the data by a scattering length parametrization deduced from a dispersion theory analysis (Phys. Rev. C 69 (2004) 034006). The fit range is limited to an excess energy range of 40 MeV to ensure the dominance of an S-wave $p\Lambda$ system. The resulting a_{eff} of $(-1.38 \pm_{0.05}^{0.04} \text{ stat.} \pm 0.022_{\text{sys.}} \pm 0.3_{\text{theo.}}) \text{ fm}$ is consistent

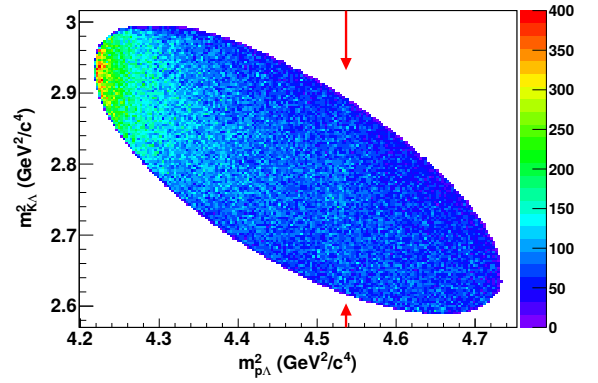


Fig. 63: Dalitz plot of the $pK^+\Lambda$ events at 2.7 GeV/c beam momentum corrected for acceptance and reconstruction efficiency. The red arrows indicate the region of the N^* thresholds. Contributions from these channels are negligible at this beam momentum.

with previous analysis. In order to check the influence of N^* resonances in the $K\Lambda$ cross channel which may introduce a systematic error for the analysis, the Dalitz plot was separated in four slices of the $p\Lambda$ helicity angle which were analyzed separately. Each slice occupies the full $m_{p\Lambda}$ range and the invariant mass spectra would be identical without N^* contributions. The obtained error is 0.1 fm which agrees with a negligible influence of N^* resonances. For the determination of the spin-triplet

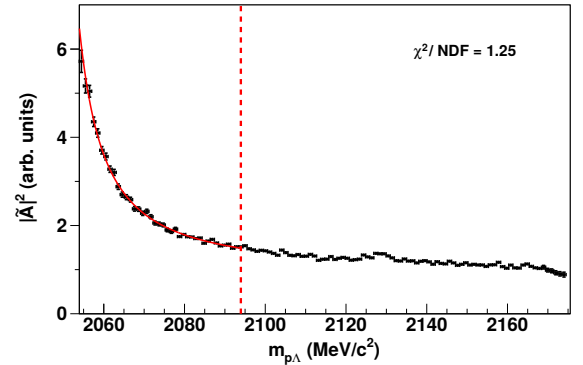


Fig. 64: The amplitude squared $|\tilde{A}(m_{p\Lambda})|^2$ corresponding to the $p\Lambda$ invariant mass distribution divided by the volume of available phase space with a fit to the data by the scattering length parametrization (solid red line) in the marked fit range (up to dashed red line).

scattering length a_t the $|\tilde{A}(m_{p\Lambda})|^2$ has to be combined with the symmetric coefficients of the associated Legendre Polynomial P_l^m , the only contribution to the spin-triplet $p\Lambda$ final state. It turns out that the two leading terms P_1^1 and P_2^1 are sufficient to describe the data shown in Fig. 65. Therefore the contribution of P_1^1 , $\alpha(m_{p\Lambda})$, is used for the determination of the spin-triplet scattering

length. In Fig. 66 the $|\tilde{A}(m_{p\Lambda})|^2$ distribution combined

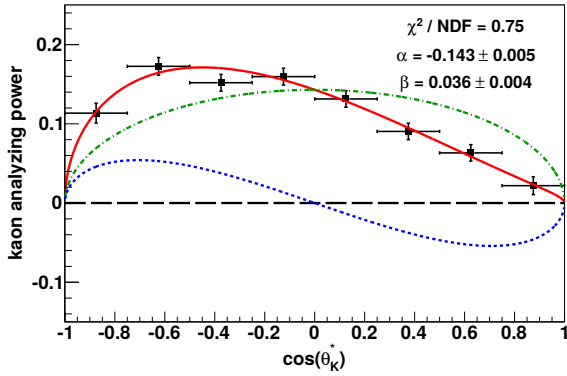


Fig. 65: The beam analyzing power determined by the kaon asymmetry, A_N^K , as a function of $\cos\Theta_K^*$. The solid red line shows the fit with $\alpha \cdot P_1^1 + \beta \cdot P_2^1$. The individual contributions of the associated Legendre polynomials P_1^1 and P_2^1 are shown by the dash-dotted green and dotted blue lines, respectively.

with $\alpha(m_{p\Lambda})$ is shown with the fit by the scattering length parametrization from which a spin-triplet scattering length of $a_t = (-2.55 \pm_{1.39}^{0.72} \text{ stat.} \pm 0.6_{\text{sys.}} \pm 0.3_{\text{theo.}}) \text{ fm}$ results. The work is accepted for publication in Phys.Rev. C in which details of the analysis and the contributing errors are described.

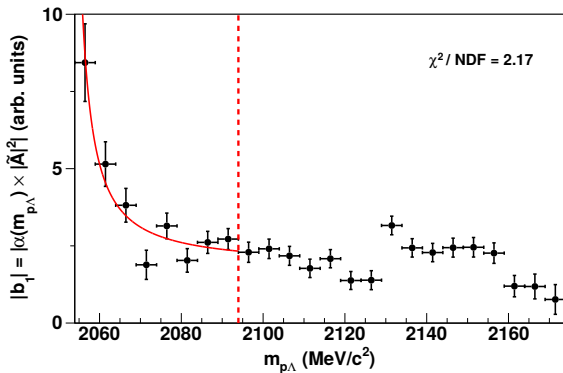


Fig. 66: Distribution of $\alpha(m_{p\Lambda}) \times |\tilde{A}(m_{p\Lambda})|^2$ fitted by the scattering length parametrization (red solid line) limited to 40 MeV excess energy (dashed red line).

6.3 Search for an isospin $I = 3$ dibaryon

Theoretical calculations, which now successfully obtain the $d^*(2380)$ state, predict partly also a dibaryon state D_{30} with mirrored quantum numbers $I(J^P) = 3(0^+)$ at a similar mass. In tendency, this state, which is expected to be again asymptotically a $\Delta\Delta$ configuration, appears to be somewhat less bound than $d^*(2380)$, but still below the

$\Delta\Delta$ threshold of $2m_\Delta$. The predicted width varies from about 90 MeV to about 180 MeV.

In order to investigate this topic experimentally, we consider the four-pion production in proton-proton collisions, in particular the $pp \rightarrow pp\pi^+\pi^+\pi^-\pi^-$ reaction. Because of its isospin $I = 3$ such a state is isospin-decoupled from the nucleon-nucleon (NN) system. Therefore, in order to be able to reach such a state by NN collisions, its production in the collision process needs to be associated by the generation of particles, which take away two units of isospin – preferably by two extra pions. So the wanted process is $pp \rightarrow D_{30}\pi^-\pi^- \rightarrow \Delta^{++}\Delta^{++}\pi^-\pi^- \rightarrow pp\pi^+\pi^+\pi^-\pi^-$. Due to $I = 3$ the $\Delta^{++}\Delta^{++}$ configuration is the most preferred $\Delta\Delta$ combination, into which D_{30} decays.

The measurements of this reaction have been carried out with the WASA detector including a hydrogen pellet target at the cooler synchrotron COSY using proton beams with kinetic energies of $T_p = 2.063$ and 2.541 GeV. The mass range of this search, which has been the first one of its kind for an $I = 3$ dibaryon, covered the region from 2.2 - 2.5 GeV, i.e. from near-to two-pion threshold up to the nominal $\Delta\Delta$ threshold of $2m_\Delta$ and above.

The resulting data exhibit no clear-cut evidence for such a resonance (see Phys. Lett. B **762** (2016) 445). The deduced upper limits for the production of such a resonance are three to four orders of magnitude smaller than the formation cross section found for $d^*(2380)$. They also are up to one order of magnitude smaller than the cross section for conventional $\Delta^{++}\Delta^{++}$ production in the $pp \rightarrow pp\pi^+\pi^+\pi^-\pi^-$ reaction – again in sharp contrast to the corresponding situation for $d^*(2380)$ formation, where this is an order of magnitude larger than in conventional $\Delta\Delta$ formation.

With only upper limits at present we cannot exclude the existence of such a resonance. However, if existent, either the production process of the $I = 3$ resonance associated with the emission of two pions has an unusually small cross section or such a resonance has a mass above the energy region investigated here. However, in such a case its width is expected to be very broad due to its fall-part decay and hence will be very hard to be distinguished from conventional processes.

6.4 Coherent meson production in the reaction $pd \rightarrow pdX$

A coherent meson production in pd interaction can be provided by a t -channel excitation of a deuteron to a two-baryon state of a nucleon and a baryon resonance. A subsequent decay of this state to the deuteron is accompanied by meson production. Such a process, not studied before, was investigated at ANKE via detection of high-momentum pairs of a proton and a deuteron at small forward angles relative to the proton beam.

The measurement of the 4-momenta of the proton and the deuteron allows the determination of the invariant mass of the missed meson system X . Spectra of this mass

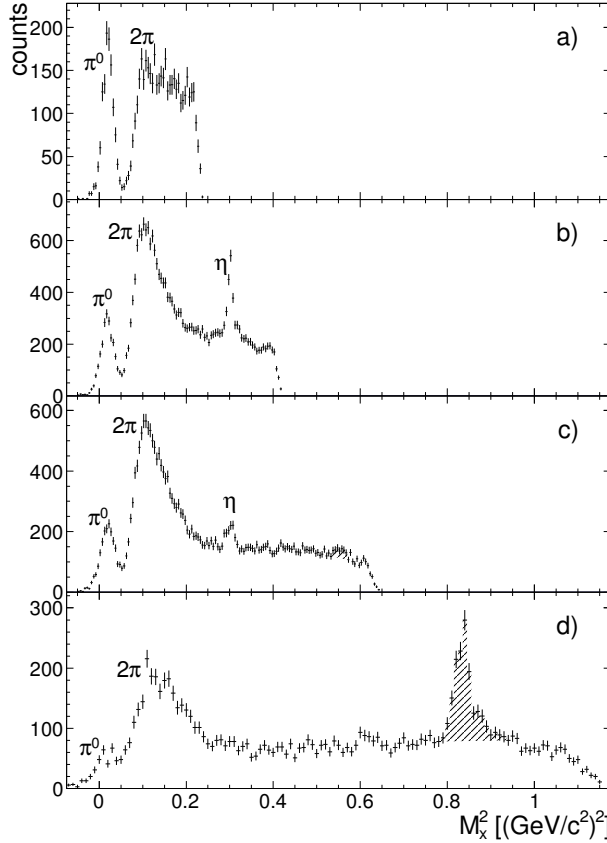


Fig. 67: Spectra of the missing mass squared, M_X^2 , at 0.8 GeV (a), 1.1 GeV (b), 1.4 GeV (c) and 1.97 GeV (d) proton beam energies. The shaded peaks at 0.55 GeV/c² (c) and 0.84 GeV/c² (d) are caused by the pd background.

squared, M_X^2 , (Fig. 67) reveal a peak caused by a single pion production, a clear enhancement near the threshold of a two-pion production, a peak caused by a single η -meson emission and a continuum of the multi-meson production. A separation of certain parts of the M_X spectra allows to obtain the final deuteron-meson system invariant mass.

The $d\pi$ mass spectrum has a defined peak with a mean value of 2.20 ± 0.05 GeV/c² and 110 ± 10 MeV/c² width. The peak is obviously caused by the well-known $N\Delta(1232)$ resonance.

The $d\pi\pi$ spectrum reveals a peak with a mean value of 2.38 ± 0.08 GeV/c² and 100 ± 15 MeV/c² width. The peak is located in the $\Delta(1232)\Delta(1232)$ excitation region and might be of the same nature as the WASA isoscalar resonance with 2.37 GeV/c² mass. The resonance in the $\Delta\Delta$ excitation region has been described in the meson-baryon approach by Gal and Garcilazo in 2013.

The $d\eta$ spectrum exhibits a peak with a mean value of 2.45 ± 0.05 GeV/c² and a width of about 40 MeV/c². This peak position is close to the sum of the nucleon and $N(1535)$ resonance masses, 2.47 GeV/c², what indicates its $NN(1535)$ resonance origin. Analysis of the data on

the latter resonance, never observed before, is in progress at present.

The obtained data demonstrate that the lightest nucleus, the deuteron, in scattering conditions of small transverse- and significant longitudinal-momentum transfers displays excitations of a two-baryon system with a definite spectrum of quasi-bound and continuum states.

6.5 Isoscalar single-pion production in the region of Roper and $d^*(2380)$ resonances

Exclusive and kinematically complete measurements of the quasi-free $pn \rightarrow pp\pi^-$ and $pp \rightarrow pp\pi^0$ reactions have been carried out by means of pd collisions at $T_p = 1.2$ GeV using the WASA detector setup at COSY. Therefrom total and differential cross sections have been obtained covering the energy region $T_p = 0.95 - 1.3$ GeV ($\sqrt{s} = 2.3 - 2.46$ GeV), which are also the regions of $\Delta(1232)$, $N^*(1440)$ and $d^*(2380)$ resonance excitations.

From these measurements the isoscalar part of the single-pion production cross section has been extracted, for which data existed so far only below $T_p = 1$ GeV – see Fig. 68. We observe a substantial increase of this cross section above 1 GeV, which can be related to the Roper resonance $N^*(1440)$ excitation. It shows up isolated from the Δ resonance in the $N\pi$ invariant-mass spectrum of the isoscalar cross section.

In this energy region also the hypothetical decay of the $d^*(2380)$ dibaryon resonance into the $NN\pi$ system is expected. Recently, exclusive and kinematically complete WASA measurements of the double pionic fusion reaction $pn \rightarrow d\pi^0\pi^0$ revealed a narrow resonance structure in the total cross section at a mass $m \approx 2380$ MeV having a width of $\Gamma \approx 70$ MeV and quantum numbers $I(J^P) = 0(3^+)$. Additional evidence for it had been traced subsequently in all two-pion production channels, which contain isoscalar components. Finally, analyzing power measurements of np elastic scattering at WASA established this structure to be a genuine s -channel resonance with a pole in the 3D_3 partial wave — denoted since then by $d^*(2380)$.

Such a dibaryon resonance, which asymptotically resembles a deeply bound $\Delta\Delta$ system, was predicted first by Dyson and Xuong in 1964 based on $SU(6)$ symmetry breaking. Indeed, there are now quite a number of QCD-based model calculations, which find $d^*(2380)$ at about the correct mass. Also, relativistic Faddeev-type calculations based on hadronic interactions find this state at the correct mass. However, the latter calculations assume the asymptotic hadronic configuration not to be a $\Delta\Delta$, but a $D_{12}\pi$ configuration, where D_{12} denotes the dibaryonic state at the ΔN threshold with $I(J^P) = 1(2^+)$. However, different from the $\Delta\Delta$ scenario there should be now a 17% decay branch $d^*(2380) \rightarrow D_{12}\pi \rightarrow [NN\pi]_{I=0}$.

As apparent from Fig. 68 no evidence for a decay of the dibaryon resonance $d^*(2380)$ into the isoscalar $(NN\pi)_{I=0}$ channel is found in the new WASA data.

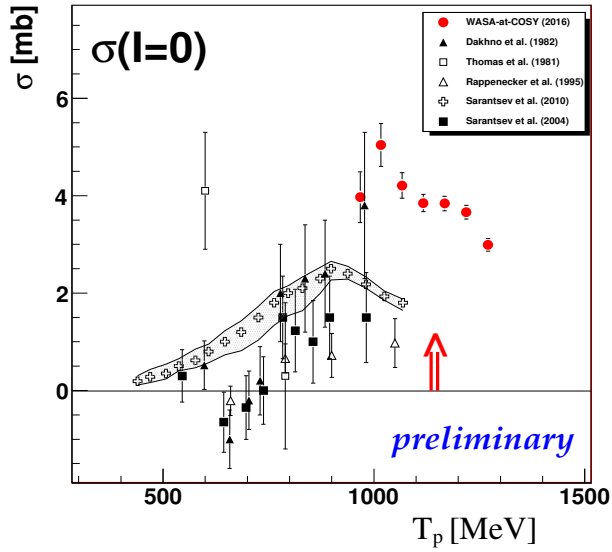


Fig. 68: Isoscalar part of the single-pion production cross section in NN collisions. The solid (red) circles denote the WASA measurements, other symbols show previous measurements. The arrow indicates the position of the hypothetical $d^*(2380) \rightarrow NN\pi$ transition.

Hence only an upper limit can be deduced. A corresponding publication is in preparation.

6.6 Measurement of the $\omega \rightarrow \pi^+\pi^-\pi^0$ Dalitz plot distribution

The main decay mode of the ω -meson resonance discovered in 1961 is $\omega \rightarrow \pi^+\pi^-\pi^0$, with a branching ratio of $BR = (89.2 \pm 0.7)\%$. The spin-parity of ω ($J^P = 1^-$) and the combination of Bose, isospin, and parity symmetry of the strong interaction demands that for the decay $\omega \rightarrow \pi^+\pi^-\pi^0$ every pion pair is in a state of odd relative orbital angular momentum. Given the limited phase space of the decay, P -wave is the dominant partial wave. This further implies the third pion in P -wave state relative to the pair. This “ P -wave phase space” distribution has been well established experimentally and historically has been used to determine ω quantum numbers. However, a pion pair in a P -wave shows a very strong final-state interaction. The two-pion P -wave phase shift is dominated by the ρ meson, and is now known very accurately. The prediction of the presence of final-state interactions leading to an increase of strength towards the Dalitz-plot boundaries has not been observed experimentally so far. The highest statistics of a dedicated $\omega \rightarrow \pi^+\pi^-\pi^0$ Dalitz plot measurement from 1966 had 4208 ± 75 signal events and fits with a pure P -wave phase space which could not be distinguished from a distortion by the final-state interactions, *i.e.* by intermediate $\rho\pi$ states. Surprisingly

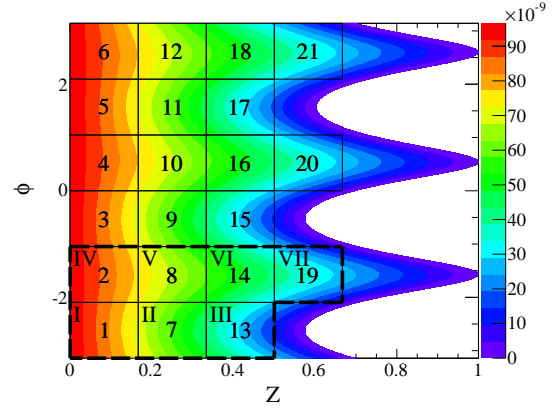


Fig. 69: Arabic numbering of the bins used in the analysis. The color plot shows the kinematically allowed region of the $\omega \rightarrow \pi^+\pi^-\pi^0$ decay with ω nominal mass as well as the density distribution from P -wave dynamics.

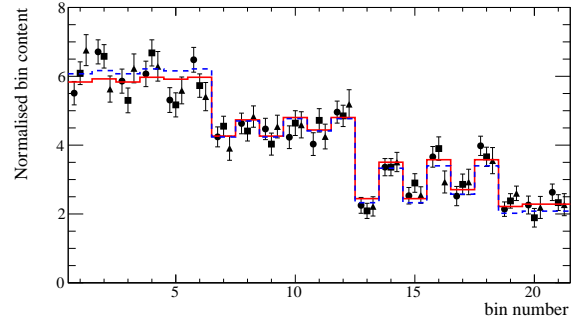


Fig. 70: Efficiency corrected experimental Dalitz plot distribution. Circles correspond to set A, squares to set B, and triangles to set C. The solid red line is the fit result with α parameter, and the dashed line is P -wave only.

there were no further dedicated Dalitz plot studies of the $\omega \rightarrow \pi^+\pi^-\pi^0$ decay.

The WASA-at-COSY collaboration has collected three data sets for ω meson decay studies. Two sets were obtained using the $pd \rightarrow {}^3\text{He}\omega$ reaction at two different proton kinetic energies $T_A = 1.450\text{ GeV}$ and $T_B = 1.500\text{ GeV}$. The third set comes from $pp \rightarrow pp\omega$ experiment at $T_C = 2.063\text{ GeV}$ beam kinetic energy, corresponding to 60 MeV centre-of-mass excess energy. The combined data sample includes $(4.408 \pm 0.042) \times 10^4$ events.

In addition to ${}^3\text{He}$ or two protons the selected events have to contain at least a pair of opposite charge particle tracks and at least two neutral clusters in the calorimeter. The charged particle tracks are assigned the charged pion mass. A constrained kinematic fit imposes the energy and momentum conservation with the $pd \rightarrow {}^3\text{He}\pi^+\pi^-\gamma\gamma$ or $pp \rightarrow pp\pi^+\pi^-\gamma\gamma$ hypothesis, respectively. The events with a probability of less than 0.05 are rejected. The missing mass distributions, $MM({}^3\text{He})$ and $MM(pp)$, is

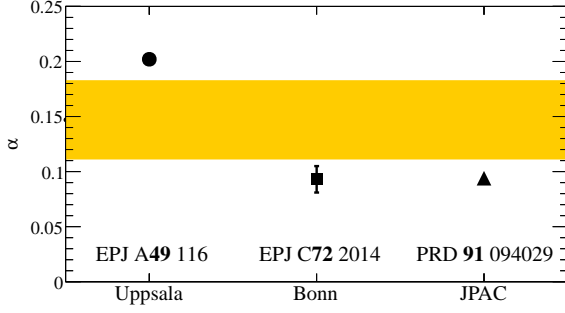


Fig. 71: Comparison of our result for the α parameter (yellow area) with three theoretical predictions.

used to determine ω production yield for each bin of the Dalitz plot.

The normalized Dalitz plot variables are defined by:

$$X = \sqrt{3} \frac{T_+ - T_-}{Q_\omega}, \quad Y = \frac{3T_0}{Q_\omega} - 1, \quad (5)$$

with

$$Q_\omega = T_+ + T_- + T_0. \quad (6)$$

and T_i – the kinetic energies of the pions in the ω rest frame (centre-of-mass frame of the three-pion system). In the analysis polar Dalitz plot variables Z and ϕ related to X and Y by

$$X = \sqrt{Z} \cos \phi, \quad Y = \sqrt{Z} \sin \phi \quad (7)$$

are used.

The definition of Dalitz plot bins is introduced in Fig. 69 and the resulting distribution is shown in Fig. 70 for the three data sets. A deviation from pure P -wave phase space is observed and parametrized by a linear term $1 + 2\alpha Z$, with α determined to be $+0.147 \pm 0.036$, *i.e.* a positive value with 4.1σ significance. The result is dominated by statistical uncertainty. The comparison to theoretical predictions for the α parameter is shown in Fig. 71. A corresponding publication is in preparation (preprint available at arXiv:1610.02187).

6.7 Charge symmetry breaking in $dd \rightarrow {}^4\text{He}\pi^0$

Symmetries and symmetry breaking patterns in the non-perturbative regime of QCD is a key issue of the physics program of WASA-at-COSY. One objective is the determination of higher partial wave contributions to the charge symmetry breaking amplitude in the reaction $dd \rightarrow {}^4\text{He}\pi^0$ at higher energy. Charge symmetry is a subgroup of isospin symmetry being broken by the different masses of the up and down quarks as well as by electromagnetic interaction. In order to get access to quark mass effects on the hadronic level it is favorable to look at charge symmetry breaking (CSB) rather than isospin breaking observables as the relative pion mass difference, which is of electromagnetic origin, does not contribute.

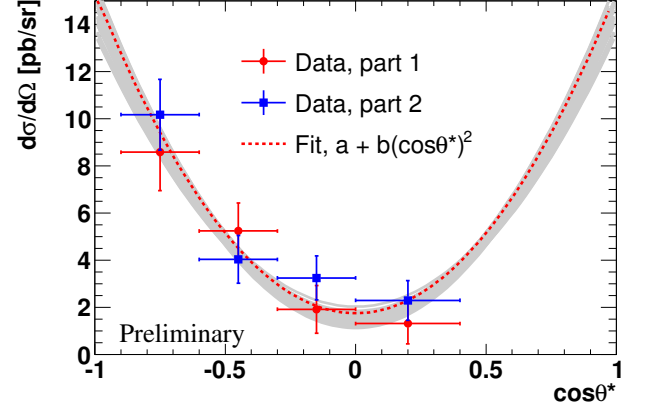


Fig. 72: Preliminary differential cross section as function of the π^0 emission angle in the center-of-mass system. Data from both parts of the beam time are shown separately (red and blue points). A fit to the data up to second order in $\cos\theta^*$ (red dashed curve) as well as the systematic errors (grey band) has been added.

The reaction $dd \rightarrow {}^4\text{He}\pi^0$ is forbidden by charge symmetry and, thus, is a direct measure of the CSB amplitude.

Previous investigations comprise a measurement close to threshold at IUCF and a first measurement with the WASA detector at COSY at an excess energy of $Q = 60\text{MeV}$. Both aimed primarily at the total cross section and did not provide decisive information on the differential distribution. Such data are, however, crucial for calculations within the framework of Chiral Perturbation Theory currently under way.

Based on the first experiment with WASA (see Phys. Lett. B **739** (2014) 44) a new measurement aiming at higher statistics and using a modified detector setup has been performed in 2014: a 1.5 m long time-of-flight path in forward direction improves particle identification and energy reconstruction. This was achieved by removing most of the detector elements in forward direction leaving only two thin scintillator layers close to the exit window, the forward tracking detector and the former veto hodoscope as stopping layer. In addition to the detection of the ${}^4\text{He}$ ejectile the two decay photons of the π^0 are registered in the WASA calorimeter. Final separation between ${}^3\text{He}$ and ${}^4\text{He}$ has been done by means of a kinematic fit testing the final-state hypotheses ${}^3\text{He}\pi\gamma\gamma$ and ${}^4\text{He}\pi\gamma\gamma$ requiring overall energy and momentum conservation. No constraint for the π^0 has been included in order not to introduce a fake π^0 signal. Compared to the previous experiment the number of events in the final missing mass plot could be increased by roughly a factor of 4. For acceptance correction the measured angular distribution has been utilized in an iterative procedure, for absolute normalization the reaction $dd \rightarrow {}^3\text{He}\pi^0$ has been used. A total cross section of $\sigma_{\text{tot,prel}} = (79.1 \pm 7.3(\text{stat})^{+1.2}_{-10.5}(\text{syst}) \pm 8.4(\text{norm})) \text{pb}$

has been obtained, which is smaller than the previous result, but still consistent within the error margins.

Due to the identical particles in the initial state, odd and even partial waves do not interfere and the angular distribution is symmetric with respect to $\cos\theta^* = 0$. If one considers only terms up to second order in pion momentum, in final state only s -wave, p -wave and s - d interference terms contribute and the differential cross section can be written as $d\sigma/d\Omega = a + b\cos^2\theta^*$. In this context a p -wave contribution to the parameter b always has a negative sign. However, Fig 72 shows a differential cross section following a parabola with a positive quadratic term. The fitted parameters are $a = (1.75 \pm 0.46(\text{stat})_{-0.8}^{+0.31}(\text{syst}))$ pb/sr and $b = (13.6 \pm 2.2(\text{stat})_{-2.7}^{+0.9}(\text{syst}))$ pb/sr, i.e. the parameter b significantly differs from zero and is positive. This means that it is not sufficient to consider only s - and p -wave in final state — which is what the current theoretical approaches contain — but also to take into account (at least) d -wave contributions. A corresponding publication is currently in preparation.

7 Further Experimental Activities

7.1 Photo production of the π^0 meson up to 5.5 GeV with CLAS

The first high precision measurement of exclusive π^0 photo production cross section in Dalitz decay and conversion mode has been measured in CLAS setup at Thomas Jefferson National Accelerator Facility. The measurement is performed in the reaction $\gamma p \rightarrow pe^+e^-X(\gamma)$ using tagged photon beam spanning in energy interval, covered “resonance” and “Regge” regimes, $E = 1.25 - 5.55$ GeV. In the final state of the reaction, the particles $p; e^+; e^-$ are detected while the photon is not detected. The π^0 meson is identified in the missing mass of proton. This new data quadrupled the world bremsstrahlung database above $E = 2$ GeV. Our data appear to favor the Regge pole model and constituent counting rule (CCR) while disfavor handbag model.

In elementary particle physics involving center-of-mass energies (W) less than 2.5 GeV (“resonance” regime), the study of lightest mesons (π^0 and η) in photo production has always been a complementary tool to elastic πN scattering. At high energies single pion photo production can be used to test predictions of Regge theory, in which recent calculations have shown to describe the presented data well. Furthermore, these measurements have shown that the differential cross section for single pion production at fixed c.m. angles, $\theta_{c.m.}$, of 70° , 90° and 110° seem to scale as $\frac{d\sigma}{dt} \sim s^{2-n} f(\theta_{c.m.})$, where s and t are the Mandelstam variables and n is the total number of interacting elementary fields in the initial and final state of the reaction. This is predicted by the constituent counting rule and exclusive measurements in pp and $\bar{p}p$ elastic scattering, meson-baryon Mp reactions, and photo production γN agree well with this rule. This experiment is a unique opportunity to bridge resonance and high-energy, in particular, “Regge”, regimes and increases available database above resonance range by significant amount.

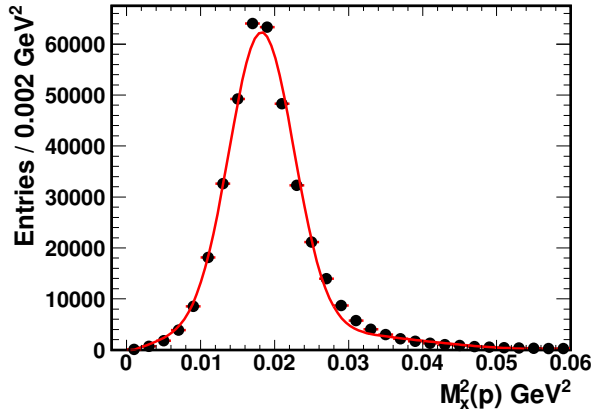


Fig. 73: Peak of π^0 in the missing mass of proton for events with $pe^+e^-(\gamma)$ in final state.

7.1.1 Data analysis

The missing mass of proton for events with $pe^+e^-(\gamma)$ in final state shown in Fig. 73. The selected strategy of the analysis of $g12$ data allowed to have negligible background. The fit (shown by red solid line) performed with the Crystal Ball function plus 3rd order polynomial function results in $M_{\pi^0}^2 = 0.0182$ GeV² and the Gaussian $\sigma = 0.0043$ GeV².

Lepton identification was based on conservation of mass. Once the data is skimmed for p, π^+, π^- , all particles that were π^+, π^- were tentatively assigned to be electrons or positrons based on their charge. The analysis employed three separate kinematic fitting hypotheses, 4-C, 1-C, and 2-C, as well as a cut on the missing energy of the detected system. The 4-C fit used the $\gamma p \rightarrow p\pi^+\pi^-$ channel to filter background from double charged pion production from single π^0 production. The 1-C fit was used for the topology of $\gamma p \rightarrow pe^+e^-(\gamma)$ to fit to a missing final state photon. The 2-C fit was used for the topology of $\gamma p \rightarrow pe^+e^-(\gamma)$ to fit to a final state photon but also to constrain the invariant mass of $e^+e^-(\gamma) = m_{\pi^0}^2$. The “confidence levels” for each constraint were consistent between $g12$ data and Monte-Carlo simulations.

The remainder of the background was attributed to $\pi^+\pi^-$ events. To reduce the background further, a comparison of the missing mass squared of the proton and the pe^+e^- missing energy of the system was performed. This comparison revealed that the majority of $\pi^+\pi^-$ background has missing energy less than 75 MeV. To eliminate this background all events with a missing energy less than 75 MeV were removed.

Overall, angular independent systematic uncertainty varies between 9% and 12% as a function of photon energy. The individual contributions came from particle efficiency, sector-to-sector efficiency, flux determination, missing energy cut, 4-C, 2-C, and 1-C pull probability, target length, branching ratio, fiducial cut, and z-vertex cut.

7.1.2 Results

The new CLAS high statistical cross sections, obtained here, for $\gamma p \rightarrow \pi^0 p$ are compared in Fig. 74 with previous data from tagged JLab CLAS $g1c$ measurements, and bremsstrahlung DESY, Cambridge Electron Accelerator (CEA), and SLAC, and Electron Synchrotron at Cornell Univ. experiments. The overall agreement is good, specifically with the tagged CLAS $g1c$ data.

At higher energies (above $s \sim 6$ GeV²) and large angles ($\theta \geq 90^\circ$) in c.m., the results are consistent with the s^{-7} scaling expected from the quark counting rule. The black dash-dotted line on 90° (Fig. 74) is a result of the fit of new CLAS $g12$ data only, performed with power function $\sim s^{-n}$, leading to $n = 6.89 \pm 0.26$. Oscillations observed at 50° and 70° up to $s \sim 10$ GeV² indicate that the quark counting rule requires higher energies and higher $|t|$ to prove it.

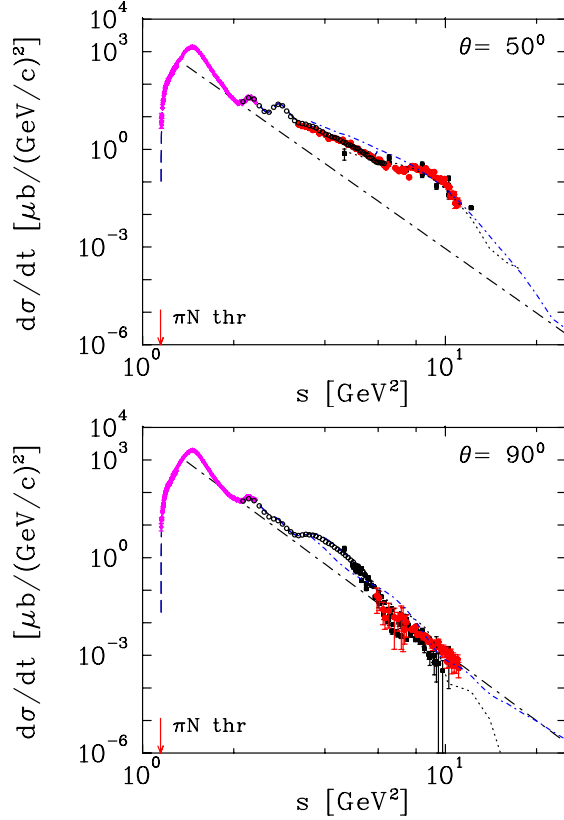


Fig. 74: Differential cross section of $\gamma p \rightarrow \pi^0 p$ $d\sigma/dt(s)$ at 50° and 90° in c.m. as a function of c.m. energy squared, s . The red filled circles are results from the current analysis of the CLAS Collaboration g12 data. The black open circles are results from CLAS g1c and magenta open diamonds with crosses are A2 at MAMI Collaboration. While black filled squares are data from old bremsstrahlung measurements above $E = 2$ GeV. Plotted uncertainties are statistical. The blue dashed line corresponds to the SAID PWA DU13 solution (no new CLAS data are in the fit). Black dot-dashed lines are plotted as the best fit result for 90° case. Pion production threshold shown as a vertical red arrow. Regge results are given by black dotted and blue short dash-dotted, respectively.

In Fig. 75, the $d\sigma/dt(|t|)$ values are shown along with predictions from Regge pole and cut models and the handbag model.

Above $\cos\theta \geq 0.6$ (c.m.s. value), there is a small difference between different Regge approaches. Overall, the Regge approximation becomes less relevant below $E = 3$ GeV. The dip around $\cos\theta = 0.2 - 0.4$ agrees with presented CLAS data. This is surprising, as there was no evidence found before (with the actual data) for this dip. Since dips are observed, a mechanism for producing those dips is provided by final state interactions which correspond to Regge cuts.

Since this data reaches all $|\cos\theta|$, it is interesting to see how the old model fares in an enlarged range. Remarkably, with a lowering of the original Pomeron strength, the model fits the data fairly well up to the 90° . The description of the π^0 photo production cross sections at largest $|t|$ requires some improvement of the Regge model probably by including u-channel exchange.

Simultaneously, Fig. 75 shows that the new CLAS data are orders of magnitude higher than the handbag model for π^0 photo production below $s = 11$ GeV².

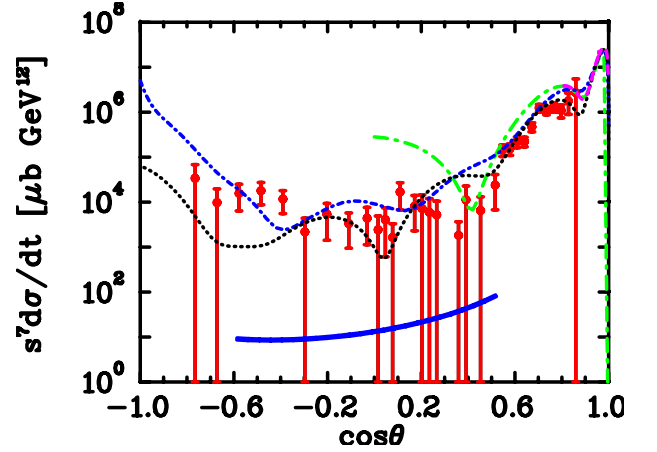


Fig. 75: Differential cross section of π^0 photo production. CLAS experimental data at $s = 11$ GeV² are from the current g12 experiment (red filled circles). Regge results are given by black dotted, blue short dash-dotted, green long dash-dotted, and magenta long dashed lines. The handbag model by Kroll at $s = 10$ GeV² (blue double solid line).

7.1.3 Conclusions

A significant increase in the comprehensiveness of the database for observables in the meson photo production process is critical to reaching definitive knowledge about QCD-based models of the nucleon. Studies that cover a broad range of c.m. energy W are particularly helpful in sorting out the phenomenology.

Through the experiments described above, an extensive and precise data set (2030 data points) on the cross section for π^0 photo production from the proton has been obtained over the range of $1.81 \leq W \leq 3.33$ GeV. A novel approach based on the use of the Dalitz decay mode was employed for extracting the cross sections from the experimental data. Measurements are performed in the reaction $\gamma p \rightarrow pe^+e^-X(\gamma)$ using a tagged photon beam spanning the energy interval covered by "resonance" and "Regge" regimes.

The measurements obtained here have been compared to existing data. The overall agreement is good, while the data provided here quadrupled the world bremsstrahlung database above $E = 2$ GeV, more precise

than previous measurements, and cover the reported energies with finer resolution. By comparing this new and greatly expanded data set to the predictions of several phenomenological models, the present data were found to favor the Regge pole model and quark counting rule while disfavoring the handbag approach.

7.2 Transition form factor of the η' meson with CLAS12

One of the currently most promising candidates to provide a signal for physics beyond the SM is the muon anomaly. It is a low-energy observable, which can be both measured and computed to high precision. For the muon, as well as for the electron and tauon, the anomaly a differs slightly from zero (of order 10^{-3}) because of radiative corrections. In the Standard Model, contributions to the anomaly come from virtual ‘loops’ containing photons and the known massive particles. The present experimental value $a_\mu^{\text{EXP}} = 1\,165\,920\,89(63) \times 10^{-11}$ deviates from the SM prediction by about 3 standard deviations $\Delta a_\mu^{(\text{EXP-SM})} = (287 \pm 80) \times 10^{-11}$ or $= (261 \pm 78) \times 10^{-11}$, depending on how the leading-order hadronic contributions are evaluated. While this discrepancy is not large enough to claim a failure of the SM, it is currently the largest deviation of a SM prediction from an experimental observable. This alone justifies the efforts currently taken to improve both the theoretical as well as the experimental value.

The largest uncertainty of the SM prediction comes from the hadronic quantum corrections. At the level of accuracy that is relevant at the moment the hadronic contributions can be split up into the hadronic vacuum polarization (HVP) and the hadronic light-by-light scattering (HLbL). The most important contribution to the latter comes from the pseudoscalar pole contributions. For those one expects that the contribution should be largely saturated by the lightest exchange particles, namely the π^0 , the η and the η' . Fortunately there is a way to quantify hadronic corrections. It requires both theoretical as well as experimental efforts: Dispersion theory provides a link between particular hadronic cross sections and a_μ . In particular for the latter contribution it allows one to calculate from the transition form factors of the kind π^0 , η , $\eta' \rightarrow \gamma^* \gamma^*$ the corresponding piece for the meson pole contribution.

The measurement that was proposed will provide important information towards the necessary input needed for the evaluation of the HLbL contribution, since $\eta' \rightarrow \gamma^* \gamma$ gives the single off-shell form factor of the η' , this is also known as a Dalitz decay.

7.2.1 Time-like approach

Dalitz decays are radiative decays in which the photon is virtual and subsequently produces an electron positron pair, $P \rightarrow l^+ l^- X$. Such decays serve as an important tool used to reveal the internal structure of hadrons and the in-

teraction mechanisms between photons and hadrons. Furthermore, assuming point-like particles, the electromagnetic interaction is calculable within QED by the Kroll-Wada formula. Transition form factors quantify modifications of the point-like photon-meson vertex due to the transitions and interactions of the meson. The transition form factor can be characterized as $|F(q^2)|$, where q^2 is the square of the invariant mass of the lepton pair, and can be determined by comparing QED predictions to the experimentally measured rate. The proposed measurement will aid in limiting the largest uncertainty of the Standard Model prediction for hadronic quantum corrections in the muon anomaly.

7.2.2 Time-like form factor

It has been experimentally observed that the shape of the dilepton mass spectrum deviates significantly from the QED predictions, displaying a rise at larger dilepton mass. Therefore, the form factor $M_P(p^2, k^2 = 0)$ or $M_P(p_1^2, p_2^2)$ can be written as follows:

$$M_P \rightarrow M'_P \times |F(q^2)|, \quad (8)$$

where M'_P is the decay constant of two photons, while $|F(q^2)|$ is called the transition form factor, which defines the electromagnetic space structure of the meson. According to that, the $\eta' \rightarrow e^+ e^- \gamma$ decay rate modifies as:

$$\frac{d\Gamma_{e^+e^-\gamma}}{\Gamma_\gamma d q^2} = \frac{2\alpha}{3\pi} \frac{1}{q^2} \left(1 - \frac{q^2}{m_l^2}\right)^3 \left(1 + \frac{2m_l^2}{q^2}\right) \times \left(1 - \frac{4m_l^2}{q^2}\right)^{\frac{1}{2}} |F(q^2)|^2.$$

First observations were described with standard vector meson dominance (VMD) where the virtual photon can stem from intermediate vector mesons. The value of $|F(q^2)|$ can be directly measured by comparing QED predictions to the measured rate.

$$\frac{d\Gamma(A \rightarrow B + l^+ l^-)}{d q^2 \Gamma(A \rightarrow B \gamma)} = \left[\frac{d\Gamma}{d q^2} \right]_{\text{QED}} \cdot |F(q^2)|^2 \quad (9)$$

or by performing a line shape analysis on the $l^+ l^-$ invariant mass using assumptions on the structure of $|F(q^2)|$. One such assumption for $|F(q^2)|$ is the dipole approximation from the VMD model, which can be parametrized as:

$$F(q^2) = \frac{1}{1 - q^2/\Lambda^2} \quad (10)$$

where the parameter Λ corresponds to the mass for the effective contributing vector meson.

7.2.3 Proposed measurement with CLAS12

From previous CLAS analyses, it was shown that measurements of the time-like transition form factor were

achievable, but without the statistical precision needed to be competitive. Therefore, we proposed to use the CLAS12 detector to measure the Dalitz decay channel of the reactions $ep \rightarrow e'p\eta'$, where $\eta' \rightarrow e^+e^-\gamma$, through detection of the final state proton and η' decay products. Preliminary studies using the CLAS12 simulation suite have shown that a beam time of 80 days, at full luminosity (10^{35}), will accumulate a data sample at least one order of magnitude larger in statistics than the most current $\eta' \rightarrow e^+e^-\gamma$ measurement and would yield a statistical uncertainty $\lesssim 0.5\%$.

7.2.4 Particle identification with CLAS12

The η' meson have pion decay modes, which are orders of magnitude greater than the Dalitz decay. For example, the ratio $\Gamma_{\pi^+\pi^-\gamma}/\Gamma_{e^+e^-\gamma}$ is $6.2 \cdot 10^2$. Electrons/positrons will be identified by using the information from the High Threshold Cherenkov counters (HTCC) and Electro-magnetic Calorimeters (PCAL+EC). The expected e^\pm/π^\pm rejection factor for single particles ($p < 4.9$ GeV) is 10^5 . This results in a $e^+e^-/\pi^+\pi^-$ rejection factor of 10^{10} . Therefore, the amount of $\pi^+\pi^-$ background in the $M(e^+e^-)$ spectrum will be $\approx 6.2 \cdot 10^2/10^{10} = 6.2 \cdot 10^{-8}$.

7.2.5 Expected yield with CLAS12

The rate for mesons in electro-production where the scattered electron is left undetected ($W=1.9-2.7$ GeV) is ~ 80 kHz. This rate, along with the production cross-section ($\sigma(W)$), the average detection efficiency, $\varepsilon \approx 5\%$, as well as the branching fraction $\mathcal{BR} = 4.69 \cdot 10^{-4}$ for $\eta' \rightarrow e^+e^-\gamma$ leads to an expected rate of $\frac{28,200 \text{ events}}{80 \text{ Days}}$. This rate is 35 times more in statistics than the most current available measurement.

The expected QED normalized spectrum for this measurement is shown in Fig. 76. There were two acceptance models (i.e. flat and QED+VMD) used to determine the transition form factor. It is shown that there exists a systematic uncertainty depending on the chosen acceptance model. However, the final calculation on the slope parameter or the TFF shows a negligible impact of this uncertainty. Regardless of the acceptance model, it is shown in Fig. 76 that the accumulated statistics collected by CLAS12 allow for a precision of each parameter $\lesssim 0.5\%$, with an expected systematic uncertainty on the measurement to be no less than

$$b_n^{\text{sys}} = 0.0497\%$$

$$\Lambda_{\text{sys}}^2 = 0.0494\%.$$

7.2.6 Approved beam time request

With this proposal and beam time request, we asked to run for 80 days parallel with the beam time already approved for Run-group A. The 80 day request was ap-

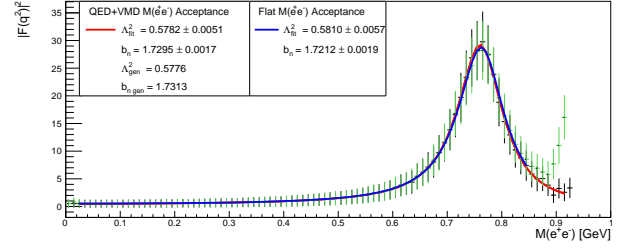


Fig. 76: $|F(q^2)|^2$ as a function of $M(e^+e^-)$ using two acceptance models. (black points) QED+VMD $M(e^+e^-)$ acceptance model. (green points) Flat $M(e^+e^-)$ acceptance model. The solid lines represent a fit using Eq. 10 to the data points.

proved. This request will provide a competitive data sample of $\eta' \rightarrow e^+e^-\gamma$.

7.2.7 Conclusion

Compared to current experimental uncertainties of 10% and differences in theoretical approaches of $\approx 10\%$, this approved proposed measurement by CLAS12 would not only be in the position to decisively discriminate between the theoretical predictions, but also pin down one of the largest uncertainties to the muon g-2 anomaly.

7.3 A spin-off from COSY: Production and interaction of polarized molecules

The polarized targets of experiments like ANKE or PAX at COSY consist of T-shaped storage cells that are filled with polarized hydrogen or deuterium atoms produced by a polarized atomic beam source (ABS). The target density is increased by these cells up to two orders of magnitude, because the COSY beam can interact with these atoms until they are leaving the cell after a few hundred wall collisions. The polarization of the atoms is conserved by a special coating of the inner surface. Further development of this technique led to the idea to recombine the polarized atoms into molecules without polarization losses. In this case, the target density is increased due to the slower velocity of the molecules compared to the atoms, which will increase the time of flight of the molecules inside the cell.

For this purpose, a collaboration between the Petersburg Nuclear Physics Institute (PNPI), the Institute of Nuclear Physics of the University of Cologne, and the IKP built a dedicated apparatus to investigate the influence of different parameters like external magnetic fields, temperatures or the surface materials. The recombination takes place on the surface of the cells only and not in the gas phase, because the pressure inside does not exceed 10^{-4} mbar. The atoms and molecules are ionized by an electron beam and the produced ions (protons/deuterons or H_2^+/D_2^+ and even HD^+) are accelerated into a Lamb-shift polarimeter, where the nuclear polarization is measured.

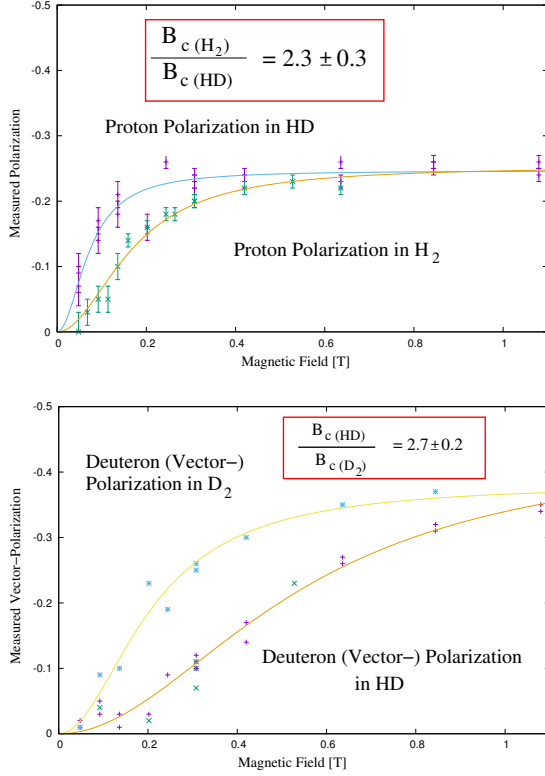


Fig. 77: Up: The measured polarization of protons in H_2 and HD molecules as a function of the external magnetic field after the recombination of polarized hydrogen (and deuterium) atoms on a gold surface at 80 K. The measured ratio of the coupling between the rotational magnetic moment and the proton spin of 2.3 ± 0.3 fits to the expected value of 2.37.

Down: The measured vector-polarization of deuterons in D_2 and HD molecules as a function of the external magnetic field. The measured ratio of the critical magnetic fields of 2.7 ± 0.3 is only a little bit smaller than expected value of 3.3 from a first order approximation.

Due to the rotational quantum number J of the molecules the inhomogeneous charge distribution is producing a magnetic moment B_{rot} that can couple with the nuclear spins I of the protons/deuterons within the molecules. The magnetic field seen by the protons in the H_2 molecule is $B_c = B_{rot}/r^3 = 5.4$ mT. When the rotational magnetic moment of the molecules is randomized during wall collisions, it will affect the nuclear polarization that will be lost after a few wall collisions. An external magnetic field B is able to decouple the nuclear spin I from J and will decrease the polarization loss per collision. Like shown in Fig. 77 the polarization of an ensemble of polarized molecules in a magnetic field B with original polarization P_0 after n wall collisions is:

$$P(B) = P_0 e^{-n(B_c/B)^2} \quad (11)$$

Due to the exponential distribution of the number of wall collisions n inside the cell $W(n) = \alpha e^{-\alpha n}$ the average number of wall collisions is $\bar{n} = \ln 2/\alpha$ and the formula can be deconvolved to:

$$P = \frac{P_0}{1 + \frac{\bar{n}}{\ln 2} \frac{B_c}{B}} \quad (12)$$

The parameter α depends on the geometry of the cell (400 mm long, 10 mm inner diameter) and the typical average number of wall collisions is $\bar{n} = 125$.

In a first order approximation the distance of the nucleons $d = 2r$ in a H_2 , D_2 or HD molecule and even the rotational magnetic moment B_{rot} are equal. But compared to the other molecules the rotation axis of the HD molecule is shifted closer to the deuteron. Therefore, the distance of the rotational magnetic moment B_{rot} to the deuteron is decreased to $r' = 2/3r$ and increased to $r'' = 4/3r$ for the proton. This means, that the critical field B_c for the proton inside the HD molecule is decreased to $B_c(HD) = (3/4)^3 B_c(H_2) \sim 2.37 B_c(H_2) \sim 2.3$ mT and for the deuteron it is increased by a factor $(3/2)^3 \sim 3.34$. This simple estimation corresponds well with the measurements, when the polarization of the proton (deuteron) in the H_2 (D_2) molecule is compared with the proton (deuteron) in the HD molecule.

For more precise calculations the temperature dependence of the rotational magnetic moment must be taken into account. While J is always odd for hydrogen molecules with parallel nuclear spins (ortho-hydrogen) and $J = 1$ at temperatures below 200 K, the corresponding (ortho-)deuterium molecules allow even J only and the occupation numbers of $J = 0, 2$ or higher quantum states vary in this temperature range. For hydrogen, the $J = 0$ state is found for anti-parallel spins only and, therefore, polarized hydrogen molecules cannot be frozen out and stored as ice. The situation is totally different for deuterons, because only the $J = 0$ state is occupied by polarized molecules at temperatures below 40 K and the production and storage of polarized deuterium and HD molecules seems to be in range. These polarized molecules can be used as improved targets in coming experiments at accelerators. In addition, they might be used to increase the energy output or reduce the costs of fusion reactors, because the fusion cross sections are spin-dependent. But polarized fuel, i.e. nuclear-polarized deuterium, was missing for further tests until now.

This new technique opens new insights in chemical reactions, i.e. the recombination of hydrogen atoms or the adsorption on different surfaces, because the nuclear spin was never observed meanwhile. Conserving the nuclear spin during chemical reactions, like it was shown for the recombination of hydrogen on a surface made of Perfluoropolyether, might allow to produce spin-polarized tracer materials for medicine by attaching a polarized hydrogen(deuterium) atom without polarization loss. In this case, the resolution of NMR scans can be improved by orders of magnitude and new possibilities for corresponding diagnostic techniques are just around the corner.

7.4 PAX/TRIC detector development

At the Cooler Synchrotron COSY a novel (P-even, T-odd) null test of time-reversal invariance to an accuracy of 10^{-6} is planned as an internal target transmission experiment. The parity conserving time-reversal violating observable is the total cross-section asymmetry $A_{y,xz}$. This quantity is measured using a polarized proton beam with an energy of 135 MeV and an internal tensor polarized deuteron target from the PAX atomic beam source. The reaction rate will be measured by means of an integrating beam current transformer.

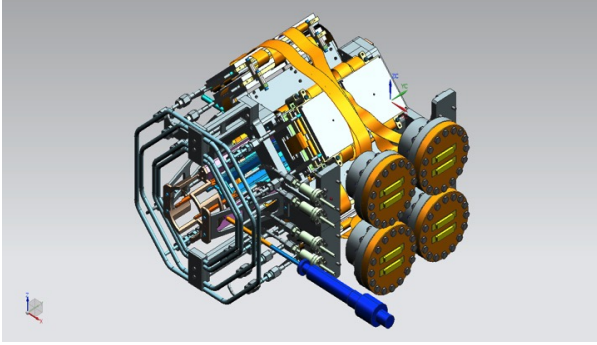


Fig. 78: Sketch of the PAX detector assembly consisting of four quadrants and two individual cooling circuits.

Part of the PAX/TRIC developments of the past years were devoted to the design and realization of a large acceptance silicon detector. The PAX/TRIC silicon detector has been realized in collaboration between the University and INFN of Ferrara (Italy) and the FZJ. It is a multipurpose silicon vertex detector installed around the storage cell of the polarized H/D target. It is supposed to determine the beam and target polarizations by detection of asymmetries in pp- and pd-elastic scattering. In this perspective, it will provide an absolute calibration of the atomic Breit-Rabi polarimeter of the polarized target. At the same time it will serve as a beam position monitor in the beam-target interaction region.

The detector is composed of four identical quadrants implemented in a diamond configuration (Fig. 78) around the openable storage cell storage cell. Each quadrant consists of three layers of double-sided silicon-strip sensors, mounted inside an aluminium box, and a front-end readout system (Fig. 80). Three kinds of 100 mm x 100 mm silicon sensors are mounted. Some of them have been recovered from the HERMES experiment at DESY-HERA.

- 1st layer: $2 \times$ HERMES 300 μm sensors
- 2nd layer: $2 \times$ PAX 300 μm sensors
- 3rd layer: $1 \times$ PAX 1000 μm sensor

Two separate cooling circuits cool down the electronic readout and silicon sensors.

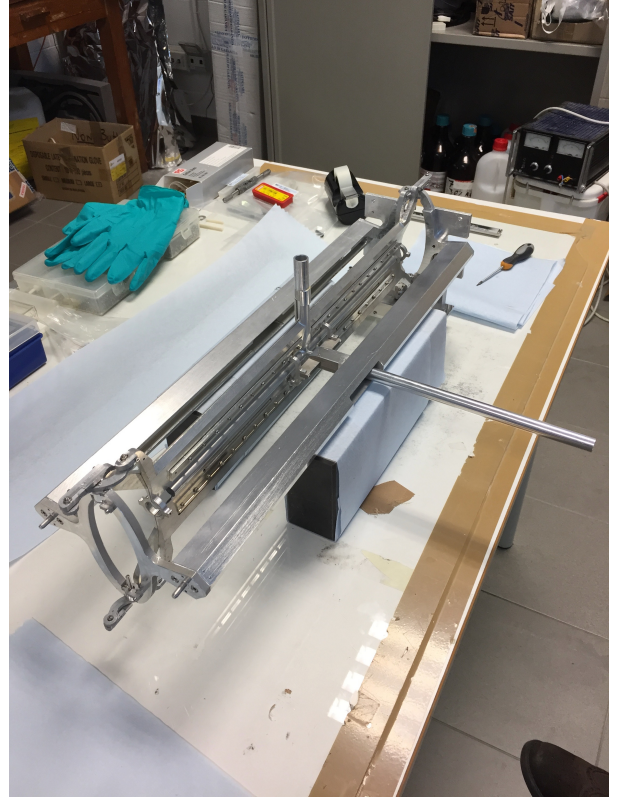


Fig. 79: The storage cell before insertion in the detector assembly.

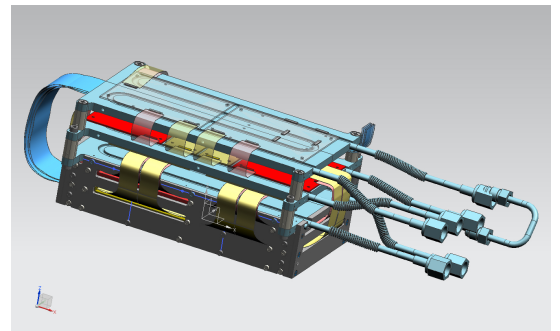


Fig. 80: Single detector quadrant including three layers of silicon-strip detectors operated by front-end electronic mounted on cooling plates directly behind the detectors.

Dedicated front-end boards have been developed. To make use of the hardware and software already developed for the ANKE experiment, the PCBs have been realized with the same VATA chips of the ANKE silicon telescopes. This allows also to employ the already developed readout chain, and with some modification, also of the related software.

A dedicated setup for the characterization and test of the silicon sensors and relative electronics has been assembled and put into operation at IKP. All the sensors have been characterized and calibrated with an α -source.

A new trigger system driven by FPGA programmable chips will replace the old NIM based logic. Low voltage and high voltage power supply will be provided by the MPOD Wiener crate system capable of handling both kinds of modules.

In January 2017, at the conclusion of a development plan including one year for the design and three years for the realization, the detector have been finally assembled with two complete quadrants and is ready for its first commissioning planned for March 2017 (Fig. 81).

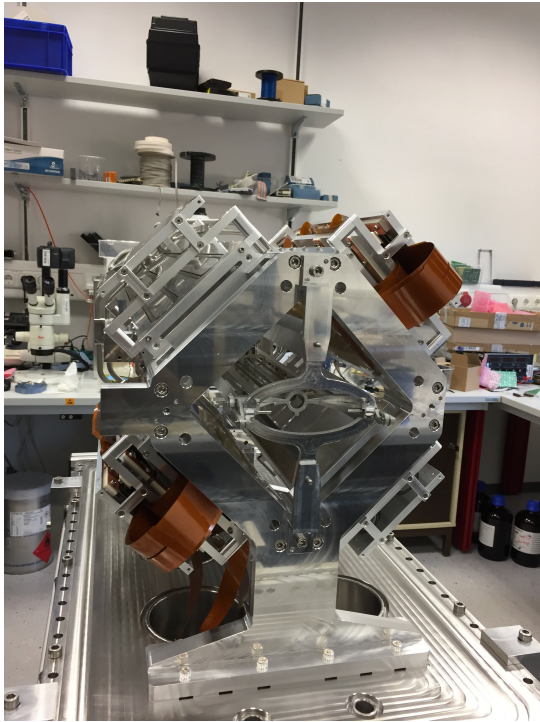


Fig. 81: Picture of the assembled detector with two complete quadrants. The storage cell can be identified in the center.

8 Theoretical Investigations

8.1 Introduction

The IKP theory group studies the strong interactions in their various settings — spanning topics in hadron structure and dynamics, the nuclear many-body problem, symmetry tests in Quantum Chromodynamics (QCD), physics beyond the Standard Model and strongly correlated electron systems. The first focus of the theory group is the formulation and application of effective field theories for precision hadron and nuclear physics based on the symmetries of QCD. The second focus is related to high performance computing in nuclear and hadronic physics, spear-headed by the work on nuclear lattice simulations. Since July 2012, the group is heavily involved in the activities of the collaborative research center “Symmetries and the emergence of structure in QCD” (CRC 110) together with researchers from Bonn University, TU München, Ruhr-Universität Bochum, IHEP/CAS (Beijing, China), ITP/CAS (Beijing, China) and Peking University (China). This CRC was just renewed for another funding period of 4 years. Some of the high-lights of these activities are discussed in the following.

8.2 Nuclear physics near a quantum phase transition

How do protons and neutrons bind to form nuclei? This is the central question of *ab initio* nuclear structure theory. While the answer may seem as simple as the fact that nuclear forces are attractive, the full story is more complex and interesting. We have presented numerical evidence from *ab initio* lattice simulations showing that nature is near a quantum phase transition, a zero-temperature transition driven by quantum fluctuations. Using lattice effective field theory, we perform Monte Carlo simulations for systems with up to twenty nucleons. For even and equal numbers of protons and neutrons, we discover a first-order transition at zero temperature from a Bose-condensed gas of alpha particles (${}^4\text{He}$ nuclei) to a nuclear liquid. Whether one has an alpha-particle gas or nuclear liquid is determined by the strength of the alpha-alpha interactions, see Fig. 82. We further have shown that the alpha-alpha interactions depend on the strength and locality of the nucleon-nucleon interactions. More precisely, we have constructed two extreme leading order interactions, consisting of one-pion exchange and smeared four-nucleon operators without derivatives. While the short-range terms of interaction A (V_A) are non-local, interaction B (V_B) contains in addition local short-distance operators. In both cases, the Coulomb interaction is included. While interaction A is fitted entirely to np phase shifts and the deuteron binding energy, the parameters of interaction B are further constrained by fitting the S-wave alpha-alpha scattering phase shifts at low energies. Note that interaction A fails to reproduce the α - α phase shifts. From this, one can define a one-parameter family of interactions, $V_\lambda = (1 - \lambda)V_A + \lambda V_B$ that allows to map

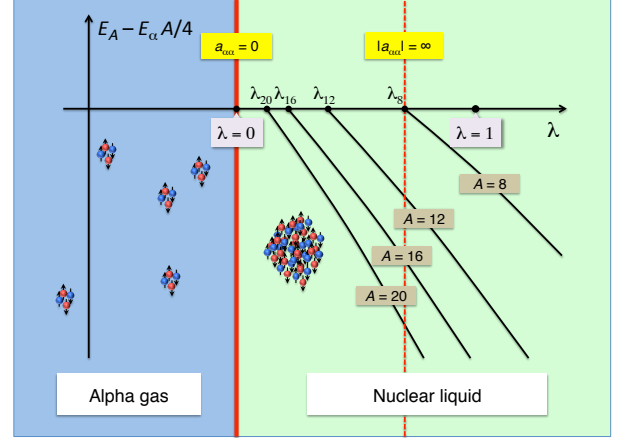


Fig. 82: Zero-temperature phase diagram. We show the zero-temperature phase diagram as a function of the parameter λ in the interaction $V_\lambda = (1 - \lambda)V_A + \lambda V_B$ without Coulomb included. The blue filled circles indicate neutrons, the red filled circles indicate protons, and the small arrows attached to the circles indicate spin direction. We show a first-order quantum phase transition from a Bose gas to nuclear liquid at the point where the scattering length $a_{\alpha\alpha}$ crosses zero. We have also plotted the alpha-like nuclear ground state energies E_A for A nucleons up to $A = 20$ relative to the corresponding multi-alpha threshold $E_\alpha A/4$. The last alpha-like nucleus to be bound is ${}^8\text{Be}$ at the unitarity point where $|a_{\alpha\alpha}| = \infty$.

out the behavior of nuclear binding at alpha-particle separation thresholds. In fact, $\lambda = 0$ corresponds to a vanishing alpha-alpha scattering length, whereas the unitarity point with diverging scattering length gives a bound ${}^8\text{Be}$ nucleus, while in nature this nucleus is unbound by about -0.1 MeV.

This insight should be useful in improving calculations of nuclear structure and important astrophysical reactions involving alpha capture on nuclei. Our findings also provide a tool to probe the structure of alpha cluster states such as the Hoyle state responsible for the production of carbon in red giant stars and point to a connection between nuclear states and the universal physics of bosons at large scattering length.

8.3 Nuclear structure using relative coordinates

Reliable nuclear structure calculations based on realistic nuclear interactions have become increasingly important in recent years. They are the basis for studying a wide variety of nuclear reactions aiming to better understand astrophysical processes or for devising experiments to pin down beyond-the-standard-model physics. Because many of their properties are very sensitively affected by

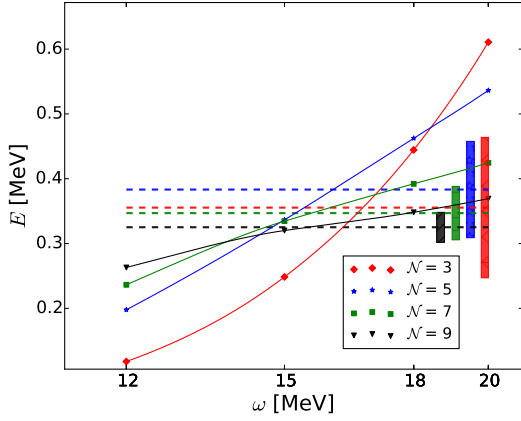


Fig. 83: Extraction of the excitation energy of the $\frac{1}{2}$ -state of ${}^7\text{Li}$ using the dependence on the HO frequency. The solid lines show the dependence for various basis sizes. The dashed lines give the averages and the bars indicate the standard deviation.

nuclear interactions including three- and possibly more-nucleon forces, they also serve as a benchmark for the verification of new realizations of nuclear interactions.

One important tool for such calculations is the no-core shell model (NCSM) where the many-body Schrödinger equation is solved in an antisymmetrized harmonic oscillator (HO) basis. Although the NCSM is an efficient way to represent the pertinent dynamical equations, nuclear structure calculations are still computationally demanding due to the complexity of nuclear interactions. It is most efficient to describe the quantum mechanical many-body states in terms of relative coordinates to take full advantage of translational and rotational invariance. Despite these benefits, most NCSM calculations have been performed using single particle basis states in the past since it has been difficult to build an antisymmetrized set of relative coordinate basis states that allows one to enforce the Pauli principle.

We have recently introduced an algorithm to obtain the antisymmetrized HO states for light p-shell nuclei. In this work, these states are calculated for several light nuclei and also the recoupling coefficients for the application of two-nucleon and three-nucleon (3N) operators are given. The generation of these states requires the numerical diagonalization of the antisymmetrizer. The basis states are therefore defined in terms of sets of coefficients defining how the antisymmetrized states is related to non-antisymmetrized HO state. Due to the large number of states, the determination of these coefficients requires supercomputer resources. Once they have been obtained, solving dynamical equations in this basis is possible even with limited computational resources. Since the coefficients are electronically available, this allows other groups to perform nuclear structure calculations without the need to acquire supercomputers.

As an example, we study the dependence of binding and excitation energies on the HO frequency for several p-shell nuclei. The new approach allows one to perform a large number of such calculations. Thereby, we showed that it becomes possible to extract in a systematic way, the energies and their uncertainty from the known dependence on the HO frequency. Fig. 83 shows the dependence of the first excitation energy E of the $J = \frac{1}{2}$ state of ${}^7\text{Li}$ on HO frequency ω . The different solid lines are results for different basis sizes constrained by the maximal HO excitation taken into account. As expected, the frequency dependence becomes smaller for larger bases. The extraction of the averages and variances allows to determine the final results for the excitation energy and an estimate for the numerical uncertainty. It is seen that the results for increasing basis sizes are consistent with each other and that the excitation energy can be obtained with high accuracy. The sets of basis states and transition coefficient will allow to pin down 3N forces with high precision. The use of relative coordinates will also enable first applications for four-nucleon interactions for p-shell nuclei. Since the results are electronically available to other groups, this work will trigger a wide variety of possible applications.

8.4 $\Lambda\Lambda$ and ΞN interactions in chiral effective field theory

The interaction between baryons in the strangeness $S = -2$ sector ($\Lambda\Lambda$, ΞN , $\Sigma\Lambda$, $\Sigma\Sigma$) has been in the focus of interest for many years. Specifically, the so-called H -dibaryon has played a prominent role. The H -dibaryon, a deeply bound 6-quark state with $S = -2$, $J = 0$ and isospin $I = 0$, was predicted by Jaffe within the bag model and should appear in the coupled $\Lambda\Lambda - \Xi N - \Sigma\Sigma$ system. So far none of the experimental searches for the H -dibaryon led to convincing signals. Recently, evidence for a bound H -dibaryon was claimed based on lattice QCD calculations. Extrapolations of those computations, performed for $M_\pi \gtrsim 400$ MeV, to the physical pion mass suggest, however, that most likely the H -dibaryon disappears into the continuum.

Recently, we have presented an investigation of the baryon-baryon (BB) interaction in the strangeness $S = -2$ sector within $\text{SU}(3)$ chiral effective field theory (EFT) to next-to-leading order (NLO) in the chiral expansion. At NLO there are contributions from one- and two-pseudoscalar-meson exchange diagrams and from four-baryon contact terms without and with two derivatives. As in case of our study to the ΛN and ΣN systems, $\text{SU}(3)$ flavor symmetry is used as guiding principle in the derivation of the interaction. This means that all the coupling constants at the various baryon-baryon-meson and baryon-baryon-meson-meson vertices are fixed from $\text{SU}(3)$ symmetry and the symmetry is also exploited to derive relations between the contact terms. The $\text{SU}(3)$ symmetry is, however, broken by the masses of the pseu-

doscalar mesons (π , K , η) and of the baryons for which we take the known physical values.

There are no genuine scattering data for the $\Lambda\Lambda$ and ΞN systems at low energies. However, other information from few- and many-baryon systems puts qualitative constraints on the BB interaction with strangeness $S = -2$. Those constraints were utilized as guideline for constructing our interaction.

In the course of our study it turned out that a simultaneous description of ΛN and ΣN data and of the few data and upper limits in the $S = -2$ sector is not possible if one insists on strict SU(3) symmetry of the contact interactions. First, one would get a much too attractive $\Lambda\Lambda$ interaction, incompatible with the fairly small separation energy measured for the ${}_{\Lambda\Lambda}^6\text{He}$ hypernucleus. Secondly, the interaction in the ΞN system would be too strong and one overshoots the experimental upper limit for the $\Xi^- p$ cross sections, see the blue bands in Fig. 84. Therefore, we have re-adjusted the low-energy constants (LECs) representing the strength of the contact terms in order to satisfy the experimental constraints on the $\Lambda\Lambda$ and ΞN systems. The resulting BB interaction in the $S = -2$ sector is then relatively weak. A selection of our final results are shown in Fig. 84 where the red bands correspond to the NLO interaction and the green band to our predictions at leading order (LO). Note that we still implement SU(3) symmetry for the LECs within the $\Lambda\Lambda - \Xi N - \Lambda\Sigma - \Sigma\Sigma$ systems. In any case we want to emphasize that an SU(3) breaking in the leading S -wave contact terms is in line with the employed power counting scheme.

8.5 The nucleon EDM from the flowed Weinberg operator

The gradient flow (GF) for gauge and fermion fields, used in combination with a lattice regulator, can probe the non-perturbative dynamics of QCD in advantageous manners. It is defined by a differential equation that gauge and fermion fields satisfy as a function of the space-time coordinates x and of a new scale, the flow-time t . The works by Lüscher and Weisz give us a complete understanding of the continuum limit of observables at non-vanishing flow-time. This allows us to use the GF to define observables that otherwise would be difficult to compute with standard methods. For example, we recently used the GF in a quenched calculation to determine the topological susceptibility relevant for determining nucleon EDM originating from the strong- θ term. Here we report on our initial findings of another operator using the GF that can induce a nucleon EDM: the Weinberg operator.

The Weinberg operator is the following dimension 6 operator

$$O_W = \frac{ig}{6} C_W f^{abc} G_{\mu\rho}^a G_{\nu\rho}^b G_{\lambda\sigma}^c \varepsilon_{\mu\nu\lambda\sigma}, \quad (13)$$

where G is the gluonic field strength tensor, ε is the anti-symmetric tensor, f are the structure constants of the gauge group, and C_W is the Weinberg coupling. This operator breaks both parity P and time-reversal T and thus

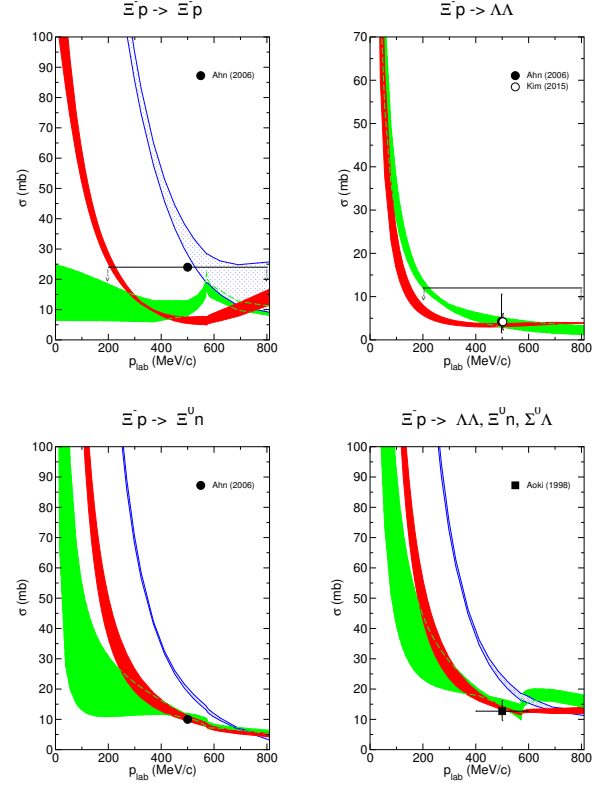


Fig. 84: Cross sections for $\Xi^- p$ induced reactions. NLO results for our chiral EFT interaction are shown by red bands, LO results by green bands. The blue bands are results that follow from a strict implementation of SU(3) flavor symmetry. The symbols represent data while bars are upper limits deduced from experiments.

also CP (because of CPT conservation), but it conserves charge conjugation symmetry C . It was introduced by Weinberg in the 1980s in the context of the CP -violating Higgs models. Weinberg realized that the effective operator Eq.(13) is induced by quark loops with the Higgs exchange containing a mixing between CP -even and CP -odd Higgs bosons. The Weinberg operator induces a contribution to the nucleon EDM directly and also mixing with the quark and quark-gluon contributions. Being an operator of purely gluonic parts, the renormalization pattern of the Weinberg operator can be greatly simplified using the gradient flow. We have implemented the Weinberg operator coupled with the GF and in fig. 85 we show the Monte Carlo history of this operator in one of our $N_f = 2 + 1$ lattice QCD gauge ensembles. To obtain the final nucleon EDM, the computation of the Weinberg operator as an insertion into the nucleon 3-point function is currently being performed using the variational method.

8.6 The decay $\omega \rightarrow \pi\pi$ revisited

The need to improve the theoretical description of the anomalous magnetic moment of the muon in partic-

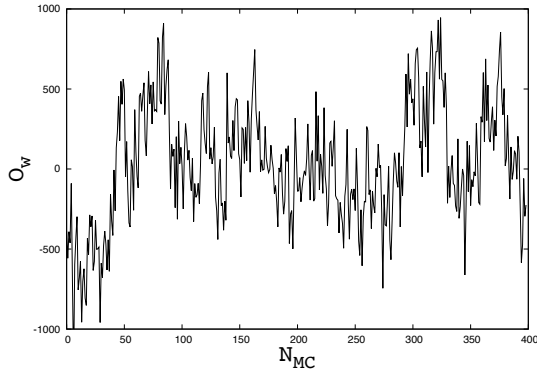


Fig. 85: Monte Carlo history of the Weinberg operator on the $N_f = 2 + 1$ ensemble corresponding to $M_\pi \simeq 650$ MeV.

ular calls for an improved understanding of the couplings of light mesons to vector currents. Traditionally those analyses were mostly done using models of the vector-meson dominance type, however, with improved $\pi\pi$ phase shift information nowadays a model-independent analysis of the two-pion channels became feasible based on dispersion theory. In the work presented here we focussed on an extraction of the branching fraction for $\omega \rightarrow \pi\pi$ from $e^+e^- \rightarrow \pi\pi$ as well as $\eta' \rightarrow \pi\pi\gamma$.

In our work we employed phase shifts provided by both the Madrid and the Bern groups as well as different fitting strategies. In addition we analyzed six different sets of experimental data for $e^+e^- \rightarrow \pi\pi$ as well as a set of pseudo-data for $\eta' \rightarrow \pi\pi\gamma$, since for the latter channel data of sufficient quality is not available yet (but expected soon from BESIII and CLAS). Our study revealed that while most of the experiments gave consistent results for the different fits the BaBar data clearly behaved differently. E.g. in a fit where the rho mass parameters was allowed to float only the BaBar data set called for a parameter outside the parameter range determined by the Madrid group. In addition, the analysis of the BaBar data also led to branching fractions for $\omega \rightarrow \pi\pi$ significantly outside the range suggested by a combined analysis of all other experiments—this is also clear from Fig. 86. We therefore excluded the BaBar data from our analysis and extracted from five recent data sets on $e^+e^- \rightarrow \pi\pi$

$$\text{Br}(\omega \rightarrow \pi\pi) = (1.46 \pm 0.08) \times 10^{-2}.$$

We also demonstrate that once data will be available for the two-pion invariant mass spectra from $\eta' \rightarrow \pi\pi\gamma$ an extraction of $\text{Br}(\omega \rightarrow \pi\pi)$ with similar accuracy as from the e^+e^- data will be possible. The pseudo-data used was generated based on a fit to preliminary data for this reaction from BESIII with equal statistics.

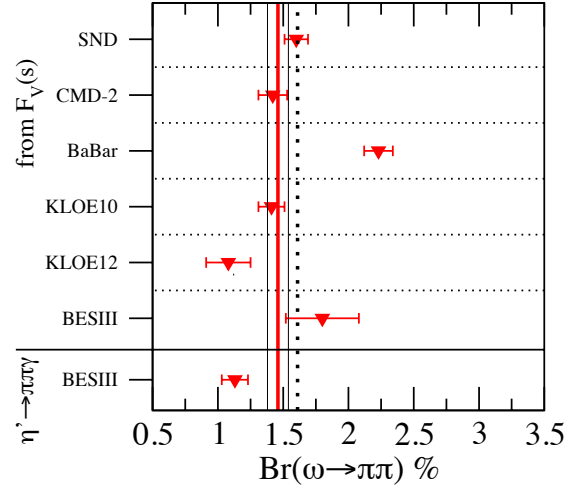


Fig. 86: $\text{Br}(\omega \rightarrow \pi\pi)$ extracted from 6 $e^+e^- \rightarrow \pi\pi$ experiments as well as pseudo-data for $\eta' \rightarrow \pi\pi\gamma$. The red and the solid black perpendicular lines show the central value and its uncertainty, respectively. The dotted one shows the central value that would have emerged had the BaBar data been kept in the average.

As a side result we also extracted an updated value for the pion vector radius. Also for this quantity the BaBar data set gave inconsistent results and was omitted. We find

$$\sqrt{\langle r_V^2 \rangle} = (0.6603 \pm 0.0005) \text{ fm}.$$

This value is an order of magnitude more accurate and 1.5σ lower than the current PDG average (0.672 ± 0.008) fm. In this context it is interesting to note that as soon as the data sets where the radius was extracted from $eN \rightarrow e\pi N$ are omitted from the average the central value for the radius drops to (0.663 ± 0.006) fully in line with our number.

8.7 The width of the Δ and Roper resonances at two-loop order

Chiral effective field theory provides a controllable perturbative approach of strongly interacting hadrons at low energies. A systematic power counting organizes the chiral effective Lagrangian and observables as a perturbative series in the Goldstone boson sector of QCD. Effective field theories (EFTs) with pions and nucleons proved to be more complicated, however, the problem of a consistent power counting in various ways. Due to the relatively small mass difference between the nucleon and the Δ -resonance and the strong coupling to the pion-nucleon system, the delta can be also included in a systematic way in chiral EFT. The corresponding chiral effective Lagrangian contains a certain number of parameters, the low-energy constants (LECs). These parameters are fixed by fitting them to experimental data or can be calculated

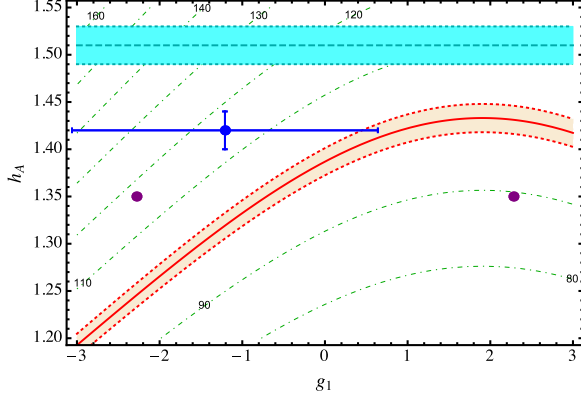


Fig. 87: Value of the pion-nucleon-delta coupling h_A as a function of the pion-delta coupling g_1 represented by the solid red line and the corresponding band given by the dashed red lines. The central line corresponds to $\Gamma_\Delta = 100$ MeV, while the band is obtained by varying Γ_Δ in the range of $98 - 102$ MeV. The dot-dashed lines correspond to various values of the delta width indicated by their values (in MeV). For comparison, the blue dot with error bars represents the real part of the coupling from the recent study of Yao et al., the purple dots stand for the values of the leading order pion-nucleon-delta coupling obtained in the large- N_c limit and the horizontal dashed line with cyan band corresponds to the value (with error represented by the band) from an earlier study of Bernard et al. .

on the lattice, allowing one to predict other quantities. A precise determination of these LECs is an important and highly non-trivial task, especially when the Δ -resonance is included because there are more LECs for a given process than in the pure πN effective Lagrangian.

We have calculated the width of the delta resonance in a systematic expansion in terms of the pion mass and the nucleon-delta mass difference (collectively denoted by q) in the framework of covariant baryon chiral perturbation theory up-to-and-including order q^5 , which includes the leading two-loop contributions. As the main result, we have found for the first time a correlation between the leading pion-nucleon-delta coupling h_A and the lowest-order pion-delta coupling g_1 , see Fig. 87.

Using the same formalism, we have also calculated the width of the Roper resonance at next-to-leading order in a systematic expansion of baryon chiral perturbation theory with pions, nucleons, and the delta and Roper resonances as dynamical degrees of freedom. Three unknown low-energy constants contribute up to the given order. One of them can be fixed by reproducing the empirical value for the width of the Roper decay into a pion and a nucleon. Assuming that the remaining two couplings of the Roper interaction take values equal to those of the nucleon, the

result for the width of the Roper decaying into a nucleon and two pions

$$\Gamma_{R \rightarrow \pi\pi N} = (40.5 \pm 2.2 \pm 16.8) \text{ MeV},$$

is consistent with the experimental value, $\Gamma_{R \rightarrow \pi\pi N} = (66.5 \pm 9.5) \text{ MeV}$.

8.8 What is the X(5568)?

The D0 Collaboration reported the observation of a narrow peak in the $B_s^0 \pi^\pm$ invariant mass distribution based on data from $p\bar{p}$ collisions at $\sqrt{s} = 1.96$ TeV. They fitted to the data using an S -wave Breit-Wigner parametrization, and obtained a mass and width of $M_{X(5568)} = (5567.8 \pm 2.9^{+0.9}_{-1.9}) \text{ MeV}$ and $\Gamma_{X(5568)} = (21.9 \pm 6.4^{+5.0}_{-2.5}) \text{ MeV}$, respectively, with a significance of 5.1σ . This observation has triggered a lot of theoretical calculations and speculations. We have provided arguments based on chiral symmetry and heavy quark symmetry that support the analysis of Burns and Swanson that it is hard to explain the properties of the $X(5568)$ using either tetraquark, hadronic molecule, or threshold-effect models. If the observation of the $X(5568)$ is confirmed, it would have an important impact on the understanding of nonperturbative QCD. We thus suggest to search for it in other processes such as the dipion decays of excited bottom-strange mesons, e.g., $B_{s2}^*(5840) \rightarrow B_s \pi \pi$, and search for its charmed partner using the huge data sets of B factories. As was pointed out later, neither the LHCb nor the CMS Collaboration did see a signal corresponding to the $X(5568)$ based on their pp collision data. Consequently, we have pointed out a possible reason of the appearance of the $X(5568)$ in the D0 and absence in LHCb and CMS experiments. In a semi-exclusive process, one might miss the third particle which is produced together with the $\pi^\pm B_s^0$ simultaneously. In the three-body Dalitz plot, once the remaining region is narrow enough after the kinematic cuts, its reflection to another invariant mass distribution will accumulate a large number of events within a specific energy region. If there is an enhancement in the remaining region, it will make the reflection structure more pronounced. To be specific, we have considered the three exclusive particle process and the specific double heavy baryon loop $\Xi_b^{*+}(5955) \Lambda_b^0(5920) (\Xi_b^0)$, however, the conclusions are more general. The enhancement due to this reflection mechanism is shown for the differential cross section $p\bar{p} \rightarrow \Xi_b^{*+}(5955) \Lambda_b^0(5920) + \text{all} \rightarrow \pi^+ B_s^0 \bar{B}^0 + \text{all}$ in Fig. 88. A combined study of different cone cuts and the low-energy dynamics, e.g. the Landau singularity, demonstrates that the $X(5568)$ structure could come from this kinematic reflection. This conclusion can be checked by both searching for the enhancement in another invariant mass distribution, such as $B_s^0 \bar{B}^0$, and the cone cut dependence of the $X(5568)$ mass. Such a combined study can be used to distinguish the effects of the triangle singularity from a genuine state. We also have shown how

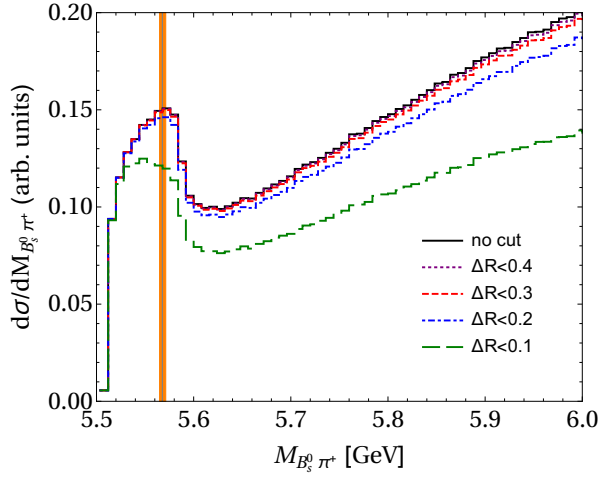


Fig. 88: The differential cross section of the $p\bar{p} \rightarrow \bar{\Xi}_b^{*+}(5955)\Lambda_b^0(5920) + \text{all} \rightarrow \pi^+ B_s^0 \bar{B}^0 + \text{all}$ process as a function of the $\pi^+ B_s^0$ invariant mass distribution with the invariant mass of the three exclusive particles $\pi^+ B_s^0 \bar{B}^0$ at the $\bar{\Xi}_b^{*+}(5955)\Lambda_b^0(5920)$ threshold. The black solid curve is the distribution without cone cut. The purple dotted, red dashed, blue dot-dashed and green long dashed lines are the distributions with cone cut $\Delta R < 0.4$, $\Delta R < 0.3$, $\Delta R < 0.2$ and $\Delta R < 0.1$, respectively. The vertical band is the mass region of the $X(5568)$ measured by the D0 Collaboration.

to avoid this kinematic reflection in future experimental analysis.

8.9 Lineshapes of the $Z_b(10610)$ and the $Z_b(10650)$

In recent years a large number of structures were discovered in production data with either $Q\bar{Q}$ states or $Q\bar{q}-\bar{Q}q$ pairs in the final state close to the thresholds of the latter, where Q (\bar{Q}) and q (\bar{q}) denote a heavy and a light quark (anti-quark), respectively. Examples are the famous $X(3872)$ seen in $J/\psi\pi\pi$, $J/\psi\pi\pi\pi$, $J/\psi\gamma$, $\psi'\gamma$ as well as $D^0\bar{D}^{*0}$ final states, the $Z_b(10610)$ and $Z_b(10650)$ decaying into the $B^{(*)}\bar{B}^*$ open-bottom and $\pi Y(nS)/\pi h_b(mP)$ ($n = 1, 2, 3$, $m = 1, 2$) hidden-bottom channels and their charmed cousins $Z_c(3900)$ and $Z_c(4020)$ seen in the $D^{(*)}\bar{D}^*$ as well as $\pi Q\bar{Q}$ channel. Natural candidates for the nature of those states are tetraquarks (compact bound systems of a heavy-light diquark with heavy-light anti-diquark), hadrocharmonia (compact heavy quarkonia surrounded by a light quark cloud) and hadronic molecules (bound systems of mesons — if the corresponding poles are located very close to the most relevant threshold, these have large radii). In order to understand the nature of those states one crucial aspect is to determine the respective pole locations. This becomes especially clear as soon as one recognizes that hadronic molecules most naturally correspond to poles below the most rele-

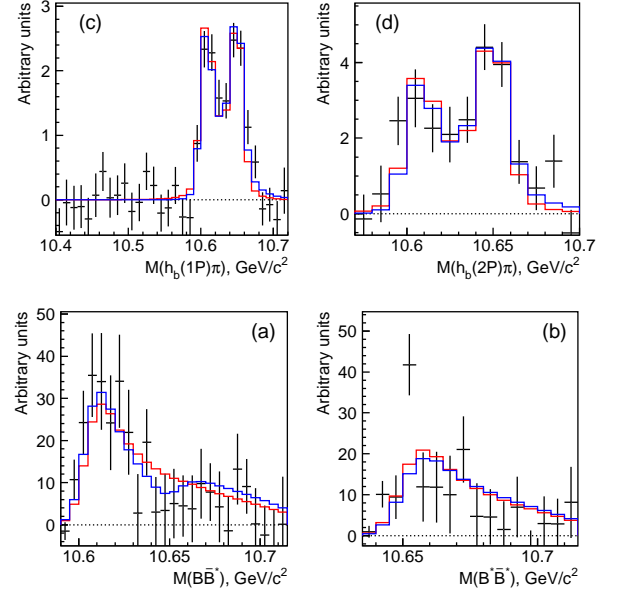


Fig. 89: Lineshapes of the two Z_b -states in the inelastic $h_b\pi$ channels (upper row) and the elastic channels (lower row). The blue line shows the fit with all parameters allowed to float while for the red line various parameters were related to each other by means of heavy quark spin symmetry.

vant threshold — the corresponding two-hadron channel will be called elastic channel in what follows — either on the physical sheet (in analogy to the 3S_1 nucleon–nucleon channel which has the deuteron as bound state pole) or on the unphysical sheet (similar to the 1S_0 nucleon–nucleon channel which shows a huge scattering length, however, no bound state but only a virtual pole).

Standard parametrizations of the existing data for the Z_b -states comprise of the sum of two Breit-Wigners with some complex relative phase. This kind of parametrization necessarily violates unitarity since the two Breit-Wigner distributions strongly overlap, which sheds doubt on the reliability of the resulting mass extraction which puts the poles above the elastic thresholds. In two recent publications we developed and applied an alternative approach to the Z_b -production amplitudes that is consistent with analyticity and unitarity. The method is based on coupled channel unitarity and, after dropping direct $\pi(\bar{Q}Q) \rightarrow \pi(\bar{Q}Q)$ transitions on the potential level — a step well justified from chiral perturbation theory as well as phenomenology — the equations can be solved analytically.

We performed two different fits both compared to data in Fig. 89: The blue line is based on a 11 parameter fit — since a good fit (fit probability: 53%) was achieved already without inclusion of explicit pole terms they were omitted in the whole analysis. It reveals that both the pole of $Z_b(10610)$ as well as the one for $Z_b(10650)$ are located on the unphysical sheet for $B\bar{B}^*$ and $B^*\bar{B}^*$, respectively. This observation already implies that both states must be

of molecular origin. In a second fit we imposed spin symmetry where ever possible. This reduced the number of parameters to 8 but did not worsen the fit significantly (fit probability 48%). In the latter case the potential gets arranged such that in addition to the heavy quark spin also the light quark spin gets conserved which might point at an additional symmetry of the heavy quark system as recently conjectured by Voloshin. Even more importantly also from this analysis both Z_b poles are located below threshold on the unphysical sheets with high statistical significance providing additional strong evidence for a molecular nature of $Z_b(10610)$ and $Z_b(10650)$.

A Councils

A.1 CBAC – COSY Beam Time Advisory Committee

Prof. K. Aulenbacher	Universität Mainz, Germany
Prof. A. Chao	SLAC Stanford, USA
Prof. O. Kester	TRIUMF, Canada
Prof. C.J. Schmidt	GSI Darmstadt, Germany
Prof. E. Steffens	Universität Erlangen-Nürnberg, Germany (Chairperson)
Prof. G. Trubnikov	JINR Dubna, Russia
Prof. M. Weber	KIT, Karlsruhe, Germany

Note: In the committee of Forschungszentrum Jülich, the “Wissenschaftlicher Beirat” (WB, Scientific Council), Prof. Thomas Roser (Brookhaven National Laboratory, USA) is assigned to IKP.

B Publications–Journal Articles

1. **Search for an Isospin $I=3$ Dibaryon**
P. Adlarson *et al.*
Phys. Lett. B **762** 455-461 (2016)
2. **Measurements of branching ratios for η decays into charged particles**
P. Adlarson *et al.*
Phys. Rev. C **94** 065206 (2016)
3. **Measurement of the $\vec{\pi} p \rightarrow d\pi^0\pi^0$ reaction with polarized beam in the region of the $d^*(2380)$ resonance**
P. Adlarson *et al.*
Eur. Phys. J. A **52** 147 (2016)
4. **The $B \rightarrow K^*$ form factors on the lattice**
A. Agadjanov *et al.*
Nucl. Phys. B **910** 387 - 409 (2016)
5. **The optical potential on the lattice**
D. Agadjanov *et al.*
J. High Energ. Phys. **2016** 43 (2016)
6. **A search for low-energy neutrino and antineutrino signals correlated with gamma-ray bursts with Borexino**
M. Agostini *et al.*
Astropart. Phys. **6** 1-10 (2016)
7. **Neutrino physics with JUNO**
F. An *et al.*
J. Phys. G **43** 030401 - (2016)
8. **A storage ring experiment to detect a proton electric dipole moment**
V. Anastassopoulos *et al.*
Rev. Sci. Instrum. **87** 115116 - (2016)
9. **T and F asymmetries in π^0 photoproduction on the proton**
J.R.M. Annand *et al.*
Phys. Rev. C **93** 055209 (2016)
10. **Threshold pion production in proton-proton collisions at NNLO in chiral EFT**
V. Baru *et al.*
Eur. Phys. J. A **52** 146 (2016)
11. **Heavy-quark spin symmetry partners of the X(3872) revisited**
V. Baru *et al.*
Phys. Lett. B **763** 20 - 28 (2016)
12. **Two-nucleon scattering in a modified Weinberg approach with a symmetry-preserving regularization**
J. Behrendt *et al.*
Eur. Phys. J. A **52** 296 (2016)
13. **Few-nucleon systems with state-of-the-art chiral nucleon-nucleon forces-**
S. Binder *et al.*
Phys. Rev. C **93** 044002 (2016)
14. **Effect of Z_b states on $\Upsilon(3S) \rightarrow \Upsilon(1S)\pi\pi$ decays**
Y. Chen *et al.*
Phys. Rev. D **93** 034030 (2016)
15. **On the pole content of coupled channels chiral approaches used for the $\bar{K}N$ system**
A. Cieplý *et al.*
Nucl. Phys. A **954** 17 - 40 (2016)
16. **Pion polarizabilities from a $\gamma\gamma \rightarrow \pi\pi$ analysis**
L. Dai and M.R. Pennington
Phys. Rev. D **94** 116021 (2016)

17. **A model-independent analysis of final-state interactions in $\bar{B}_{d/s}^0 \rightarrow J/\psi\pi\pi$**
J.T. Daub, C. Hanhart and B. Kubis
J. High Energ. Phys. **2016** 9 (2016)
18. **Violations of discrete space-time symmetries in chiral effective field theory**
J. de Vries and U. Meißner
Int. J. Mod. Phys. E **25** 1641008 (2016)
19. **Subtraction of power counting breaking terms in chiral perturbation theory: spinless matter fields**
M. Du, F. Guo and U. Meißner
J. High Energ. Phys. **2016** 122 (2016)
20. **Aspects of the low-energy constants in the chiral Lagrangian for charmed mesons**
M. Du *et al.*
Phys. Rev. D **94** 094037 (2016)
21. **P -wave coupled channel effects in electron-positron annihilation**
M. Du, U. Meißner and Q. Wang
Phys. Rev. D **94** 096006 (2016)
22. **Coherent pion production in proton-deuteron collisions**
S. Dymov *et al.*
Phys. Lett. B **762** 102 - 106 (2016)
23. **Nucleon-deuteron scattering using the adiabatic projection method**
S. Elhatisari *et al.*
Eur. Phys. J. A **52** 174 (2016)
24. **Nuclear Binding Near a Quantum Phase Transition**
S. Elhatisari *et al.*
Phys. Rev. Lett. **117** 132501 (2016)
25. **Electron-cooled accumulation of 4×10^9 positrons for production and storage of antihydrogen atoms**
D.W. Fitzakerley *et al.*
J. Phys. B **49** 064001 - (2016)
26. **Momentum dependence of the imaginary part of the ω - and η' -nucleus optical potential**
S. Friedrich *et al.*
Eur. Phys. J. A **52** 297 (2016)
27. **The width of the Δ -resonance at two loop order in baryon chiral perturbation theory**
J. Gegelia *et al.*
Phys. Lett. B **763** 1 - 8 (2016)
28. **The width of the Roper resonance in baryon chiral perturbation theory**
J. Gegelia, U. Meißner and D. Yao
Phys. Lett. B **760** 736 - 741 (2016)
29. **Muon capture on ^3H**
J. Golak *et al.*
Phys. Rev. C **94** 034002 (2016)
30. **Remarks on a Johann spectrometer for exotic-atom research and more**
D. Gotta and L.M. Simons
Spectrochim. Acta, Part B **120** 9 - 18 (2016)
31. **How to Reach a Thousand-Second in-Plane Polarization Lifetime with 0.97 - GeV / c Deuterons in a Storage Ring**
G. Guidoboni *et al.*
Phys. Rev. Lett. **117** 054801 (2016)
32. **Interplay of quark and meson degrees of freedom in near-threshold states: A practical parametrization for line shapes**
F. Guo *et al.*
Phys. Rev. D **93** 074031 (2016)

33. **Remarks on the Pc structures and triangle singularities**
F. Guo *et al.*
Eur. Phys. J. A **52** 318 (2016)
34. **Hindered magnetic dipole transitions between P-wave bottomonia and coupled-channel effects**
F. Guo, U. Meißner and Z. Yang
Phys. Lett. B **760** 417 - 421 (2016)
35. **How the X (5568) Challenges Our Understanding of QCD**
F. Guo, U. Meißner and B. Zou
Commun. Theor. Phys. **65** 593 - 595 (2016)
36. **The electromagnetic form factors of the Λ in the timelike region**
J. Haidenbauer and U. Meißner
Phys. Lett. B **761** 456 - 461 (2016)
37. **Strangeness $S=-2$ baryon-baryon interaction at next-to-leading order in chiral effective field theory**
J. Haidenbauer, U. Meißner and S. Petschauer
Nucl. Phys. A **954** 273 - 293 (2016)
38. **Remarks on meson loop effects on quark models**
I. Hammer, C. Hanhart and A.V. Nefediev
Eur. Phys. J. A **52** 330 (2016)
39. **Potential of geo-neutrino measurements at JUNO**
R. Han *et al.*
Chinese Phys. C **40** 033003 (2016)
40. **Measurement of polarization observables of the associated strangeness production in proton proton interactions**
F. Hauenstein *et al.*
Eur. Phys. J. A **52** 337 (2016)
41. **Extracting the depolarization coefficient DNN from data measured with a full acceptance detector**
F. Hauenstein *et al.*
Nucl. Instr. Meth. Phys. Res. A **817** 42 - 45 (2016)
42. **On the $\pi\pi$ continuum in the nucleon form factors and the proton radius puzzle**
M. Hoferichter *et al.*
Eur. Phys. J. A **52** 331 (2016)
43. **Remarks on the pion-nucleon σ -term**
M. Hoferichter *et al.*
Phys. Lett. B **760** 74 - 78 (2016)
44. **Roy-Steiner-equation analysis of pion-nucleon scattering**
M. Hoferichter *et al.*
Phys. Rep. **625** 1 - 88 (2016)
45. **Multipole neodymium magnets for polarized atom source**
K.A. Ivshin *et al.*
Izv. Vyssh. Uchebn. Zaved., Priborostr. **59** 60 - 68 (2016)
46. **K_{α} X-ray emission in manganese compounds**
M. Jabua *et al.*
Spectrochim. Acta, Part B **121** 11 - 17 (2016)
47. **High-precision measurement of the associated strangeness production in proton-proton interactions**
S. Jowzaee *et al.*
Eur. Phys. J. A **52** 7 (2016)
48. **Photoproduction of η π pairs off nucleons and deuterons**
A. Käser *et al.*
Eur. Phys. J. A **52** 272 (2016)

49. **Late Pseudoprogession in Glioblastoma: Diagnostic Value of Dynamic O-(2-[¹⁸F]fluoroethyl)-L-Tyrosine PET**
S. Kebir *et al.*
Clin. Cancer Res. **22** 2190 - 2196 (2016)
50. **Evidence for excitation of two resonance states in the isovector two-baryon system with a mass of 2.2 GeV/ c²**
V. Komarov *et al.*
Phys. Rev. C **93** 065206 (2016)
51. **Applying Twisted Boundary Conditions for Few-body Nuclear Systems**
C. Körber and T. Luu
Phys. Rev. C **93** 054002 (2016)
52. **Jacobi no-core shell model for p-shell nuclei-110**
S. Liebig, U. Meißner and A. Nogga
Eur. Phys. J. A **52** 103 (2016)
53. **Precise determination of lattice phase shifts and mixing angles**
B. Lu *et al.*
Phys. Lett. B **760** 309 - 313 (2016)
54. **Experimental data on solar neutrinos**
L. Ludhova
Eur. Phys. J. A **52** 82 (2016)
55. **Resonances in QCD**
M.F.M. Lutz *et al.*
Nucl. Phys. A **948** 93 - 105 (2016)
56. **Quantum Monte Carlo calculations for carbon nanotubes**
T. Luu and T. Lähde
Phys. Rev. B: Condens. Matter **93** 155106 (2016)
57. **Large numbers of cold positronium atoms created in laser-selected Rydberg states using resonant charge exchange**
R. McConnell *et al.*
J. Phys. B **49** 064002 (2016)
58. **Measurement of the absolute differential cross section of proton-proton elastic scattering at small angles**
D. Mchedlishvili *et al.*
Phys. Lett. B **755** 92 - 96 (2016)
59. **Determination of the real part of the η' -Nb optical potential**
M. Nanova *et al.*
Phys. Rev. C: Nucl. Phys. **94** 025205 (2016)
60. **Review of Particle Physics**
C. Patrignani *et al.*
Chinese Phys. C **40** 100001 (2016)
61. **Hyperons in nuclear matter from SU(3) chiral effective field theory**
S. Petschauer *et al.*
Eur. Phys. J. A **52** 15 (2016)
62. **Leading three-baryon forces from SU(3) chiral effective field theory**
S. Petschauer *et al.*
Phys. Rev. C **93** 014001 (2016)
63. **A time-based front-end ASIC for the silicon micro strip sensors of the PANDA Micro Vertex Detector**
V.D. Pietro *et al.*
J. Instrum. **11** C03017 - C03017 (2016)
64. **Laser spectroscopy of muonic deuterium**
R. Pohl *et al.*
Science **353** 669 - 673 (2016)

65. **First measurement of the helicity asymmetry E in η photoproduction on the proton**
I. Senderovich *et al.*
Phys. Lett. B **755** 64-69 (2016)
66. **Ranking and validation of the spallation models for description of intermediate mass fragment emission from $p + Ag$ collisions at 480 MeV incident proton beam energy**
S.K. Sharma *et al.*
Eur. Phys. J. A **52** 171 (2016)
67. **Elastic pion-nucleon scattering in chiral perturbation theory: A fresh look**
D. Siemens *et al.*
Phys. Rev. C **94** 014620 (2016)
68. **Study of doubly strange systems using stored antiprotons**
B. Singh *et al.*
Nucl. Phys. A **954** 323 - 340 (2016)
69. **Feasibility studies of time-like proton electromagnetic form factors at \bar{P} ANDA at FAIR**
B. Singh *et al.*
Eur. Phys. J. A **52** 325 (2016)
70. **Testing semilocal chiral two-nucleon interaction in selected electroweak processes**
R. Skibiński *et al.*
Phys. Rev. C **93** 064002 (2016)
71. **Electromagnetic Simulation and Design of a Novel Waveguide RF Wien Filter for Electric Dipole Moment Measurements of Protons and Deuterons**
J. Slim *et al.*
Nucl. Instr. Meth. Phys. Res. A **828** 116 - 124 (2016)
72. **Measurement of the charged pion mass using X-ray spectroscopy of exotic atoms**
M. Trassinelli *et al.*
Phys. Lett. B **759** 583 - 588 (2016)
73. **Application of an extended random-phase approximation to giant resonances in light-, medium-, and heavy-mass nuclei**
V. Tselyaev *et al.*
Phys. Rev. C **94** 034306 (2016)
74. **Empirical parametrization of the nucleon-nucleon elastic scattering amplitude at high beam momenta for Glauber calculations and Monte Carlo simulations**
V. Uzhinsky *et al.*
Phys. Rev. C **94** 064003 (2016)
75. **Polarized proton-deuteron scattering as a test of time-reversal invariance**
Y.N. Uzikov and J. Haidenbauer
Phys. Rev. C **94** 035501 (2016)
76. **Role of the Total Isospin 3/2 Component in Three-Nucleon Reactions**
H. Witala *et al.*
Few-body systems **57** 1213 - 1225 (2016)
77. **Insight into the Narrow Structure in η Photoproduction on the Neutron from Helicity-Dependent Cross Sections**
L. Witthauer *et al.*
Phys. Rev. Lett. **117** 132502 (2016)
78. **Pion-nucleon scattering in covariant baryon chiral perturbation theory with explicit Delta resonances**
D. Yao *et al.*
J. High Energ. Phys. **2016** 38 (2016)

C Talks and Colloquia

C.1 Conference and workshop contributions

1. P. Alba *et al.*
Workshop on Excited Hyperons in QCD Thermodynamics at Freeze-Out (YSTAR2016) Mini-Proceedings
YSTAR2016 Workshop, Newport News, USA: 2016-11-16 - 2016-11-17
2. D. Alfs *et al.*
Status of the analysis for the search of polarization in the antiproton production process
MESON 2016 - 14th International Workshop on Meson Production, Properties and Interaction, Krakau, Poland: 2016-06-02 - 2016-06-07
Eur. Phys. J. Web of Conferences 130 07002
3. A. Apostolou *et al.*
Measurement of the spatial and energy-loss resolution with a prototype Straw Tube Tracker (STT) for the PANDA experiment
DPG Frühjahrstagung, Darmstadt, Germany: 2016-03-14 - 2016-03-18
4. V. Baru *et al.*
Light-quark mass behaviour of the X(3872) as a molecular state
21st International Conference on Few-Body Problems in Physics (FB21), Chicago, USA: 2015-05-18 - 2015-05-22
Eur. Phys. J. Web of Conferences 113 05015
5. V. Baru *et al.*
Chiral extrapolation of the X(3872) binding energy
1st International Conference on Particle Physics and Astrophysics (ICPPA 2015), Moskow, Russia: 2015-10-05 - 2015-10-10
J. Phys.: Conf. Ser. 675 022017
6. L. Bianchi *et al.*
Parallel Algorithms for Online Trackfinding at PANDA
DPG Frühjahrstagung, Darmstadt, Germany: 2016-03-14 - 2016-03-18
7. L. Bianchi *et al.*
Parallel Algorithms for Online Trackfinding for the PANDA Experiment at FAIR
607. WE-Heraeus-Seminar on "Semiconductor detectors in astronomy, medicine, particle physics and photon science", Bad Honnef, Germany: 2016-02-14 - 2016-02-17
8. L. Bianchi *et al.*
Parallel Algorithms for Online Trackfinding for the PANDA Experiment at FAIR
Fünftes Doktorandenkolloquium, Ruhr-Universität Bochum, Germany: 2016-06-14 - 2016-06-14
9. L. Bianchi *et al.*
Parallel Algorithms for Online Trackfinding at PANDA
22nd International Conference on Computing in High Energy and Nuclear Physics, CHEP 2016, San Francisco, USA: 2016-10-10 - 2016-10-14
10. C. Böhme *et al.*
Studies for a BPM Upgrade at COSY
4th International Beam Instrumentation Conference, Melbourne, Australia: 2015-09-13 - 2015-09-17

11. C. Böhme, A. Halama and V. Kamedzhiev
COSY BPM Electronics Upgrade
 International Beam Instrumentation Conference, Barcelona, Spain: 2016-09-11 - 2016-09-15

12. C. Böhme *et al.*
Beam Diagnostics for the High Energy Storage Ring at FAIR
 4th International Beam Instrumentation Conference, Melbourne, Australia: 2015-09-13 - 2015-09-17

13. A. Caminata *et al.*
The SOX experiment: understanding the detector behavior using calibration sources
 Magellan Workshop, Hamburg, Germany: 2016-03-17 - 2016-03-18

14. A. Caminata *et al.*
Monte Carlo simulations in neutrino physics: the example of the SOX experiment
 Magellan Workshop, Hamburg, Germany: 2016-03-17 - 2016-03-18

15. L. Cao
Simulations of the Simulation of the $D_s \rightarrow \eta_e \nu_e$ Form Factor
 PANDA LVII. Collaboration Meeting, GSI Darmstadt, Germany: 2016-06-06 - 2016-06-09

16. L. Cao and J. Ritman
Simulated Measurement of the D_s Meson Semileptonic Decay Form Factor with the $\bar{\text{P}}\text{ANDA}$ Detector
 37th International Conference on High Energy Physics (ICHEP 2014), Valencia, Spain: 2014-07-02 - 2014-07-09
 Nucl. Part. Phys. Proc. 273-275 2485 - 2487

17. L. Cao, T. Stockmanns and J. Ritman
Simulations of the Measurement of the Form Factor for the D_s Semileptonic Decay with the $\bar{\text{P}}\text{ANDA}$ Detector
 DPG Frühjahrstagung, Darmstadt, Germany: 2016-03-14 - 2016-03-18

18. C. Constantinou
Dense Matter in Supernovae and Compact Objects
 QCD matter: dense and hot, International Workshop XLIV on Gross Properties of Nuclei and Nuclear Excitations, Hirschegg, Austria: 2016-01-17 - 2016-01-23

19. R.W. Engels
Polarized Molecules: A new Option for Internal Storage-Cell Targets?
 XVIth International Workshop on Polarized Sources, Targets, and Polarimetry, Bochum, Germany: 2015-09-14 - 2015-09-18

20. R.W. Engels
Polarized Molecules
 Seventh Georgian-German School and Workshop in Basic Science, Tbilisi, Georgien: 2016-08-28 - 2016-09-02

21. R.W. Engels and G. Ciullo
Polarized Fusion. Can Polarization Help to Increase the Energy Output of Fusion Reactors?
 The 21st International Symposium on Spin Physics, Beijing, China: 2014-10-20 - 2014-10-24
 Int. J. Mod. Phys. Conf. Ser. 40 1660112 -

22. I. Engin *et al.*
A polarized ^3He Target for the Exploration of Spin Effects in Laser-induced Plasmas
 PolFusion (Round-Table on perspectives and milestones on nuclear fusion with polarized fuels), Ferrara, Italy:
 2015-07-23 - 2015-07-23

23. A.M. Gasparyan *et al.*
Nucleon-nucleon scattering in the $^1\text{S}_0$ partial wave in the modified Weinberg approach
 21st International Conference on Few-Body Problems in Physics (FB21), Chicago, USA: 2015-05-18 - 2015-05-22
 Eur. Phys. J. Web of Conferences 113 04024

24. A. Gillitzer
Spectroscopy of Strange Baryons: Future Perspectives
 Baryons 2016 - International Conference on the Structure of Baryons, Florida State University Alumni Center,
 Tallahassee, USA: 2016-05-16 - 2016-05-20

25. J. Golak *et al.*
Break-up channels in muon capture on ^3He
 21st International Conference on Few-Body Problems in Physics, Chicago, USA: 2015-05-18 - 2015-05-22
 Eur. Phys. J. Web of Conferences 113 04029

26. D. Gotta
From fundamental physics to applications
 Seventh Georgian-German School and Workshop in Basic Science, Tbilisi, Georgien: 2016-08-29 - 2016-09-01

27. D. Gotta
Experimental status and prospects of light pionic atoms
 First Workshop on Hadronic Contributions to New Physics, Puerto de la Cruz, Tenerife: 2016-09-26 - 2016-09-30

28. J. Haidenbauer
Hyperons in nuclear matter studied in chiral effective field theory
 8th International Workshop on Chiral Dynamics, Pisa, Italy: 2015-06-29 - 2015-07-03

29. J. Haidenbauer
Charm production in antiproton-proton collisions
 Panda Collaboration Meeting, Darmstadt, Germany: 2016-06-06 - 2016-06-09

30. J. Haidenbauer
Production of charmed baryons and mesons in antiproton-proton annihilation
 VIII International Workshop on Charm Physics, Bologna, Italy: 2016-09-05 - 2016-09-09

31. A. Halama *et al.*
Numerical Comparative Study of BPM Designs for the HESR at FAIR
 International Beam Instrumentation Conference, Barcelona, Spain: 2016-09-11 - 2016-09-15

32. C. Hanhart
Practical Parametrization for Line Shapes of Near-Threshold States
 International Workshop on Heavy Quarkonium, Richmond, USA: 2016-06-06 - 2016-06-10

33. C. Hanhart
Practical Parametrization for Line Shapes of Near-Threshold States
 11th International Workshop on Heavy Quarkonium, Pacific Northwest National Laboratory (PNNL), USA:
 2016-06-06 - 2016-06-10
34. F. Hauenstein
Polarization Observables Measured in the Reaction $\vec{p}p \rightarrow pK^+\Lambda$ by COSY-TOF
 DPG Frühjahrstagung, Darmstadt, Germany: 2016-03-14 - 2016-03-18
35. F. Hauenstein
Determination of the Spin Triplet $p\Lambda$ Scattering Length from the Reaction $\vec{p}p \rightarrow pK^+\Lambda$
 Baryons 2016 - International Conference on the Structure of Baryons, Florida State University Alumni Center,
 Tallahassee, USA: 2016-05-16 - 2016-05-20
36. N. Hempelmann
Stabilization of the Deuteron Spin Tune in a Storage Ring Using Active Feedback
 22nd International Spin Symposium, Champaign, USA: 2016-09-25 - 2016-09-30
37. J. Hetzel *et al.*
Towards Beam-Dynamics Simulations Including More Realistic Field Descriptions for the HESR
 7th International Particle Accelerator Conference, Busan, Korea: 2016-05-09 - 2016-05-13
38. Q. Hu
Measurements of Proton-Proton Elastic Scattering by the KOALA Experiment at COSY
 DPG Frühjahrstagung, Darmstadt, Germany: 2016-03-14 - 2016-03-18
39. M. Jabua, D. Gotta and T. Strauch
Comparison of the LY23 line shape of Ba²⁺ compounds and metal
 Frühjahrstagung DGP Atomphysik (A), Hannover, Germany: 2016-02-29 - 2016-03-04
40. D. Ji *et al.*
First Experience of Applying Loco for Optics at Cosy
 7th International Particle Accelerator Conference, Busan, Korea: 2016-05-08 - 2016-05-13
41. V. Kamedzhiev *et al.*
Electron cooling experiments at COSY
 Workshop on electron cooling and stochastic cooling, Tokyo, Japan: 2016-10-04 - 2016-10-10
42. I. Keshelashvili
Polarimetry concept based on heavy crystal hadron calorimeter
 CALOR 2016 - The 17th Int. Conf. on Calorimetry in Particle Physics, Daegu, Rep. of Korea: May 15 - 20, 2016
43. M.C. Kunkel
Light Meson Decays in CLAS and CLAS12
 DPG Frühjahrstagung, Darmstadt, Germany: 2016-03-14 - 2016-03-18
44. M.C. Kunkel
Light meson decays from photon-induced reactions with CLAS
 XVITH INTERNATIONAL CONFERENCE ON HADRON SPECTROSCOPY: Hadron2015, Newport News,
 VA: 2015-09-13 - 2015-09-18
 AIP Conf. Proc. 1735 030017

45. M.C. Kunkel
[Light meson decays from photon-induced reactions with CLAS](#)
14th International Workshop on Meson Production, Properties and Interaction, Krakau, Poland: 2016-06-02 - 2016-06-07
Eur. Phys. J. Web of Conferences 130 04004
46. M.C. Kunkel
[Measurement of the \$\pi^0\$ differential cross-section with CLAS and outlook into 12 GeV Hall C](#)
XVITH INTERNATIONAL CONFERENCE ON HADRON SPECTROSCOPY: Hadron2015, Newport News, VA: 2015-09-13 - 2015-09-18
AIP Conf. Proc. 1735 080013
47. M.C. Kunkel
[An update on the Electromagnetic Transition Form Factor of the eta' meson with g12 and CLAS12](#)
CLAS Collaboration Meeting, Jefferson Lab, Newport News, USA: 2016-02-23 - 2016-02-26
48. M.C. Kunkel
[G12 Run Group review G12 analysis status](#)
CLAS Collaboration Meeting, Jefferson Lab, Newport News, USA: 2016-02-23 - 2016-02-26
49. M.C. Kunkel
[Light meson decays in CLAS and CLAS12](#)
MESON 2016 - 14th International Workshop on Meson Production, Properties and Interaction, Krakau, Poland: 2016-06-02 - 2016-06-07
50. M.C. Kunkel
[Transition Form Factors of the eta' and phi Mesons with CLAS12](#)
PAC Talk - CLAS Collaboration Meeting, Jefferson Lab, Newport News, USA: 2016-06-15 - 2016-06-18
51. A. Lai
[A Test System for the Electronics Components of the PANDA MVD](#)
Wilhelm and Else Heraeus-Seminar on Semiconductor Detector, Bad Honnef, Germany: 2016-02-14 - 2016-02-17
52. A. Lai
[A Test System for the Electronics Components of the PANDA MVD](#)
Doktorandenkolloquium, Bochum, Germany: 2016-06-14 - 2016-06-14
53. A. Lai
[A Test System for the Electronics Components of the PANDA MVD](#)
DPG Frühjahrstagung, Darmstadt, Germany: 2016-03-14 - 2016-03-18
54. A. Lehrach
[Storage Ring Based EDM Search – Achievements and Goals](#)
21st International Symposium on Spin Physics, Beijing, China: 2014-09-29 - 2014-10-03
Int. J. Mod. Phys. Conf. Ser. 40 1660092
55. A. Lehrach
[Highlights from COSY \(JEDI project\)](#)
7th Georgian-German School and Workshop in Basic Science, Tbilisi, Gorgia: 2016-08-28 - 2016-08-31

56. D. Lersch
Study of η -Meson Decays with the WASA-at-COSY experiment
 DPG Frühjahrstagung, Darmstadt, Germany: 2016-03-14 - 2016-03-18
57. D. Lersch
Investigation of the CLAS g12 kinematic fitter
 CLAS Collaboration Meeting, Jefferson Lab, Newport News, USA: 2016-06-15 - 2016-06-18
58. D. Lersch
Status of the analysis of $\eta \rightarrow \pi^+ \pi^- \pi^0$ with the CLAS g12 data set
 CLAS Collaboration Meeting, Jefferson Lab, Newport News, USA: 2016-06-15 - 2016-06-18
59. D. Lersch
Status of the Analysis of $\eta \rightarrow \pi^+ \pi^- \pi^0$ with the CLAS g12 Data Set - Vol. II
 CLAS Collaboration Meeting, Jefferson Lab, Newport News, USA: 2016-11-01 - 2016-11-04
60. D. Lersch
Radiative and Hadronic Decay Modes of the eta-Meson with CLAS and WASA-at-COSY
 Baryons 2016 - International Conference on the Structure of Baryons, Florida State University Alumni Center, Tallahassee, USA: 2016-05-16 - 2016-05-20
61. D. Lersch
Studying η -Meson Decays with WASA-at-COSY
 MESON 2016 - 14th International Workshop on Meson Production, Properties and Interaction, Kraków, Poland: 2016-06-02 - 2016-06-07
 Eur. Phys. J. Web of Conferences 130 03005
62. S. Lu *et al.*
Study of $N\Sigma$ Cusp in $p + p \rightarrow p + K^+ + \Lambda$ with Partial Wave Analysis
 DPG Frühjahrstagung, Darmstadt, Germany: 2016-03-14 - 2016-03-18
63. L. Ludhova
Low-energy neutrinos
 Topics in Astroparticle and underground Physics, Torino, Italy: 2015-09-07 - 2015-09-11
 J. Phys.: Conf. Ser. 718 022012
64. L. Ludhova
Geoneutrinos
 GDR Neutrino 2016, Grenoble, France: 2016-06-06 - 2016-06-07
65. L. Ludhova
Neutrino Geoscience
 Magellan Workshop - Connecting Neutrino Physics and Astronomy, Hamburg, Germany: 2016-03-17 - 2016-03-18
66. L. Ludhova
Status and Future of Neutrino Physics with Scintillator-Based Detectors
 DPG Frühjahrstagung, Darmstadt, Germany: 2016-03-14 - 2016-03-18
67. L. Ludhova
Neutrino Geoscience
 Magellan Workshop, Hamburg, Germany: 2016-03-17 - 2016-03-18

68. L. Ludhova
JUNO
 FroST - Topical Workshop for THEIA, Mainz, Germany: 2016-10-22 - 2016-10-24
69. L. Ludhova
Geoneutrinos
 XXXVI Physics in Collision, XIIth Rencontres du Vietnam, Quy Nhon, Vietnam: 2016-09-13 - 2016-09-18
70. L. Ludhova
“Neutrino physics based on Scintillator Detectors“
 7th Georgian-German School and Workshop, Tbilisi, Georgia: 2016-08-30 - 2016-08-30
71. S. Marcocci *et al.*
Measurement of solar neutrino fluxes with Borexino
 Magellan Workshop, Hamburg, Germany: 2016-03-17 - 2016-03-18
72. P. Maris *et al.*
Properties of ^4He and ^6Li with improved chiral EFT interactions
 21st International Conference on Few-Body Problems in Physics, Chicago, USA: 2015-05-18 - 2015-05-22
 Eur. Phys. J. Web of Conferences 113 04015
73. U.-G. Meißner
Strong interaction theory
 1st IAS Symposium, Forschungszentrum Jülich, Jülich, Germany: 2016-12-05 - 2016-12-06
74. U.-G. Meißner, T. Lähde and T. Luu
Pushing the Boundaries of Nuclear Physics with Lattice Simulations
 NIC Symposium 2016, Jülich, Germany: 2016-02-11 - 2016-02-12
75. U.-G. Meißner
Pentaquarks from threshold singularities
 Workshop on “The power of spectroscopy in QCD, ECT*, Trento, Italy: 2016-02-07 - 2016-02-13
76. U.-G. Meißner
Clustering in nuclear physics from ab initio nuclear lattice simulations
 KITPC program “Clustering effects of nucleons in nuclei and quarks in multi-quark states,” Kavli Institute for Theoretical Physics, CAS, Beijing, China: 2016-03-28 - 2016-04-22
77. U.-G. Meißner
Towards an understanding of clustering in nuclei
 INT Program 16-1on Nuclear Physics from Lattice QCD, INT, Seattle, USA: 2016-03-21 - 2016-05-27
78. U.-G. Meißner
Theory of the neutron EDM
 Workshop on “Baryons over antibaryons: the nuclear physics of Sakharov,” ECT*, Trento, Italy: 2016-07-25 - 2016-07-25
79. U.-G. Meißner
Hadronic Parity Violation in Chiral EFT
 mini-workshop on “Hadronic weak physics and new physics with medium energy nucleon beams,” ITP, CAS, Beijing, China: 2016-09-20 - 2016-09-21

80. U.-G. Meißner
[Nuclear Structure and Reactions from Nuclear Lattice EFT](#)
 Workshop on Covariant Density Functional Theory for Nuclear Structure, Peking University, Beijing, China:
 2016-09-19 - 2016-09-22
81. F. Müller
[LYSO Crystal Testing for an EDM Polarimeter](#)
 CALOR 2016 - The 17th International Conference on Calorimetry in Particle Physics, Daegu, Republic of Korea:
 May 15 - 20, 2016
82. R. Navarro Pérez *et al.*
[Binding in light nuclei: Statistical NN uncertainties vs Computational accuracy](#)
 Workshop for young scientists with research interests focused on physics at FAIR, Garmisch-Partenkirchen,
 Germany: 2016-02-14 - 2016-02-19
 J. Phys.: Conf. Ser. 742 012001
83. S. Petschauer *et al.*
[Hyperons in nuclear matter from SU\(3\) chiral effective field theory](#)
 DPG-Frühjahrstagung, Darmstadt, Germany: 2016-03-14 - 2016-03-18
84. E. Prencipe
[Customization of GENFIT2 fitting package for PANDA](#)
 "Connecting the dots 2016" Workshop, Vienna, Austria: 2016-02-22 - 2016-02-24
85. E. Prencipe
[Software design of GENFIT2](#)
 Common Tracking forum, Vienna, Austria: 2016-02-23 - 2016-02-23
86. E. Prencipe
[Impact of the genfit 2 Kalman-Filter based algorithm on physics simulations performed with Panda Root](#)
 DPG-Frühjahrstagung, Darmstadt, Germany: 2016-03-14 - 2016-03-18
87. E. Prencipe
[X, Y, Z rates with PANDA at FAIR](#)
 DPG Frühjahrstagung, Darmstadt, Germany: 2016-03-14 - 2016-03-18
88. E. Prencipe
[Feasibility study of the \$\bar{p}p \rightarrow D_s^- D_{s0}^*\(2317\)\$ process with PANDA](#)
 DPG Frühjahrstagung, Darmstadt, Germany: 2016-03-14 - 2016-03-18
89. E. Prencipe
[Customization of the GENFIT2 Fitting Package in \$\bar{\text{P}}\text{ANDA}\$](#)
 Connecting the dots 2016, Vienna, Austria: 2016-02-22 - 2016-02-24
 Eur. Phys. J. Web of Conferences 127 00013
90. E. Prencipe, J.S. Lange and A. Blinov
[New spectroscopy with PANDA at FAIR: X, Y, Z and the F-wave charmonium states](#)
 XVITH INTERNATIONAL CONFERENCE ON HADRON SPECTROSCOPY: Hadron2015, Newport News,
 USA: 2015-09-13 - 2015-09-18

91. E. Prencipe and PANDA-Collaboration
Status and Perspectives for PANDA at FAIR
 37th International Conference on High Energy Physics (ICHEP), Valencia, Spain: 2014-07-02 - 2014-07-09
 Nucl. Part. Phys. Proc. 273-275 231 - 237

92. J. Pütz
Study of excited Ξ Baryons in Antiproton-Proton Collisions with the PANDA Detector
 FAIRNESS2016, Garmisch-Partenkirchen, Germany: 2016-02-14 - 2016-02-19

93. J. Pütz
Study of excited Ξ Baryons in Antiproton-Proton Collisions with the PANDA Detector
 DPG Frühjahrstagung, Darmstadt, Germany: 2016-03-14 - 2016-03-18

94. J. Pütz *et al.*
Study of Excited Ξ Baryons in $\bar{p}p$ -Collisions with the PANDA Detector
 FAIRNESS 2016, Garmisch-Partenkirchen, Germany: 2016-02-14 - 2016-02-19
 J. Phys.: Conf. Ser. 742 012028 -

95. A. Riccardi *et al.*
The PASTA chip for the silicon micro strip sensor of the PANDA MVD
 DPG Frühjahrstagung, Darmstadt, Germany: 2016-03-14 - 2016-03-18

96. J. Ritman
Initial Measurements of Hadron Spectroscopy and Nucleon Structure with Antiprotons by PANDA
 COMPASS Beyond 2020 Workshop, CERN, Genf, Schweiz: 2016-03-03 - 2016-03-22

97. J. Ritman
Initial measurements with antiprotons at the upcoming FAIR/PANDA facility
 XXIII International Baldin Seminar on High Energy Physics Problems, Dubna, Russia: 2016-09-19 - 2016-09-24

98. J. Ritman
Summary of the Cross-topic: Strongly Interacting Matter
 Matter and Universe Yearly Retreat, Mainz, Germany: 2016-12-12 - 2016-12-13

99. J. Ritman
Exploring Excited Hyperon Spectroscopy with Antiproton Beams at PANDA
 Workshop on Physics with Neutral Kaon Beam at JLab, Newport News, USA: 2016-11-16 - 2016-11-17

100. J. Ritman
Hadron Physics with PANDA: From FAIR Phase 0 to Phase 1
 KHuK Jahrestagung, Bad Honnef, Germany: 2016-12-08 - 2016-12-09

101. S. Schadmand
Light Meson Decay working group activities
 CLAS Collaboration Meeting, Jefferson Lab, Newport News, USA: 2016-02-23 - 2016-02-26

102. S. Schadmand
update on the $\omega \rightarrow \pi^0 e^+ e^-$ analysis
 CLAS Collaboration Meeting, Jefferson Lab, Newport News, USA: 2016-06-15 - 2016-06-18

103. S. Schadmand
Conversion Decays of Light Mesons
 Baryons 2016 - International Conference on the Structure of Baryons, Florida State University Alumni Center, Tallahassee, USA: 2016-05-16 - 2016-05-20

104. X. Song
Box anomaly in $\eta' \rightarrow \pi^+ \pi^- \gamma$ with clas g12 data (remote)
 CLAS Collaboration Meeting, Jefferson Lab, Newport News, USA: 2016-11-01 - 2016-11-04

105. S. Spellerberg *et al.*
New irradiation Facilities for Development of Production Methods of Medical Radionuclides at Various Cyclotrons at Forschungszentrum Jülich
 International Workshop on Targetry and Target Chemistry, Santa Fe, USA: 2016-08-29 - 2016-09-01

106. S. Srinivasan
Design and Construction of the HESR BPM prototype wiretest bench at COSY, Forschungszentrum Jülich
 Deutsche Physikalische Gesellschaft e.V.-Frühjahrstagung, Darmstadt, Germany: 2016-03-14 - 2016-03-18

107. T. Stockmanns
GPUs for Track Trigger in High Energy Physics
 Topical Workshop on Parallel Computing for Data Acquisition and Online Monitoring, Karlsruhe, Germany: 2016-03-07 - 2016-03-08

108. T. Stockmanns
Message Queues for Online Reconstruction on the Example of the PANDA Experiment
 CHEP 2016 Conference, San Francisco, USA: 2016-10-08 - 2016-10-14

109. H. Ströher
Fifty Years of Nuclear Chemistry
 Commemorative Symposium "Fifty Years of Nuclear Chemistry, Forschungszentrum, Jülich, Germany: 2016-04-28 - 2016-04-29

110. H. Ströher
Precision Physics
 7th Georgian-German School and Workshop in Basic Science, Tbilisi, Georgia: 2016-08-28 - 2016-08-31

111. H. Ströher
Introducing the Helmholtz Association of German Research Centres (HGF)
 Tbilisi Science and Innovation Fest: Georgian-German Day of Science, Tbilisi, Georgia: 2016-09-19 - 2016-09-19

112. H. Ströher
A Farmer or a Hunter -Should Researchers be Driven by Pre-determined Goals or by Sheer Curiosity?
 Tbilisi Science and Innovation Fest: Georgian-German Day of Science, Tbilisi, Georgia: 2016-09-19 - 2016-09-19

113. H. Ströher
COSY-Jülich - A Status Report
 KHuK Jahrestagung, Bad Honnef, Germany: 2016-12-02 - 2016-12-02

114. H. Ströher
Georgian-German Science Bridge - A Best Practice Example
 Kick-off Workshop "Palestinian-German Science Bridge, Jülich, Germany: 2016-12-07 - 2016-12-09

115. Y. Valdau *et al.*
[The physics program of PAX at COSY](#)
 XVI Workshop on High Energy Spring Physics, Dubna, Russia: 2015-09-08 - 2015-09-12

116. S. Vejdani
[Feasibility studies for the open-charm production in proton-antiproton reactions for the PANDA experiment](#)
 DPG Frühjahrstagung, Darmstadt, Germany: 2016-03-14 - 2016-03-18

117. C. Weidemann *et al.*
[Model Driven Machine Improvement of COSY Based on ORM Data](#)
 International Particle Accelerator Conference (7th), Busan, Korea: 2016-05-08 - 2016-05-13

118. P. Wintz
[Jülich Straws and their application in tracking at small polar angles in HADES](#)
 XXXII. HADES Collaboration Meeting, Paris, France: 2016-10-17 - 2016-10-21

119. P. Wintz
[Challenges and Opportunities in Gaseous Detectors](#)
 2. Annual MT Meeting, KIT Karlsruhe, Germany: 2016-03-08 - 2016-03-10

120. P. Wintz
[STT Status Report](#)
 Tracking Session at LVI. PANDA Collaboration Meeting, Ruhr-Universität Bochum, Germany: 2016-02-29 - 2016-03-04

121. P. Wintz
[STT News](#)
 Tracking Session at LVII. PANDA Collaboration Meeting, GSI Darmstadt, Germany: 2016-06-06 - 2016-06-10

122. P. Wintz
[STT Status Update](#)
 Tracking Session at LVIII. PANDA Collaboration Meeting, Helmholtz-Institut Mainz, Germany: 2016-09-12 - 2016-09-16

123. P. Wintz
[STT System Status Report](#)
 Technical Board Session at LVIII. PANDA Collaboration Meeting, Helmholtz-Institut Mainz, Germany: 2016-09-12 - 2016-09-16

124. P. Wüstner *et al.*
[A Small Data Acquisition System for the KOALA Experiment in Jülich](#)
 2016 IEEE-NPSS Real Time Conference, Padova, Italy: 2016-06-06 - 2016-06-10

125. M. Zurek
[Charge Symmetry Breaking In The \$dd \rightarrow \alpha\pi^0\$ Reaction With WASA-at-COSY](#)
 The 26th International Nuclear Physics Conference, Adelaide, Australia: 2016-09-11 - 2016-09-16

126. M. Zurek
[Charge Symmetry Breaking in \$dd \rightarrow {}^4\text{He}\pi^0\$](#)
 Bonn-Cologne Graduate School of Physics and Astronomy Poster Session, Bonn, Germany: 2016-06-23 - 2016-06-23

C.2 Colloquia

1. L. Dai
Comprehensive amplitude analysis of $\gamma\gamma \rightarrow \pi\pi$ and $K\bar{K}$ below 1.5 GeV
Universität Mainz:
2. A. Halama *et al.*
Characterization of BPM pickup designs for the HESR @ FAIR using simulations and numerical calculations
DPG-Frühjahrstagung 2016, Darmstadt, Germany: 2016-03-14 - 2016-03-18
3. A. Halama and V. Kamedzhiev
Fully automated adjustment of the electron beam line of the 2 MeV Electron Cooler at the Cooler Synchrotron @ FZ-Jülich
DPG-Frühjahrstagung 2016, Darmstadt, Germany: 2016-03-14 - 2016-03-18
4. F. Hauenstein
Associated Strangeness Production in Proton-Proton Interactions
Wien, Österreich: 2016-04-06 -
5. F. Hauenstein
Associated Strangeness Production in the $pp \rightarrow pK\Lambda$ Reaction Measured by COSY-TOF
Norfolk, Virginia, USA: 2016-07-19 -
6. V. Hejny
Measurement of Electric Dipole Moments at Storage Rings
Hadron Physics Summer School, Jülich, Germany: 2016-09-05 - 2016-09-09
7. V. Kamedzhiev
Beam diagnostics for the HESR
36th HESR Consortium Meeting, Jülich, Germany: 2016-12-12 - 2016-12-13
8. V. Kamedzhiev
Status of the IKP facilities
4th ARD ST3 workshop, Berlin, Germany: 2016-07-13 - 2016-07-15
9. A. Lehrach
Progress and Plans on Hadron Accelerator Developments at FZJ
2nd Annual Matter and Technology Meeting, Karlsruhe, Germany: 2016-03-08 - 2016-03-11
10. A. Lehrach
Accelerator Physics
Hadron Physics Summer School, Jülich, Germany: 2016-09-05 - 2016-09-09
11. A. Lehrach
Accelerator Basics
Jülich Krakow Summer School 2016, Science-UP, Jülich, Germany: 2016-09-12 - 2016-09-16
12. L. Ludhova
Neutrino physics with the Borexino detector
Dresden, Germany: 2016-06-09 - 2016-06-09

13. L. Ludhova
[Status and Future of Neutrino Physics with Scintillator-Based Detectors](#)
Aachen, Germany: 2016-05-23 - 2016-05-23

14. L. Ludhova
[Geoneutrino measurement with Borexino](#)
München, Germany: 2016-03-29 - 2016-03-29

15. L. Ludhova
[Low-energy neutrinos](#)
JEDI collaboration meeting, Jülich, Germany: 2016-02-29 - 2016-02-29

16. L. Ludhova
[Solar and Geo Neutrinos](#)
Bratislava, Slovakia: 2016-02-25 - 2016-02-25

17. L. Ludhova
[Solar and Geo Neutrinos](#)
Aachen, Germany: 2016-01-19 - 2016-01-19

18. L. Ludhova
[“La struttura della Terra: metodi geologici, fisici e chimici di investigazione”](#)
Gran Sasso, Italy: 2016-10-27 - 2016-10-28

19. L. Ludhova
[Geoneutrinos](#)
PRISMA, Mainz, Germany: 2016-12-07 - 2016-12-07

20. A. Nogga
[Predictions for Light hypernuclei based on chiral and similarity renormalization group-evolved interactions](#)
Athens, OH, USA:

21. J. Ritman
[Hadron Physics with PANDA](#)
Open Plenary session of the 2nd Meeting of the Joint Scientific Council of GSI and FAIR, Darmstadt, Germany:
2016-11-14 - 2016-11-15

22. T. Stockmanns
[HEP pixel detectors for TEM?](#)
Workshop on Scientific Directions for Future Transmission Electron Microscopy, Forschungszentrum Jülich,
Germany: 2016-10-24 - 2016-10-26

23. H. Ströher
[Update on SMARTILabs](#)
Visit of Georgian Delegation (Minister Tamar Sanikidze) to Forschungszentrum Jülich, 2016-05-10 - 2016-05-10

24. H. Ströher
[Experience with ERC Grants](#)
Interim Evaluation of H2020 - Expert Hearing, Brussels, Belgium: 2016-09-12 - 2016-09-12

25. H. Ströher

Experience with ERC Grants

Informationsveranstaltung der RWTH Aachen und JARA zu den Förderlinien des Europäischen Forschungsrats, Aachen, Germany: 2016-11-23 - 2016-11-23

26. S. Vejdani

First beam test results for the STT - flash ADC readout

PANDA LVII. collaboration meeting, Darmstadt, Germany: 2016-06-06 - 2016-06-10

D Diploma and Ph.D. Theses

1. Bachelor, Master, Diploma

1. P. Buske
Bachelor thesis: **Development of a Sona Transition for Metastable Hydrogen Atoms**
RWTH Aachen, Germany
2. T. Dato
Bachelor thesis: **Four-pion contributions to the eta-prime transition form factor**
Universität Bonn, Germany
3. M. Erdmann
Diploma Thesis: **Entwicklung eines Systems zur Überprüfung der Integrität und Sicherheit des Datenaufnahmesystems von PANDA**
Ruhr-Universität Bochum, Fakultät für Physik und Astronomie, Germany
4. I. Hammer
Master Thesis: **Systematic study of the impact of unitarization on quark models**
University Bonn, Germany
5. F. Kibellus
Bachelor thesis: **Entwicklung eines Spurfindealgorithmus für das Forward Tracking System des PANDA-Detektors**
Fachhochschule Aachen, Campus Jülich, Germany
6. M. Martić
Bachelor thesis: **Produktion und Nachweis von polarisierten HD Molekülen im Hinblick auf die polarisierte Kernfusion**
Universität Düsseldorf, Germany
7. H. Matschat
Bachelor thesis: **Development of a trigger system based on FPGA logic**
RWTH Aachen, Germany
8. A. Rolofs
Bachelor thesis: **Production of Nuclear-Spin-Polarized Deuterium**
Universität Düsseldorf, Germany
9. W. Sartison
Bachelor thesis: **Erzeugung und Messung von kernspinpolarisierten HD Molekülen**
Universität Göttingen, Germany
10. V. Schmidt
Master thesis: **Analysis of Closed-Orbit Deviations for a first direct Deuteron Electric Dipole Moment Measurement at the Cooler Synchrotron COSY**
RWTH Aachen, Germany
11. A.A. Skawran
Master thesis: **Comparison of Frozen and Quasi Frozen Spin Concepts for a Deuteron Electrical Dipole Moment Storage Ring**
Forschungszentrum Jülich, Germany

12. S. Srinivasan
Master thesis: **Design and Construction of a stretched wire test bench to characterize Beam Position Monitor for the High Energy Storage Ring**
FH-Aachen, Germany
13. M. Thiel
Bachelor thesis: **Spintune change due to an electric field kick at the particle accelerator and storage ring COSY**
Universität Regensburg, Germany
14. J. Wynen
Master thesis: **Theoretically consistent description of lineshapes for near threshold resonances**
RWTH Aachen, Germany

2. Ph.D.

1. Z. Bagdasarian
Measurement of Nucleon-Nucleon Elastic Scattering at Small Angles using the ANKE spectrometer
Mathematisch-Naturwissenschaftliche Fakultät der Universität zu Köln, Germany
2. L. Cao
Simulation of the D_s Semileptonic Decay with the PANDA Detector and Experimental Verification of the Micro-Vertex-Detector Pixel Readout ASIC with Proton Test Beam
Ruhr-Universität Bochum, Germany
3. I. Engin
Towards Polarization Measurements of Laser-accelerated Helium-3 Ions
Heinrich-Heine-Universität Düsseldorf, Germany
4. M. Jabua
Ultimate Resolution X-ray Spectroscopy of Chemical-Effects in Manganese Compounds
Mathematisch-Naturwissenschaftliche Fakultät der Universität zu Köln, Germany
5. M. Papenbrock
Investigation of the tensor analysing power T_{20} in the reaction $\vec{d} + p \rightarrow {}^3\text{He} + \eta$ with the COSY-ANKE experiment
Mathematisch-Naturwissenschaftliche Fakultät der Westfälischen Wilhelms-Universität Münster, Germany
6. M. Rosenthal
Experimental Benchmarking of Spin Tracking Algorithms for Electric Dipole Moment Searches at the Cooler Synchrotron COSY
RWTH Aachen University, Germany
7. M. Zurek
Investigation of the Charge Symmetry Breaking Reaction $dd \rightarrow {}^4\text{He}\pi^0$ with the WASA-at-COSY Facility
Mathematisch-Naturwissenschaftliche Fakultät der Universität zu Köln, Germany

E Awards & Offers for Professorships

Z. Bagdasarian: Cotutelle de thèse PhD from University of Cologne and Tbilisi State University, selected to participate in the 66th Lindau Nobel Laureate Meeting

L. Eltcov: Awarded the Kurchatov price for the best students work in 2016 by the Kurchatov Institute, Moscow, Russia

F. Goldenbaum: Awarded Professorship (APL) at University of Wuppertal, Faculty of Mathematics and Natural Sciences

C. Hanhart: Teaching award 2016 of the Faculty Physics/Astronomy of the Rheinische Friedrich-Wilhelms-Universität Bonn, Germany

U.-G. Meißner: Awarded the Lise Meitner Prize 2016 by the Nuclear Physics division of the European Physical Society

M. Rosenthal: JARA Excellent Junior Award for project “Spin Tracking Studies towards Electric Dipole Moment Measurements in Storage Rings” (JARA-FAME)

F Third Party Funded Projects

Project	Responsible	Funded by
HGF - Fellow Award C.Roberts Preisgeld	U. Meißner	HGF
SFB/TRR 110 Quantenchromodynamik TP A01	J. Haidenbauer	SFB
SFB/TRR 110 Quantenchromodynamik TP B03	C. Hanhart	SFB
SFB/TRR 110 Quantenchromodynamik TP B06	U. Meißner	SFB
SFB/TRR 110 Quantenchromodynamik TP B06	A. Nogga	SFB
SFB/TRR 110 Quantenchromodynamik TP B09	T. Luu	SFB
POLPBAR Management	H. Ströher	EU Projekt
POLPBAR Research	H. Ströher	EU Projekt
PANDA/ Straw Tube Tracker	J. Ritman	Industrieprojekt mit der GSI GmbH
PANDA/ Micro Vertex Detector	J. Ritman	Industrieprojekt mit der GSI GmbH
srEDM ERC Advanced Grant Management	H. Ströher	EU Projekt
srEDM ERC Advanced Grant Research	H. Ströher	EU Projekt
HESR Dipole und Quadrupole	R. Tölle	Industrieprojekt mit der FAIR GmbH
HESR -sonstige Magnete	U. Bechstedt	Industrieprojekt mit der FAIR GmbH
HESR -Netzgeräte	M. Retzlaff	Industrieprojekt mit der FAIR GmbH
HESR -Hochfrequenz	R. Stassen	Industrieprojekt mit der FAIR GmbH
HESR-Injektion P1	R. Toelle	Industrieprojekt mit der FAIR GmbH
HESR-Strahldiagnose	V. Kamedzhiev	Industrieprojekt mit der FAIR GmbH
HESR- Vakuum P1	F. Esser	Industrieprojekt mit der FAIR GmbH
HESR- Stochastische Kühlung	R. Stassen	Industrieprojekt mit der FAIR GmbH
HESR- Panda-Integration P1	D. Prasuhn	Industrieprojekt mit der FAIR GmbH
AVA MSCA I TN	D. Grzonka	EU Projekt
PPP-Polen (Polarisation Antiproton Prod.)	D. Grzonka	DAAD

G JCHP-FFE Projects

Project	Institute	Responsible
PD Dr. A. Khoukaz	Westfälische Wilhelms-Universität Münster	Mesonenproduktion in Nukleon-Nukleon- und Nukleon-Kern-Stößen an COSY
Prof. Dr. Vorobyev	PNPI Gatchina	ANKE
Prof. Dr. M. Nioradze	Tbilisi State University	NN-elastic scattering studies at COSY
PD Dr. D. Eversheim	HISKP Universität Bonn	Time Reversal Invariance Test at COSY (TRIC)
Prof. N. Nikolaev	L.D. Landau Institute Moscow, Russia	Numerical simulations of spin dynamics for JEDI experiments, searching for permanent Electric Dipole Moments of deuterons and protons at COSY
Dr. J. G. Messchendorp	University of Groningen, Kernfysisch Versneller Instituut, Netherlands	Momentum Dependent electron Reconstruction for WASA and the PANDA Pre-Assembly
Prof. A. Roy	Indian Institute of Technology Indore, India	The η meson decay into $\gamma\gamma^*$ in pp reactions with WASA-at-COSY
Prof. Dr. P. Lenisa	Università degli Studi di Ferrara, Italy	Spin-filtering studies in storage rings
Dr. A. Kulikov	JINR Dubna, Moscow Region, Russia	Spin Experiments at ANKE
Prof. Dr. U. Wiedner	Ruhr-Universität Bochum	Development for the forward endcap of the PANDA EMC and buildup of the final endcap within PANDA in Jülich
Prof. H. Chen	Southwest University, School of Physical Science and Technology, China	Simulation and optimization of the PANDA detector to measure the form factor of the $D_s \rightarrow e + \nu + \pi, \eta, \eta'$ decay
Prof. P. Lenisa	Università degli Studi di Ferrara, Italy	Spin-filtering studies in storage rings
Prof. U. Wiedner	Ruhr-Universität Bochum	Entwicklung für das Slow-control-System von PANDA
Prof. A. Schmeink	RWTH Aachen, Dept. of Electrical Engineering	A secure real-time remote control and operation of COSY subcomponents
Prof. Dr. K. Brinkmann	Justus-Liebig-Universität Gießen	Development and Validation of Detector Components and Preassembly for the PANDA MVD

H Conferences (co-)organized by the IKP

H.1 Physics with neutral kaon beam at JLab workshop

A workshop at Thomas Jefferson National Accelerator Facility in Newport News, VA was co-organized February 1-3, 2016 by IKP to discuss physics opportunities with a kaon beam at Jefferson Lab. This workshop was organized to follow up on a letter of intent, “Physics Opportunities with Secondary KL beam at JLAB,” (LOI-12-15-001), which was presented to the Program Advisory Council PAC43. The kaon nucleon scattering on unpolarized and polarized targets with GlueX set up in Hall D was discussed with the emphasis on hyperon spectroscopy. Such studies may expand the existing scientific program on hadron spectroscopy at Jefferson Laboratory. For details, refer to: <https://www.jlab.org/conferences/kl2016/>.

H.2 European JUNO analysis kick-off meeting at IKP

JUNO is going to be the first multi-kton liquid scintillator detector ever constructed. This 20kton detector is under construction in Jiangmen, China and is planned to start data taking in 2020. The collaboration comprises about 450 members from 66 institutions mostly from China and Europe. The main aim is to determine the neutrino mass hierarchy by measuring reactor neutrinos with 53 km baseline. However, such a large detector will be also a unique observatory for astroparticle physics and for the search of rare processes.

The IKP-2 became an official member of the JUNO collaboration in 2016 and it concentrates mainly on analysis and simulations. Developers of the JUNO software are currently mostly from China. In order to efficiently spread the know-how, contribute to the software development, as well as to be able to provide an important contribution to the data analysis, a need for the coordination among the European groups have arisen. This process was triggered by the live meeting organized by the JUNO IKP-2 group in April 2016. In total, there have been 28 participants, including 3 tutors from China. The idea of such meetings was very successful and another meeting followed in November 2016, organized at LLR, France. These meetings have also triggered the creation of a working group, responsible for the Monte Carlo production and validation, in which PhD students from IKP play a key role. In the meantime, the group has gained one of the best European expertise in the JUNO software framework.



Fig. 90: The kick-off meeting starting the coordination among European groups in the JUNO analysis and software development was organized at IKP in April 2016.

H.3 International workshop expanding COSY capability for multidisciplinary science

This meeting was called to explore the potential applications of COSY light ion beams for all research projects on campus as well as from neighboring universities. The benefit of realizing these capabilities seems to be suited for FZJ, one of the multidisciplinary research centers of HGF. The meeting attendance was well balanced between internal participants, Member of FZJ Board of Directors Prof. Schmidt, meeting organizers from IKP, institute leaders and experts from INM, PGI, JCNS, IBG, and external invitees Prof. A. Stahl from RWTH, Prof. E. Steffens from University of Erlangen-Nurnberg, Dr. M. Steffens and Dr. Hoeffgen from INT, Dr. U. Koester from ILL, Dr. D. Lowenstein from BNL, Dr. W. Barletta from LBNL and Dr. A. Faus-Golfe from Saclay/CSIC-UV. The meeting was started by the member of FZJ Board of Directors Prof. Schmidt. Prof. Steffens, the chair of COSY Beam Advisory Committee (CBAC) gave a comprehensive overview of the history of IKP as well as its accelerator facility including highlights of the achievements. The technical details of current machine performance including JULIC as well as beam time planning profiles were given by M. Bai and R. Gebel from IKP-4. In short, COSY current performance

- Wide range of energy of proton and deuteron beams for both internal and external target experiments
- Three extracted beam lines are available. One of the beamlines is situated in a very spacious area, and can be very valuable for studies that require large area
- Currently, routine slow extraction performance is 10^9 - 10^{11} particles within 10 sec up to mins
- Latest machine improvement has achieved i) beam based optics measurements of COSY as well as its extraction beamline ii) Significant reduction of orbit correction implementation iii) 1 sec extraction time with 2 nA beam current on target

The one and a half day intensive discussion was focused on

- the application of energetic light ion beam for medical radionuclide as well as radiobiology research; COSY's strength and weakness in comparison to the current worldwide facilities
- roles and contributions of the current accelerator facility and its group in the development of future facilities at FZJ

In summary, the conveners came to the following conclusions regarding the potential application of COSY to multi-disciplinary research fields:

- Current proton/deuteron beams from COSY have applications beyond current program in Physics as well as ongoing irradiation studies for electronics and detectors, activation study of medical radionuclide development, ongoing accelerator development to improve the extracted beam current, neutron production measurement for HBS project
- With expanded capabilities in additional light ions together with INM expertise as well as other medical physics groups, COSY can potentially make significant contributions to the medical physics on carrying out systematic radiobiological effect measurements as a function of light ion species and its energy
- Long term committed support of FZJ Board of Directors is the first key in pursuing the identified interests
- A set of workshops with the prospective user community is recommended to gauge both the interest in an upgraded facility and expand the potential user base

H.4 14th International workshop on meson production, properties and interaction—MESON 2016

The 14th International Workshop on Meson Production, Properties and Interaction - MESON 2016 - took place in Cracow, Poland, from 2 to 7 June 2016. The conference with a tradition dating back to 1991 was attended by over 170 participants from 21 countries from around the world. In total, there were 37 plenary talks, 69 parallel session talks and 24 posters. Additionally to regular conference program a special public talk on recent discovery of gravitational waves was given by Eugenio Coccia. Objective of the MESON Conferences is to provide an overview of the present status of the physics areas in which mesons play an important role, as well as of new developments, and a preview of the forthcoming investigations. The topics covered hadronic and electromagnetic meson production in a broad energy range, meson interaction with mesons and nuclei, structure of



Fig. 91: MESON2016 conference in Cracow.

hadrons, fundamental symmetry studies with mesons, exotic systems including the recent discovery of a dibaryon. Theoretical lectures focused mainly on the problems of low-energy QCD with use of effective field theory and lattice QCD. Widely presented were diverse approaches to the problems of dynamical chiral symmetry breaking, kaon bound states, mesic atoms and nuclei, and mesons in nuclear matter. Research related to the physics of mesons are closely linked to fundamental problems of physics. Therefore, the conference program this time was expanded to cover these items. In particular, the conference program covered recent results and future plans on investigations of electric dipole moment of hadrons and dark photon searches.

The success of the conference was made possible by the extensive work of the Advisory Committee, the Organizing Committee and the Local Organizing Committee. Special thanks are to our home institutions, organizers of the conference, Jagiellonian University, Forschungszentrum Juelich, INFN Frascati, and Institute of Nuclear Physics of the Polish Academy of Science, Cracow for their generous support.

We gratefully acknowledge further financial assistance from our sponsors: Marian Smoluchowski Cracow Scientific Consortium, the Municipality of Cracow (KRK2B), CAEN, ISEG, Wiener, Nowoczesna Elektronika and European Physical Journal. Last but not least we thank all the participants for interesting presentations and lively discussions on recent results and future projects. We appreciated very much the attendance of many young physicist who really vivified the atmosphere of the conference. The large number of participants engaged in interesting discussions, expected further discoveries in the fields presented at the conference and great ambience of Cracow direct our thoughts and motivation towards the next edition of the MESON conference, which we will organize in June 2018, at the same location.

H.5 Hadron Physics Summer School 2016

The Hadron Physics Summer School HPSS2016 took place from September 5 to September 9, 2016, at the con-

ference venue JUFA Hotel at Brückenkopfpark in Jülich. The HPSS2016 is the continuation of a biannual series of summer school that started in 2002.

More than 65 graduate and advanced undergraduate students from 16 countries and 3 continents participated in the summer school (19 females, 46 males. 6 IKP students). The school comprised lectures and working groups on theoretical, experimental, and accelerator aspects. The focus is on current issues in hadron physics with emphasis on current and future programs at the accelerators COSY (Jülich), ELSA (Bonn), LHC (CERN), CEBAF (Jefferson Lab), BEPC (Beijing) and FAIR (Darmstadt) featuring experiments like PANDA, Crystal Barrel, LHCb, CLAS, BESIII and the search for electric dipole moments of charged particles in storage rings (JEDI).

The Hadron Physics Summer School 2016 (HPSS2016) is jointly organized by scientists from the Institut für Kernphysik, Forschungszentrum Jülich, and the Universities Aachen, Bonn, Bochum, Düsseldorf and Giessen. The school is jointly financed by Forschungszentrum Jülich, the Helmholtz-Institut für Strahlen- und Kernphysik of the University of Bonn, Helmholtz International Center for FAIR, and the Collaborative Research Center CRC110 (Symmetries and the Emergence of Structure in QCD) funded by DFG and National Natural Science Foundation of China (NSFC). For more detailed information, see <http://collaborations.fz-juelich.de/ikp/hpss2016/index.shtml>.



Fig. 92: Participants and organisers of the HPSS2016 at the conference venue JUFA Hotel im Brückenkopfpark in Jülich.

H.6 Georgian–German Science Bridge: SMART|EDM Lab opening and 7th GGSWBS in Tbilisi

The Georgian Ministry of Education and Science (MoE), the Shota Rustaveli National Science Foundation (SRNSF) and the Federal Ministry of Education and Research (BMBF) have organized the Georgian–German Science Bridge Day as part of the Science and Innovation Festival 2016 during September 19 – 21 in Tbilisi

(Georgia). In this week a group of scientists from Forschungszentrum Jülich, including IKP, actively participated in the program, in particular Prof. S. Schmidt (Board of Management FZJ) who, together with the Science Minister of Georgia, Alexander Jejelava, opened the first so called SMART EDM at Tbilisi State University (TSU) (SMART stands for “Science, Medicine, Applied Research and Technology” and EDM for “Electric Dipole Moment”). Further SMART|Labs are planned in the areas of climate science and brain research. These laboratories provide young Georgian scientists, which have been educated in Jülich, an attractive return option to their home country. For the SMART EDM Lab, David Mchedlishvili, a young IKP postdoc, returns back to head the lab from January 1st, 2017. SMART|Labs are funded by the Georgian Ministry (MoE), while equipment and know-how for a common project will be delivered by Jülich.

Over the past 2 decades Forschungszentrum Jülich has built very intense collaborations with four Georgian universities: Tbilisi State University (TSU), Georgian Technical University (GTU), the Ilia State University (ISU) and the Agricultural University of Georgia (AUG). Many joint projects and workshops have already been implemented, such as the traditional “Georgian–German School and Workshop in Basic Science” (GGSWBS: <http://collaborations.fz-juelich.de/ikp/cgswhp/>). The 7th bi-annual meeting called (GGSWBS’16) took place in Tbilisi from August 28 to September 2, 2016 (see: <http://collaborations.fz-juelich.de/ikp/cgswhp/cgswhp16/>), this time on the subject: “Spin Physics, Symmetries and Applications”. Leading scientists from institutes of Forschungszentrum Jülich (IKP, IEK, INM, and ZEA), from RWTH Aachen and other national and international laboratories participated - together with their Georgian colleagues from partner institutions. The workshop focused on the following topics:

- Symmetries in Subatomic Physics (T- & CP-Violations)
- Electric Dipole Moment Searches (e.g. JEDI project)
- Neutrino Physics (e.g. JUNO project)
- Standard Model and Beyond (Theory, HEP Exp.)
- Engineering Sciences (Instrumentation, Electronics)
- Applications (e.g. Medical Imaging)

In addition, a JEDI collaboration meeting took place as a satellite (see: <http://collaborations.fz-juelich.de/ikp/jedi/>). Talks of these events together with additional information have been published in 2016 as “Schriften des Forschungszentrums Jülich”, Reihe Schlüsseltechnologien/Key Technologies, Band/Volume 134 (Eds.: A. Kacharava, S. Dues, H. Ströher).



Fig. 93: Participants of the international meeting “Spin Physics, Symmetries and Applications” (GGSWBS’16) in Tbilisi.

H.7 Symposium on “Advances in Effective Field Theories” and the Lise Meitner Prize

A collection of the world’s theoretical experts on nuclear and hadronic physics attended a symposium to discuss the advances made within effective field theories (EFTs) and their impact to nuclear and hadronic physics. This symposium, titled “Advances in Effective Field Theories”, was held at the Forschungszentrum Jülich (FZJ) in Germany from November 7-9. The twenty-three participants that presented at this symposium came from the USA, China, and Europe. In addition to the invited speakers, the symposium was well attended by an additional 60-70 participants. A central topic discussed

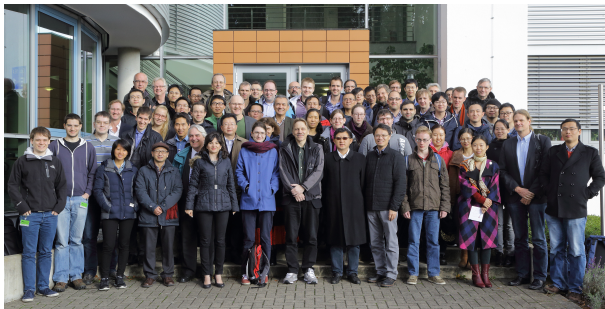


Fig. 94: Participants at the symposium “Advances in Effective Field Theories”.

during the symposium was chiral perturbation theory, the low energy EFT of Quantum Chromodynamics (QCD), the theory of quarks and gluons, and the relative advances made within this EFT. The interactions stemming from this EFT were used in nuclear lattice EFT (NLEFT), results of which were shown during the symposium. In particular, calculations of the spectrum of carbon and selected nuclear reactions were reported. Advances in lattice QCD calculations were also shown, as well as the

use of heavy quark EFT to describe exotic mesons. Other topics touched on EFTs for neutron-rich nuclei and nuclear matter, and the role of hypernuclei in the nuclear matter equation of state.

The symposium culminated in an awards ceremony where the Lise Meitner Medallion was awarded to Ulf Meißner for his contributions to the field of nuclear and hadronic physics. This prize is sponsored by the Nuclear Physics division of the European Physical Society and is awarded every two years. It consists of a monetary award and a medallion.

H.8 Excited hyperons in QCD thermodynamics at freeze-out

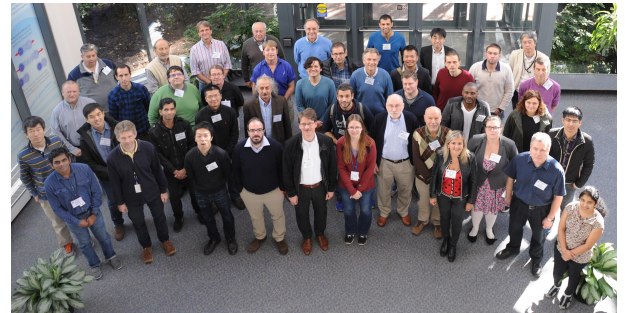


Fig. 95: YSTAR2016 – workshop on Excited Hyperons in QCD Thermodynamics at Freeze-Out.

The intention of the workshop co-organized by the IKP at the Thomas Jefferson National Accelerator Facility Newport News, VA, November 16-17, 2016 was to discuss the influence of possible “missing” hyperon resonances (JLab KLF Project) on QCD thermodynamics, on freeze-out in heavy ion collisions and in the early universe, and in spectroscopy. The workshop brought top experts, researchers, postdocs, and students from high-energy heavy ion interactions, lattice QCD and hadronic physics communities together. Recent studies that compared lattice QCD predictions of thermodynamic properties of quark-gluon plasma at freeze-out with calculations based on statistical hadron resonance gas models as well as experimentally measured ratios between yields of different hadron species in heavy ion collisions provide indirect evidence for the presence of “missing” resonances in all of these contexts. The aim of the YSTAR2016 Workshop was to sharpen these comparisons and advance our understanding of the formation of strange hadrons from quarks and gluons microseconds after the Big Bang and in today’s experiments at LHC and RHIC as well as at future facilities like FAIR, J-PARC and KL at JLab. It was concluded that the new initiative to create a secondary beam of neutral kaons at JLab will make a bridge between the hadron spectroscopy, heavy-ion experiments and lattice QCD studies addressing some major issues related to thermodynamics of the early universe and cosmology in general. The

Workshop was actually a successor to the KL2016 Workshop <https://www.jlab.org/conferences/kl2016/>, which took place early in 2016. For details, refer to: <https://www.jlab.org/conferences/YSTAR2016/>.

I Teaching Positions

Institute	Name	University
IKP-1	PD Dr. A. Gillitzer	Bonn
	Prof. Dr. F. Goldenbaum	Wuppertal
	Prof. J. Ritman Ph.D.	Bochum
	Dr. T. Stockmanns	Bochum
IKP-2	Prof. Dr. D. Gotta	Köln
	PD Dr. F. Rathmann	Aachen
	Prof. Dr. L. Ludhova	Aachen
	Prof. Dr. Dr. h.c. H. Ströher	Köln
	Prof. Dr. J. Pretz	Aachen
IKP-3/IAS-4	Univ. Doz. Dr. J. Haidenbauer	Graz
	Prof. Dr. C. Hanhart	Bonn
	Prof. Dr. S. Krewald	Bonn
	Prof. Dr. T. Luu	Bonn
	Prof. Dr. U.-G. Meißner	Bonn
	Dr. A. Nogga	Bonn
	PD Dr. A. Wirzba	Bonn
IKP-4	Prof. Dr. M. Bai	Bonn
	Prof. Dr. A. Lehrach	Aachen

J Personnel

DP A. Apostolou (IKP-1) (until 31 st Aug. 2016)	DI N. Giese (IKP-TA)
Dr. Z. Bagdasarian (IKP-2)	PD Dr. A. Gillitzer (IKP-1)
Prof. M. Bai (IKP-4)	J. Göbbels (IKP-TA)
Dr. U. Bechstedt (IKP-4)	Prof. Dr. F. Goldenbaum (IKP-1)
C. Berchem (IKP-TA)	Prof. Dr. D. Gotta (IKP-2)
Dr. E. Berkowitz (IKP-3/IAS-4) (since 14 th Nov. 2016)	Dr. D. Grzonka (IKP-1)
DP L. Bianchi (IKP-1)	Univ. Doz. Dr. J. Haidenbauer (IKP-3/IAS-4)
Dr. C. Böhme (IKP-4)	MSc. I. Hammer (IKP-3/IAS-4)
M. Böhnke (IKP-4)	Prof. Dr. C. Hanhart (IKP-3/IAS-4)
Dr. J. Böker (IKP-4)	T. Hahnrahts-von der Gracht (IKP-TA)
DI N. Bongers (IKP-4)	BEng. A. Halama (IKP-4)
Dr. B. Breitzkreutz (IKP-4)	Dr. M. Hartmann (IKP-2)
P. Brittnier (IKP-4)	Dr. F. Hauenstein (IKP-1) (until 30 th Sept. 2016)
P. Buske (IKP-2) (until 31 st July 2016)	DI R. Hecker (IKP-TA)
J. But (IKP-TA)	Dr. V. Hejny (IKP-2)
Dr. L. Cao (IKP-1)	DP N. Hempelmann (IKP-2)
W. Classen (IKP-4)	DP J.-H. Hetzel (IKP-4)
M. Comuth-Werner (IKP-TA)	DP F. Hinder (IKP-4)
Dr. C. Constantinou (IKP-3/IAS-4)	M. Holona (IKP-TA)
B. Dahmen (IKP-4) (until 17 th August 2016)	Dr. J. Hu (IKP-3/IAS-4)
DI F.U. Dahmen (IKP-4)	Dr. Q. Hu (IKP-1) (until 31 st December 2016)
Dr. L. Dai (IKP-3/IAS-4) (since 15 th Jan. 2016)	L. Huxold (IKP-2) (since 6 th June 2016)
MBA A. Derichs (IKP-1)	MSc. M. Jabua (IKP-2) (until 30 th April 2016)
C. Deliege (IKP-4)	Dr. A. Kacharava (IKP-2)
G. D'Orsaneo (IKP-2)	Dr. V. Kamerdzhev (IKP-4)
R. Dosdall (IKP-1)	Msc. P. Kampmann (IKP-2) (since 7 th Dec. 2016)
Dr. Y. Dutheil (IKP-4)	P. Kaniewski (IKP-2) (until 29 th February 2016)
C. Ehrlich (IKP-4)	Dipl.-Kffr. A. Kelleners (IKP-TA)
Dr. R. Engels (IKP-2)	Dr. I. Keshelashvili (IKP-2)
Dr. I. Engin (IKP-4) (until 29 th February 2016)	F. Kibellus (IKP-1) (until 30 th Sept. 2016)
B. Erkes (IKP-4)	A. Kieven (IKP-4)
DI F.-J. Etzkorn (IKP-4)	S. Kistemann (IKP-TA)
Dr. O. Felden (IKP-TA)	B. Klimczok (IKP-TA)
H.-W. Firmenich (IKP-TA)	MSc. C. Körber (IKP-3/IAS-4)
Y. Gan (IKP-2) (since 1 st December 2016)	M. Kremer (IKP-TA)
Dr. R. Gebel (IKP-4)	DI T. Krings (IKP-TA)
Dr. J. Gegelia (IKP-3/IAS-4)	M. Küven (IKP-4)
Msc. C. Genster (IKP-2) (since 1 st Jan. 2016)	Dr. M. Kunkel (IKP-1)
R. Geppert (IKP-TA)	Dr. T. Lähde (IKP-3/IAS-4)

DP A. Lai (IKP-1)
 K.-G. Langenberg (IKP-4)
 Prof. Dr. A. Lehrach (IKP-4)
 Dr. D. Lersch (IKP-1)
 H. Le Thi (IKP-3/IAS-4) (since 1st January 2016)
 Dr. N. Li (IKP-3/IAS-4)
 X.-H. Liu (IKP-3/IAS-4) (since 6th Nov. 2016)
 Dr. B. Lorentz (IKP-4)
 Dr. B. Lu (IKP-3/IAS-4)
 Prof. Dr. L. Ludhova (IKP-2)
 Prof. Dr. Th. Luu (IKP-3/IAS-4)
 Prof. Dr. R. Maier (IKP-4) (until 29th Feb. 2016)
 M. Martic (IKP-2) (until 31st July 2016)
 H. Matschat (IKP-2) (until 30th June 2016)
 DI H.-P. May (IKP-4)
 Prof. Dr. U.-G. Meißner (IKP-3/IAS-4)
 Dr. S. Merzliakov (IKP-4)
 DP S. Mey (IKP-4) (until 26th Feb. 2016)
 Dr. S. Mikirtychiants (IKP-2) (until 31st Dec. 2016)
 C. Müller (IKP-TA)
 DP F. Müller (IKP-2)
 S. Müller (IKP-TA)
 DP P. Musiol (IKP-1)
 Dr. A. Naß (IKP-2)
 B. Nauschütt (IKP-4) (since 18th April 2016)
 Dr. A. Nogga (IKP-3/IAS-4)
 Msc. Ö. Penek (IKP-2) (since 1st Dec. 2016)
 BSc J. T. Peters (IKP-4)
 Dr. D. Prasuhn (IKP-4)
 Dr. E. Prencipe (IKP-1)
 D. Prothmann (IKP-TA)
 H. Pütz (IKP-4)
 DP J. Pütz (IKP-1)
 MSc. S. Quilitzsch (IKP-4)
 PD Dr. F. Rathmann (IKP-2)
 Msc. M. Redchuk (IKP-2) (since 1st Oct. 2016)
 DI K. Reimers (IKP-4)
 DI M. Retzlaff (IKP-4)
 Prof. J. Ritman Ph.D.(IKP-1)
 Dr. E. Roderburg (IKP-1)
 G. Roes (IKP-TA)
 A. Rolofs (IKP-2) (until 29th Feb. 2016)
 Dr. M. Rosenthal (IKP-4) (until 30th Sept. 2016)
 N. Rotert (IKP-4)
 D. Ruhrig (IKP-4)
 W. Sartison (IKP-2) (until 30th September 2016)
 PD Dr. S. Schadmand (IKP-1)
 MSc. M. Schever (IKP-2) (since 4th April 2016)
 Dr. R. Schleichert (IKP-2)
 MSc. V. Schmidt (IKP-4) (since 1st Dec. 2016)
 W. Schoofs (IKP-4) (until 31st March 2016)
 F. Scheiba (IKP-4)
 H. Schiffer (IKP-TA)
 M. Schmühl (IKP-4)
 Dr. Th. Sefzick (IKP-TA)
 Prof. Dr. Y. Senichev (IKP-4)
 Dr. V. Serdyuk (IKP-1)
 Dr. A. Shindler (IKP-3/IAS-4) (until 31st July 2016)
 MSc. N. Shurkhno (IKP-4)
 DI M. Simon (IKP-4)
 H. Simonsen (IKP-TA)
 A. Skawran (IKP-4) (until 30th September 2016)
 Dr. X. Song (IKP-1) (since 13th January 2016)
 D. Spölgen (IKP-2)
 S. Srinivasan (IKP-4) (until 30th August 2016)
 Dr. R. Stassen (IKP-4)
 G. Sterzenbach (IKP-1)
 Dr. H. Stockhorst (IKP-4)
 Dr. T. Stockmanns (IKP-1)
 Prof. Dr. Dr. h. c. H. Ströher (IKP-2)
 MSc. M. Thelen (IKP-4)
 Dr. R. Tölle (IKP-4)
 MSc. F. Trinkel (IKP-2)
 BSc. P. Tripathi (IKP-4) (since 15th Nov. 2016)
 Dr. S. Trusov (IKP-2)
 J. Uehlemann (IKP-1)
 DI T. Vashegyi (IKP-4)
 DP S. Vejdani (IKP-1)
 BEng. A. Vishwanantha (IKP-3/IAS-4) (unt. 31st Mar. 16)
 Dr. C. Weidemann (IKP-4)
 DP P. Weiß (IKP-2) (until 30th June 2016)
 D. Wichmann (IKP-2) (until 31st August 2016)

Dr. P. Wintz (IKP-1)
PD Dr. A. Wirzba (IKP-3/IAS-4)
DI J.-D. Witt (IKP-4) (until 29th February 2016)
MSc. J.-L. Wynen (IKP-3/IAS-4)
Dr. C. Xiao (IKP-3/IAS-4)
Dr. X. Xiong (IKP-3/IAS-4) (since 4th Oct. 2016)
Dr. H. Xu (IKP-1)
Dr. D.-L. Yao (IKP-3/IAS-4) (until 31st Dec. 2016)
Dr. E. Zaplatin (IKP-4)
H. Zens (IKP-4)
Dr. L. Zhao (IKP-3/IAS-4)
Dr. M. Zurek (IKP-2)

IKP-1 = Experimental Hadron Structure
IKP-2 = Experimental Hadron Dynamics
IKP-3/IAS-4 = Theory of the Strong Interactions
IKP-4 = Large-Scale Nuclear Physics Equipment
IKP-TA = Technical Services and Administration

K Further Contributions

articles available on-line under downloads: <http://www.fz-juelich.de/ikp/>

1. Drift chamber calibration in the P-349 Antiproton Polarization Experiment
2. Analyzing power of hard bremsstrahlung $pp \rightarrow \{pp\}_s + \gamma$ in the $\Delta(1232)$ region
3. Estimation of the ANKE STT tracking efficiency from experimental data
4. Towards an upper limit for the decay $\eta \rightarrow \pi^0 e^+ e^-$ using $pd \rightarrow {}^3\text{He} \eta$ data from WASA-at-COSY
5. Hardware Development for a new Stochastic Cooling System dedicated to EDM Experiments
6. Towards a new Tune Meter for COSY
7. Studies on CP violation in the decay $\eta \rightarrow \pi^0 e^+ e^-$ in pp scattering experiments with WASA-at-COSY
8. Synchronous sampling device for the parametric current transformer
9. Analytic Model of in-Plane Depolarization and Phase Drift of the Spin Tune
10. Dalitz plot of $\eta' \rightarrow \eta \pi^+ \pi^-$ using CLAS g12 data
11. Study of the electromagnetic transition form factor of the η meson with WASA-at-COSY
12. Electrostatic deflector development
13. Progress with the model development for the 2 MeV electron cooler
14. Theoretical Development of a Beam Position Independent Capacitive Quadrupole Pickup
15. Analysis of Feedback System Data
16. Lyapunov Analysis of Particle Tracking for the HESR
17. Theoretical Limits of Closed Orbit Corrections
18. Studies on η production in pd fusion to ${}^3\text{He} \eta$ with WASA-at-COSY
19. Development of a Track Reconstruction Algorithm for the Panda Forward Tracking System
20. Study of dp breakup reaction in the Forward Detector
21. A read-out system for the PANDA MVD prototypes: development and results
22. Dalitz Plot Analysis of $\eta \rightarrow \pi^+ \pi^- \pi^0$ with CLAS
23. Low-noise BPM preamplifier for the HESR
24. The EDM polarimetry detector development
25. Automated Measurement of the COSY Injection Energy
26. Simulations on Ion Clearing for the HESR using COMSOL Multiphysics
27. Reconstruction efficiency for Forward-Central coincidences
28. Amplitude estimation of a sine function based on confidence intervals and Bayes' theorem
29. Study of Excited Xi Baryons in $\bar{p}p$ -Collisions with the PANDA Detector
30. Searching for η -mesic ${}^3\text{He}$ with WASA-at-COSY facility
31. Systematic effects of orbit excursions in the spin tune mapping with solenoids
32. Simulation of closed orbit influencing effects at COSY

33. Production of η -mesons in pn-collisions at ANKE
34. Quasi-Frozen spin concept of deuteron storage ring as an instrument to search electric dipole moment
35. Developments for the EDM polarimeter at COSY
36. Measurements of the new HESR pick-up at COSY
37. Search for η -mesic ^4He in the $dd \rightarrow ^3\text{He} \, n \, \pi^0$ and $dd \rightarrow ^3\text{He} \, p \, \pi^-$ reactions with the WASA-at-COSY facility
38. Search for box anomaly via $\eta' \rightarrow \gamma \pi^+ \pi^-$ with CLAS
39. Search for light dark bosons in η decays
40. Executive Summary of Theoretical Developments in Electron Cooling and Stochastic Cooling
41. FairMQ for the PANDA Experiment
42. Comparison of the theoretical higher order Rogowski coil BPM model with a simulation
43. Elastic d+C12 scattering within the Glauber approach
44. Measurement of the spatial and energy loss resolution for the STT flash ADC readout for the PANDA experiment
45. Simulation for the FToF detector in PANDA experiment
46. Calibration of linear optics of COSY using LOCO analysis